

Structure-Property Interrelations of Polymers for Photonics and Electronics

A Dissertation
Presented to
The Academic Faculty

By

Alex Balzer

In Partial Fulfillment
of the Requirements for the Degree
Doctor of Philosophy in the
School of Chemical and Biomolecular Engineering

Georgia Institute of Technology
May 2022

COPYRIGHT © 2022 BY ALEX BALZER

Structure-Property Interrelations of Polymers for Photonics and Electronics

Approved by:

Dr. Natalie Stingelin, Advisor
School of Materials Science and Engineering
School of Chemical and Biomolecular
Engineering
Georgia Institute of Technology

Dr. Matthew Realff
School of Chemical and Biomolecular
Engineering
Georgia Institute of Technology

Dr. Carson Meredith
School of Chemical and Biomolecular
Engineering
Georgia Institute of Technology

Dr. Shannon Yee
School of Mechanical Engineering
Georgia Institute of Technology

Dr. Carlos Silva
School of Chemistry and Biochemistry
School of Physics
Georgia Institute of Technology

ACKNOWLEDGEMENTS

I would like to express my deepest gratitude to my advisor, Dr. Natalie Stingelin. You have been an amazing mentor and role model. I am thankful for your support, guidance, and encouragement even from across the globe. You taught me how to be a researcher, mentor, form collaborations, and be a better communicator. Thank you for guiding me through this journey while also allowing me to develop my own path forward. From walking into an empty lab with Aditi and I as your first students at Tech to walking out with a PhD, I would not have it any other way!

I would like to thank the entire Stingelin lab, from members here at Tech to those across the pond! It would not have been the same without you all. I would like to thank our postdocs Dr. Seong-min Kim and Dr. Andre Zeumault, from whom I have learnt a lot. I would also like to thank all of the Stingelin group members I crossed paths with: Aditi, Hongmo, Marlow, Conor, Aziz, Tanner, Mark, Victoria, Amalie, Stefan, Shengyang, and Faisal, as well as many visiting researchers! Thanks all for our intellectual group meetings, trips to conferences, karaoke, and countless happy hours!

I would like to thank my thesis committee members, Dr. Carlos Silva, Dr. Shannon Yee, Dr. Matthew Realff, and Dr. Carson Meredith for encouraging me to think more critically about my research and for their valuable insights, advice, and feedback. I would like to thank all my direct collaborators and colleagues in my many projects at Tech, including Dr. Carlos Silva, Dr. Shannon Yee and Daron Spence, Dr. John Reynolds, Dr. Anna Österholm, Dr. Lisa Savagian, and Brandon Ditullio. Thank you to Dr. Jaime Martin for hosting me at POLYMAT, and refining my Flash DSC skills, a technique that has greatly

shaped my research. I would like to thank all my collaborators' and students who have contributed to this work.

Most importantly, I would like to thank my parents for their love and support through this long journey, for always believing in me, and encouraging me to pursue my dreams. I am forever grateful for everything that you have done for me. I would like to thank my brother and sister for their words of advice and encouragement.

I am very thankful to all my friends here in Atlanta and across the country for the wonderful memories. A special thanks to my girlfriend Audrey, who has been a wonderful supporter and friend through this journey, and I'm thankful for everything from our adventures together to support through covid lockdowns.

Abstract

In the first chapter of this thesis, the production and characterization of inorganic-organic hybrid materials is discussed. Inorganic-organic hybrids allow for the modification of physical properties and the addition of new features in polymer-based systems, and thus have received great interest. This thesis demonstrates that titanium oxide hydrates are highly versatile inorganic ‘fillers’ in polymer-based hybrids. Using the hydrate allows for the creation of versatile, low-temperature, sol-gel processed hybrids. This thesis shows that these hydrates increase the refractive index of hybrid materials with no or minimal optical loss due to the formation of a covalently crosslinked network. The high transparency in the visible and near-infrared range also proves useful for producing low-loss distributed Bragg Reflectors (DBRs) to aid and improve light and heat management. In particular, a visible range reflecting DBR can improve efficiencies of semi-transparent solar cells while maintaining transparency to chlorophyll absorption bands. This allows for charge generation in greenhouse applications. Additionally, shifting the stopband of the DBRs to the near-infrared range can reduce energy consumption in buildings by reflecting the heat from solar irradiation while maintaining visible transparency. Ultimately, we show a general understanding for this hybrid’s unique structure which can be expanded to new hybrids based on other metal oxide hydrates.

In the second chapter of this thesis, structure-property interrelations of semiconducting polymers are established using fast scanning calorimetry. The field of polymer-based electronics has witnessed major developments in the past few years that have led to systems of vastly improved charge transport- and energy-harvesting properties. This progress can be predominantly attributed to synthetic efforts in the form of the creation of new materials,

which often comprise backbones of a significantly more rigid nature than the first-generation polymer semiconductors and most bulk commodity plastics. Moreover, many semiconducting polymers frequently lack significant long-range order, but it is hypothesized that they may exhibit liquid-crystalline-like behavior because of their hairy-rod nature. To understand the polymer phase behavior, how it relates to chemical design and how it dictates important optoelectronic features, we use fast scanning calorimetry to identify the glass transition and possible liquid-crystalline-like transitions, as well as side-chain softening regimes, using physical aging signatures and isothermal annealing measurements. We show that the intrinsic UV-stability of semiconducting polymers can be tracked through increases of glass transitions through crosslinking. Additionally, the side-chain ordering and liquid-crystalline ordering of hairy-rod polymers are sensitive to backbone planarity and molecular weight, which affect optoelectronic and mechanical properties. The glass transition temperature for propylenedioxythiophene-based polymers is also shown to be affected by side-chain lengths, but independent of polarity and sterics. This approach allows us to gain insights on the role of polymer assembly and solid-state structure on energetic disorder and photophysical characteristics towards the delivery of important structure-property interrelations for design of fourth generation semiconducting plastics for organic solar cells, plastic electronics, wearable sensors, and beyond.

Contents

| | |
|--|------------|
| List of Figures..... | x |
| List of Tables | xiv |
| 1 Hybrid Materials in Optics and Photonics..... | 1 |
| 1.1 Introduction | 1 |
| 1.2 Materials and Methods | 3 |
| 1.2.1 Materials and Instruments..... | 3 |
| 1.2.2 Titanium Oxide Hydrate:PVA Hybrid..... | 5 |
| 1.2.3 Optical Modeling | 7 |
| 1.3 Titanium Oxide Hydrate:PVA Hybrids..... | 15 |
| 1.3.2 Low Optical Loss Materials..... | 17 |
| 1.3.3 Tunable Refractive Index..... | 21 |
| 1.3.4 Physical and Chemical Investigations | 23 |
| 1.3.5 The Case for a Molecular Hybrid | 35 |
| 1.4 1D Photonics: Distributed Bragg Reflectors..... | 37 |
| 1.4.1 Introduction..... | 37 |
| 1.4.2 TiOH:PVA Hybrids in DBRs | 41 |
| 1.4.3 Solution Processed DBRs | 43 |
| 1.4.4 DBR Applications..... | 45 |
| 1.5 Future Work and Conclusions..... | 60 |

| | | |
|----------|--|-----------|
| 1.5.1 | Titanium Oxide Hydrate:Polyalcohol Solutions | 60 |
| 1.5.2 | Future Work: New Hybrid Formulations and Processing..... | 64 |
| 1.5.3 | Conclusions..... | 65 |
| 2 | Fast Scanning Calorimetry | 67 |
| 2.1 | Introduction | 67 |
| 2.2 | Glass Transitions and Physical Aging..... | 68 |
| 2.3 | Semiconductors and their Side-Chains | 72 |
| 2.3.1 | OPV Materials | 73 |
| 2.3.2 | Hairy Rod Materials..... | 79 |
| 2.3.3 | OECT Materials | 95 |
| 2.3.4 | Additional Side-Chain Effects | 110 |
| 2.4 | Crystallization and Vitrification Kinetics | 115 |
| 2.5 | Future Work and Conclusions..... | 123 |
| 2.5.1 | Future Work: Phase Kinetics | 123 |
| 2.5.2 | Future Work: Liquid Crystalline Hairy-rod Polymers..... | 126 |
| 2.5.3 | Conclusions..... | 126 |
| 2.6 | Appendix | 129 |
| 2.6.1 | Appendix A: Chemical Structures | 129 |
| 2.6.2 | Appendix B: PA12 Supplemental Graphs | 130 |

| | | |
|----------|------------------------|------------|
| 3 | References..... | 133 |
|----------|------------------------|------------|

List of Figures

| | |
|--|----|
| Figure 1.1 Schematic of the Thin Film Case | 10 |
| Figure 1.2 Fabry-Pérot Oscillations in High Refractive Index Layers | 11 |
| Figure 1.3 Multilayered Coherent Structure | 13 |
| Figure 1.4 MATLAB App for TMM | 15 |
| Figure 1.5 Representation of Mono- and Poly-nuclear Titanium species. | 16 |
| Figure 1.6 Optical Transmission of Hybrids..... | 19 |
| Figure 1.7 Transmission and Reflection of Hybrids..... | 20 |
| Figure 1.8 Tunable Refractive Index Hybrids | 22 |
| Figure 1.9 Evidence of Crosslinked Network..... | 25 |
| Figure 1.10 DSC of Hybrids | 27 |
| Figure 1.11 TGA of Hybrids..... | 29 |
| Figure 1.12 TGA of Post-treated Hybrids..... | 30 |
| Figure 1.13 XPS of Hybrids..... | 32 |
| Figure 1.14 Annealing Effects of Hybrid Atomic Ratios | 34 |
| Figure 1.15 Comparing XPS to other Hybrids and Nanocomposites. | 35 |
| Figure 1.16 Proposed Titanium Oxide Hydrate:PVA Molecular Hybrid Structure. | 36 |
| Figure 1.17 DBR Schematic and Transmission..... | 41 |
| Figure 1.18 Commodity Plastic-based DBRs versus Hybrid-based DBRs. | 42 |

| | |
|---|----|
| Figure 1.19 Setup and Calibration of Dip-coated Layers. | 44 |
| Figure 1.20 Visible and Near-IR Hybrid-based DBRs. | 47 |
| Figure 1.21 Back-reflecting DBRs for Semi-transparent Solar Cells. | 48 |
| Figure 1.22 Heat Mirror Schematic for Passive Cooling. | 50 |
| Figure 1.23 Modeling heat-mirrors for maximum near-IR rejection. | 51 |
| Figure 1.24 Spectral Transmission and Reflection of DBR-coated windows. | 54 |
| Figure 1.25 Produced Heat Mirrors | 56 |
| Figure 1.26 Humidity Responses of DBRs. | 59 |
| Figure 1.27 PSRB Schematic for Energy Storage and Production using titanium oxide hydrates | 61 |
| Figure 1.28 Absorption changes upon UV-irradiation of polyalcohol hybrids. | 62 |
| Figure 1.29 FTIR changes upon UV-irradiation of polyalcohol hybrids. | 63 |
| Figure 1.30 Proposed Intermolecular Interactions of Polyalcohol hybrids. | 63 |
| Figure 2.1 Mettler Toledo Flash DSC 1. | 68 |
| Figure 2.2 Physical Aging. | 70 |
| Figure 2.3 Multi-level microstructural features of Conjugated Polymers. | 72 |
| Figure 2.4 Bulk Heterojunction Architecture Schematic. | 74 |
| Figure 2.5 Glass Transition Temperatures of UV-aged PCDTBT. | 78 |
| Figure 2.6 Evolution from Semi-crystalline to long, rigid chain microstructure. | 79 |
| Figure 2.7 Heating and Cooling Curves of pBTTT-C16. | 81 |

| | |
|--|-----|
| Figure 2.8 Physical Aging Signature of pBTTT-C16..... | 81 |
| Figure 2.9 Fullerene Derivative Intercalation in pBTTT-C16..... | 84 |
| Figure 2.10 Fullerene Intercalation into pBTTT-C16..... | 86 |
| Figure 2.11 Comparison of Side-chain Ordering to Backbone Ordering in Ketolactam:pBTTT Blends..... | 87 |
| Figure 2.12 Glass Transitions of IDT Copolymers with different backbone torsion | 88 |
| Figure 2.13 Side-chain and liquid-crystalline-like ordering of IDT copolymers. | 90 |
| Figure 2.14 Physical Aging of Planar IDT Copolymers..... | 91 |
| Figure 2.15 Glass Transitions of Planar IDT Copolymers. | 92 |
| Figure 2.16 Annealing of Planar IDT Copolymers..... | 93 |
| Figure 2.17 Molecular Weight Dependence of Liquid-Crystalline-Like Phase of PIDTBT. | 94 |
| Figure 2.18 OECT Schematic..... | 96 |
| Figure 2.19 ProDOT Series Structures Investigated..... | 97 |
| Figure 2.20 Physical Aging of Linear Spaced ProDOTs..... | 98 |
| Figure 2.21 Physical Aging of Branched Spaced ProDOTs. | 100 |
| Figure 2.22 Physical Aging of Fully Decorated ProDOTs. | 101 |
| Figure 2.23 Relationship between the Glass Transition Temperature and Length of Side-Chain in ProDOTs..... | 103 |
| Figure 2.24 Normalized absorbance of fully reduced and fully oxidized ProDOTs. | 104 |

| | |
|---|-----|
| Figure 2.25 Electrochemical Doping and dedoping versus time of ProDOTs. | 106 |
| Figure 2.26 Time constants electrochemical doping and dedoping of ProDOTs. | 107 |
| Figure 2.27 Electrochemical doping and dedoping completion times..... | 108 |
| Figure 2.28 Time constants electrochemical doping and dedoping of ProDOTs in aqueous solution..... | 109 |
| Figure 2.29 MAF and RAF Phases. | 111 |
| Figure 2.30 Annealing and Aging Protocol for Side-chain crystal ordering. | 112 |
| Figure 2.31 MAF and RAF Evidence in PIDBT. | 113 |
| Figure 2.32 Vitrification Kinetics Protocol of PA12..... | 116 |
| Figure 2.33 Vitrification Kinetics of PA12..... | 117 |
| Figure 2.34 Isothermal Aging Protocol of PA12..... | 119 |
| Figure 2.35 Crystallization and Nucleation of PA12..... | 120 |
| Figure 2.36 Characteristic Time of Crystallization of PA12. | 122 |
| Figure 2.37 Physical Aging Signature of P3HT:PVDF 75:25 Blend | 124 |

List of Tables

| | |
|---|-----|
| Table 1.1. Cauchy Coefficients of Hybrids | 21 |
| Table 1.2 Commodity Polymers | 38 |
| Table 2.1 ProDOT Series Data Table. | 102 |

1 Hybrid Materials in Optics and Photonics

1.1 Introduction

Plastics have revolutionized consumer products which has led to an exponential growth since the 1950s.¹ The optics and photonics industries are no exception, with polymers being used in waveguides, fiber optics, and many other applications due to their low optical loss.^{2,3} One of the main characteristics of materials in optics is the refractive index, n . The refractive index of materials is controlled by their bond polarizabilities and packing, and polymers have relatively weak attributes of both leading to refractive indices between 1.3-1.7.⁴ The Lorentz-Lorenz Equation was developed to predict the refractive index of polymers as a function of chemical composition, which functional groups of higher molar refractions leading to larger refractive indices.⁵⁻⁷ Thus, there many synthetic efforts to increase the refractive index through to incorporation of high molar refraction substituents like sulfur, phosphorus, and halogens.⁸⁻¹⁰ However, issues in unwanted absorption may occur in these polymers. As a way to circumvent complex polymerizations, inorganic nanoparticles have been added to commodity plastics as a way to increase the refractive index.

Inorganic nanoparticles have been utilized for centuries, due to their unique optical properties.¹¹ A nanoparticle is, in its most generic definition, a particle with a diameter in the nanometer scale (under 100 nm). However, a more stringent definition is a particle whose properties depend directly on its size. The applications of inorganic-organic polymer nanocomposites are extremely vast (optics, microelectronics, photovoltaics) since there are a countless number of combinations of particles and polymers. In addition to the numerous

properties that these nanocomposites can possess, there are also several fabrication techniques that can be utilized.¹² Fabrication of inorganic materials like silicon, gold, and metal oxides for electronics can suffer from high processing costs. Organic materials can, in contrast, be deposited at low temperatures and over large areas via solution processing.¹³ Solution processing (sol-gel processing) is attractive because of potential easy scale-up capabilities to large area printing via roll-to-roll processing. Being able to deposit inorganic-organic hybrid materials at low temperatures will reduce the overhead costs.

Incorporation of an inorganic component into a polymer matrix allows for the tailoring of the refractive index for the bulk material.^{12,14,15} However these inorganic components commonly create optical loss via Rayleigh scattering if they are larger than roughly one-tenth of the wavelength of interest. The intensity of light lost due to scattering can be estimated by Eq. 1.1:

$$\frac{I}{I_0} = \exp \left[\frac{-32\phi_p x \pi^4 r^3 n_m^4}{\lambda^4} \left(\frac{\left(\frac{n_p}{n_m}\right)^2 - 1}{\left(\frac{n_p}{n_m}\right)^2 + 2} \right)^2 \right] \quad (1.1)$$

Where n_p and n_m are the refractive index of the inorganic component and polymer matrix, respectively, ϕ_p is the volume fraction of the particle, x is the optical path length, and λ is the wavelength of light.¹¹ Thus, the larger loading of inorganic nanoparticles leads to more scattering losses.

In thin films, <500 nm, the losses due to Rayleigh scattering are limited, however, in the case for more complex optic and photonic structures where multilayers are involved, the amount of scattering increases exponentially. Applications thus benefit most from particle diameters under ~5 nm. In an effort to reduce scattering losses, this chapter focuses on the

creation of a molecular hybrid between the inorganic and organic components that no longer creates a refractive index boundary and therefore will not experience diffuse scattering losses. The material of interest is the a titanium oxide hydrate:poly(vinyl alcohol) molecular hybrid produced using a pseudo-one-pot solution processing method.

1.2 Materials and Methods

1.2.1 Materials and Instruments

Poly(methyl methacrylate) (PMMA) was purchased from Sigma-Aldrich with a weight average molecular weight, $M_w = 120,000$ g/mol. Toluene ($\geq 99.5\%$) was purchased from Sigma-Aldrich. Solutions of PMMA were prepared to a concentration of 4-8 wt% PMMA in toluene by dissolution at 80 °C under vigorous stirring for at least 2 hours until fully dissolved. The resulting PMMA solution is then stable at room temperature for several months.

Glass substrates are 3"x1" microscope slides purchased from VWR. Slides cleaned in a sonication bath with acetone and isopropanol for 15 minutes each and then quickly dried with nitrogen. Undoped silicon wafers with a crystal orientation of <100> purchased from University Wafer are cleaned similarly to glass substrates, but after sonication, are placed in a UV-ozone chamber from Novascan for 10 minutes.

Spin coating is performed using a Laurell Technologies spin coater. The spin rate and spin time are varied based on the desired thin film thickness and solvent vapor pressure, respectively. The fast solvent evaporation leads to a more kinetically trapped polymer film, which is desirable for amorphous materials.

Dip coating is performed using Biolin Scientific KSV NIMA dip coaters. The draw rate from solution is varied based on desired thin film thickness. The relatively slow draw speeds are suitable for reproducible film thicknesses.

Differential Scanning Calorimetry was performed using a Mettler Toledo DSC3+ instrument. Measurements were performed under nitrogen in sealed aluminum crucibles with punctured lids to allow evaporated gases to escape. Heating rate, temperatures, and number of cycles are dependent on the material of interest. All heat flow curves from DSC are reported with endotherms pointed up, unless otherwise noted.

Thermogravimetric analysis (TGA) was performed using a Mettler Toledo TGA/DSC 3+ instrument. Measurements were performed under nitrogen in an open alumina crucible. Heating rate and maximum temperatures are dependent on the material of interest. All heat flow curves from TGA/DSC 3+ are reported with endotherms pointed up, unless otherwise noted.

Transmission and absorption spectra were measured with an Agilent Cary 5000 UV-Vis-NIR spectrophotometer. The measurements were performed using a double beam photometric system with both the liquid and thin film sample holders. Reference curves and wavelengths measured were dependent on measurement type and sample of interest.

X-ray Photoelectron Spectroscopy (XPS) was performed with a Thermo Scientific K-Alpha X-ray Photoelectron Spectrometer System. Samples are subjected to a monochromatic beam of x-rays, with a flood gun for charge compensation. The technique measured the thin film surface level with detection depth around 5 nm.

Fourier Transform Infrared Spectroscopy (FTIR) was performed with a Shimadzu Prestige 21 Fourier Transform Infrared Spectrometer with attenuated total reflection for measurement of films and liquids.

1.2.2 Titanium Oxide Hydrate:PVA Hybrid

The Titanium oxide hydrate:poly(vinyl alcohol) (PVA) hybrid is made using a pseudo-one-pot solution processing method. PVA is dissolved in water and the titanium oxide hydrate is formed through the hydrolysis of titanium tetrachloride. The preparation of these solutions and mixing procedure is described below.

Poly(vinyl alcohol) (PVA) was purchased from Sigma-Aldrich. PVA has the product name Mowiol® 18-88 which is approximately 88% hydrolyzed, with the other 12% representing residual acetyl groups and has a weight average molecular weight, $M_w = 130,000$ g/mol. Solutions of PVA in water are prepared at a concentration of 4 wt% PVA by dissolution of PVA into water and heated to 85 °C under vigorous stirring for at least 2 hours until fully dissolved. The resulting PVA solution is then stable at room temperature for months.

Titanium oxide hydrates (TiOH) are formed from the hydrolysis of $TiCl_4$ purchased from Sigma-Aldrich at a purity of 99.9% trace metal basis. The hydrolysis is highly exothermic and fast, therefore, $TiCl_4$ is dropped slowly (~1 drop/second) into a round bottom flask of water, submerged in an ice bath. The final concentration of Ti was between 0.5 M and 2 M depending on the desired viscosity of the final hybrid solution. The hydrolysis assumed to not produce a 100% yield, and has the nonstoichiometric reaction form:



The hydrate is stable for several months when stored in a freezer below 0 °C to avoid further condensation to titanium dioxide nanoparticles.

Hybrid solutions are prepared through mixing of the PVA solution with the TiOH solution to the desired concentration. Desired concentrations, in vol% Ti of the resulting solid state hybrid film are calculated through:

$$\begin{aligned}
 \text{vol\% Ti} &= 100 \left(\frac{V_{Ti \text{ species}}}{V_{Ti \text{ species}} + V_{PVA}} \right) \\
 &= 100 \left(\frac{n_{Ti} (M_{Ti \text{ species}} / \rho_{Ti \text{ species}})}{n_{Ti} (M_{Ti \text{ species}} / \rho_{Ti \text{ species}}) + V_{PVA}} \right) \\
 &= 100 \left(\frac{46.2 C_{Ti}}{46.2 C_{Ti} + 0.794} \right)
 \end{aligned} \tag{1.2}$$

Where C_{Ti} is the concentration in *mol Ti/g PVA*, thus considering 1 g of PVA. This relation is taken from Russo et al.¹⁴, that shows the titanium species has a density of 1.95 g/cm³ and a molar mass of 90 g/mol.

Hybrid solutions are only considered stable for roughly 12 hours at room temperature and are sensitive to heat. Solutions are not to be heated as it leads to white scattering points and yellow-tinted solutions attributed to titanium oxide aggregation and PVA degradation, respectively. After mixing of the solution to the desired concentration, the hybrid is deposited using solution processing techniques including spin coating, dip coating, and drop-casting. After solution processing and prior to any additional annealing or washing, hybrid films are stored for a minimum of 5 days under vacuum to remove residual water and HCl.

1.2.3 Optical Modeling

Calculations of the refractive index and thickness of thin films are done so using a home-built MATLAB software that utilizes the Transfer Matrix Method (TMM). Relevant physical parameters and equations are discussed below.

Maxwell's equations can describe the propagation of the electric field through some medium as^{16,17}:

$$E = \epsilon \exp[i\omega t - (2\pi N/\lambda)x] \quad (1.3)$$

Where ϵ is the vector amplitude of a wave propagating along the x-axis with a wavelength λ and the angular frequency, ω . N is defined as the complex refractive index and can be written as:

$$N = n - ik \quad (1.4)$$

The real part n is often simply called the refractive index, while the imaginary part k is the extinction coefficient. n is also defined by the speed of light in a dielectric medium such as $n=c/v$ where c and v are the speeds of light in vacuum and the medium, respectively. All references to refractive index, n , in this thesis refer to this definition, and reports of the refractive index of processed films are reported only as the real part. k is a measure of the absorption in the medium. The amplitude of the wave falls to $1/e$ of its initial value after propagating for a distance of $\lambda/2\pi k$ which is also known as the absorption coefficient α (in cm^{-1}).

Using these definitions, Equation 1.3 can be restated as:

$$E = \epsilon \exp(-\alpha x) \exp[i\omega t - (2\pi n/\lambda)x] \quad (1.5)$$

The second exponent of Equation 1.5 is representative of the change in phase of the wave having travelled a distance x in the medium. For ease of calculation, the absorption coefficient, α , is assumed to be zero across the visible and near-IR range. This assumption is reasonable considering PVA, PMMA, and titanium dioxide do not absorb in either of these ranges. Since α is assumed to be zero, $\exp(-\alpha x)=1$, so the propagating wave is only dependent on the real part of the refractive index, n .

Description of the propagating wave within a medium, is not fully descriptive of a thin film system, as the boundaries between medium also affect the wave. When two media with different refractive indices are in contact, common in thin-film optics, a plane wave is partly transmitted and partly reflected. Furthermore, the intensity of the transmitted and reflected waves depends on the polarization and angle of the incident light. However, for normal incidence, the transmittance and reflectance are independent of the polarization, and derivations from this point on will only consider normal incidence. The assumption of normal incidence is valid in our system because the Cary UV-Vis-NIR Spectrophotometer measures thin film transmission at normal incidence. Reflection in this instrument is measured at 8 degrees relative to normal. Expansions to the built software can include considerations like polarization and angle. The following equations describe the reflection and transmission coefficients at normal incidence, and are generally known as the Fresnel equations:

$$R = \left(\frac{n_0 - n_1}{n_0 + n_1} \right)^2 \quad (1.6)$$

$$T = \frac{4n_0n_1}{(n_0 + n_1)^2} \quad (1.7)$$

Where R is the reflectance power, and T is the transmittance power, which are both ratios to the incident power, and therefore equal to or less than 1. n_0 and n_l are the refractive indices of the incident medium and the transmitted medium, respectively.

Due to the law of conservation of energy, we have:

$$1 = T + R + A \quad (1.8)$$

Where A is the absorptance, not to confused with absorption or extinction coefficients, and is also the ratio of absorbed irradiance to incident irradiance. With the systems discussed in the thesis, like mentioned prior, A is assumed to be zero since absorption and extinction coefficients are zero as materials do not absorb over the wavelengths of interest.

The Fresnel Equations, help describe the optical response of a semi-infinite layer, which is similar to a glass substrate. This is due to the optical thickness (nd) of the glass substrate, ~ 1 mm, which is much larger than the coherence length (λ) of the light source, ~ 400 - 1000 nm. The thickness variations of a substrate are also most likely too large or irregular to induce coherent interference effect, thus deemed an incoherent medium. However, when the optical thickness is in a similar range as the coherence length, like in polymer thin films, it is considered a coherent layer and interferences should be considered.

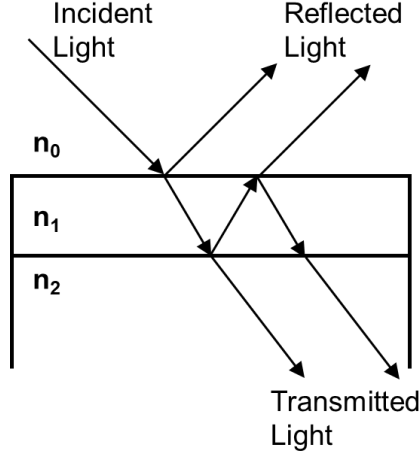


Figure 1.1 Schematic of the Thin Film Case Incident light is reflected multiple times within the coherent layer, n_1 . Without absorption events, then the summation of the reflected light intensity and transmitted light intensity equal that of the incident light intensity.

Figure 1.1 shows a system with two boundaries, with the layer of refractive index, n_1 , is a coherent layer, and n_0 and n_2 are incoherent layers. For the purpose of the experiment, n_0 is the refractive index of air (~ 1) and n_2 is the glass substrate. Boundaries of the coherent layers cause a phase shift, δ , of a wave travelling through this thin-film described by:

$$\delta = 2\pi n d \cos \theta / \lambda \quad (1.9)$$

where θ is the angle of incidence of the wave, thus, $\cos \theta = 1$ at normal incidence.

Incident light bouncing in the thin-film results in multiple transmitted and reflected waves at each interface creating in-phase and out-of-phase waves at particular wavelengths. The transmitted and reflected waves have oscillating intensities between these specific wavelengths and are referred to as Fabry-Pérot oscillations.

These oscillating transmittance and reflectance intensities are relatively easy to measure by UV-Vis spectroscopy and carry several characteristics such as the refractive index, thickness, and optical loss. Figure 1.2 shows model transmittance spectra of two films on

glass substrates with varying refractive indices and thicknesses. In these models, glass is assumed to have refractive index of 1.5.

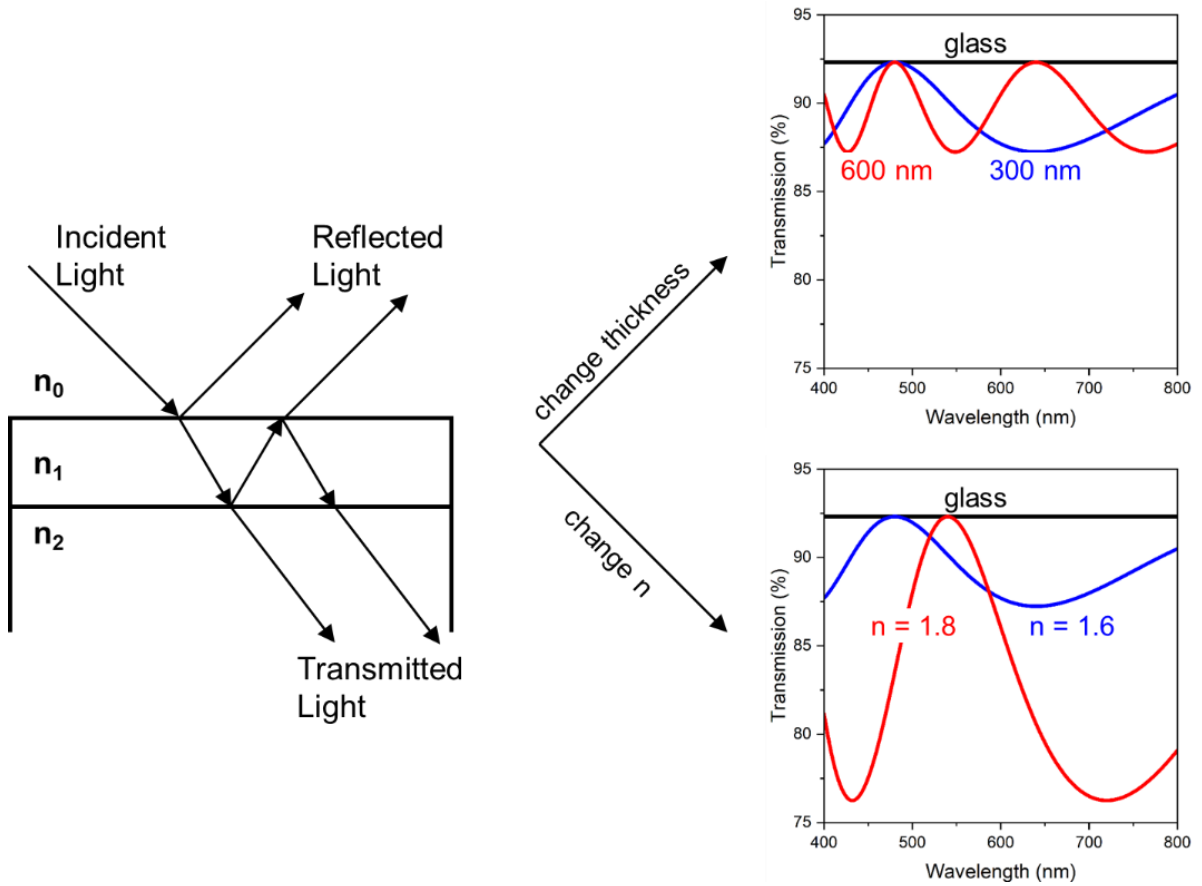


Figure 1.2 Fabry-Pérot Oscillations in High Refractive Index Layers. When a transparent, coherent layer is deposited on a glass substrate, oscillating transmission spectra occur if the layer has a different refractive index than glass. Thicker layers of the same refractive index show shorter oscillating periods. Larger refractive index layers show increased oscillation amplitudes. If no optical loss occurs, then the oscillation maxima overlap with the transmission of the substrate. If the coherent layer has a refractive index lower than glass, then oscillation occurs above the glass line, with smaller refractive indices possessing larger amplitudes.

The increase in physical thickness of the film results in a smaller period of transmission oscillation, due to the quarter-wave and half-wave boundaries occurring twice as frequently. The increase in refractive index from 1.6 to 1.8 increases the amplitude of the oscillations. The minimum and maximum of the oscillations do not align at the same wavelengths because the quarter- and half-wave thicknesses are dependent on optical

thickness which is nd . If the refractive index, n_1 , was lower than the n_2 then oscillations in transmission would occur over the glass substrate line. Finally, these oscillations can give an indication of the optical loss of the film. A film with no optical loss will have maxima in the oscillations reach the glass substrate line. A drop in these maxima below the substrate line is due to non-zero absorption coefficients or diffuse scattering. Absorption will show an overall vertical shift in the oscillations depending on the magnitude of the coefficient in the wavelengths of interest. Diffuse, or Rayleigh, scattering will have a drop in intensity proportional to $1/\lambda^4$.

The electronic (E) and magnetic (H) components a wave passing through coherent layer can be described as:

$$\begin{bmatrix} E_{0-1} \\ H_{0-1} \end{bmatrix} = \begin{bmatrix} \cos \delta & (i \sin \delta)/n_1 \\ in_1 & \cos \delta \end{bmatrix} \begin{bmatrix} E_{1-2} \\ H_{1-2} \end{bmatrix} \quad (1.10)$$

Where the subscript $0-1$ describes the boundary between n_0 and n_1 , and the subscript $1-2$ describes the boundary between n_1 and n_2 . Dividing Equation 1.10 by E_{1-2} gives:

$$\begin{bmatrix} E_{0-1}/E_{1-2} \\ H_{0-1}/E_{1-2} \end{bmatrix} = \begin{bmatrix} X \\ Y \end{bmatrix} = \begin{bmatrix} \cos \delta & (i \sin \delta)/n_1 \\ in_1 & \cos \delta \end{bmatrix} \begin{bmatrix} 1 \\ n_2 \end{bmatrix} \quad (1.11)$$

Where X and Y are substituted for simplicity. The resulting transmittance and reflectance intensities can now be described as:

$$T = \frac{4n_0 \text{Re}(n_2)}{(Xn_0 + Y)(Xn_0 + Y)^*} \quad (1.12)$$

$$R = \left(\frac{Xn_0 - Y}{Xn_0 + Y} \right) \left(\frac{Xn_0 - Y}{Xn_0 + Y} \right)^* \quad (1.13)$$

The 2x2 matrix in Eq 1.11 is called the characteristic matrix, M_j , and describes the coherent layer j .

$$M_j = \begin{bmatrix} \cos \delta_j & (i \sin \delta_j)/n_j \\ in_j & \cos \delta_j \end{bmatrix} \quad (1.14)$$

In the case of multiple coherent layers stacked together in one structure, like depicted in Figure 1.3, a characteristic matrix exists for each coherent layer.

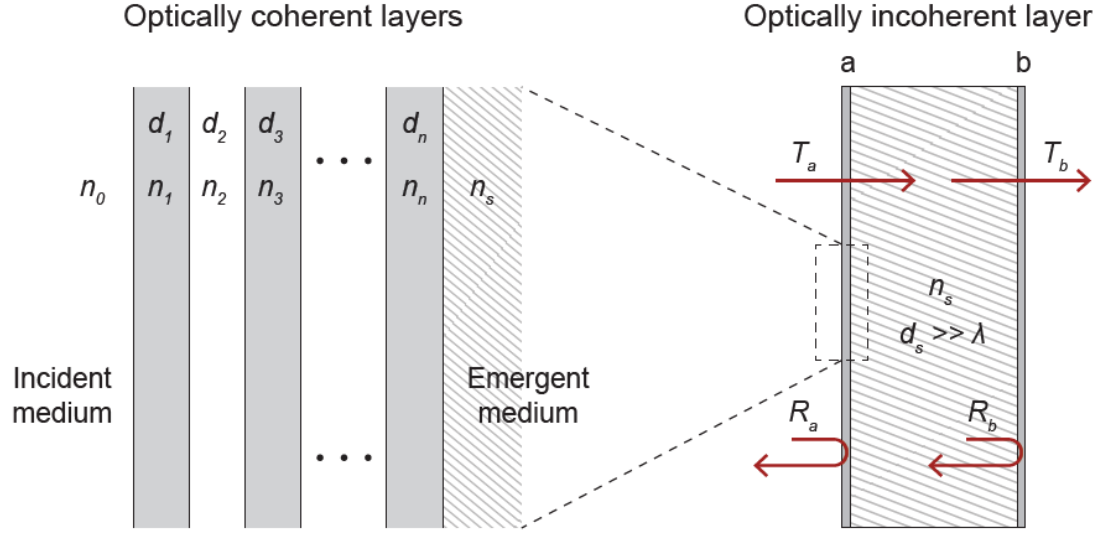


Figure 1.3 Multilayered Coherent Structure Schematic depicted a thin-film arrangement of several, transparent coherent layers stacked together on top of an incoherent layer. The transmitted intensity is a function of all of the layers together. Image credit: Stefan Bachevillier.

This characteristic matrix approach can describe each coherent layers in sequence and the total transmittance and reflectance intensities can be calculated at once using:

$$\begin{bmatrix} X \\ Y \end{bmatrix} = [M_1][M_2] \dots [M_n] \begin{bmatrix} 1 \\ n_s \end{bmatrix} \quad (1.15)$$

This is known as the Transfer Matrix Method (TMM) and is highly useful in calculating the spectra of multilayers structures.

Considering the UV-Vis set-up requires the incident beam to exit the substrate layer into air, additional interfaces occur and can be calculated. The TMM will describe the optical response of coherent layers in a multilayered structure, however it does not describe the

incoherent part. The transmitted intensity for an incoherent layer is considered an infinite sum of each wave and can be expressed as a function of the transmittance through the first and second interfaces (interfaces a and b in Fig. 1.3). The consecutive reflected wave can be added to form a series summed to infinity and solved to arrive at:

$$T = \left(\frac{1}{T_a} + \frac{1}{T_b} - 1 \right)^{-1} \quad (1.16)$$

$$R = \frac{R_a + R_b - 2R_a R_b}{1 - R_a R_b} \quad (1.17)$$

assuming the incoherent layer has no optical loss. Thanks to the flexibility and ease of TMM, each interface of the incoherent layer can contain coherent multilayered structures and the optical response of the total system is still calculatable. Furthermore, the refractive index of materials is dependent on the wavelength, and one relation that describes the polymer and hybrid films with reasonable accuracy is the Cauchy Equation:

$$n = A + \frac{B}{\lambda^2} \quad (1.18)$$

Where A and B are unitless coefficients and λ is the wavelength in microns. B describes the dispersion of the refractive index which is related to often reported Abbe numbers and is also assumed to always be positive as the refractive index for these materials should increase with decreasing wavelengths. However, the refractive index of glass is not accurately described by the Cauchy Equation and therefore takes the form¹⁸:

$$n = A + \frac{B}{\lambda^2} + C\lambda^2 \quad (1.19)$$

A screenshot of the MATLAB app designed to solve the TMM is depicted in Fig. 1.4.

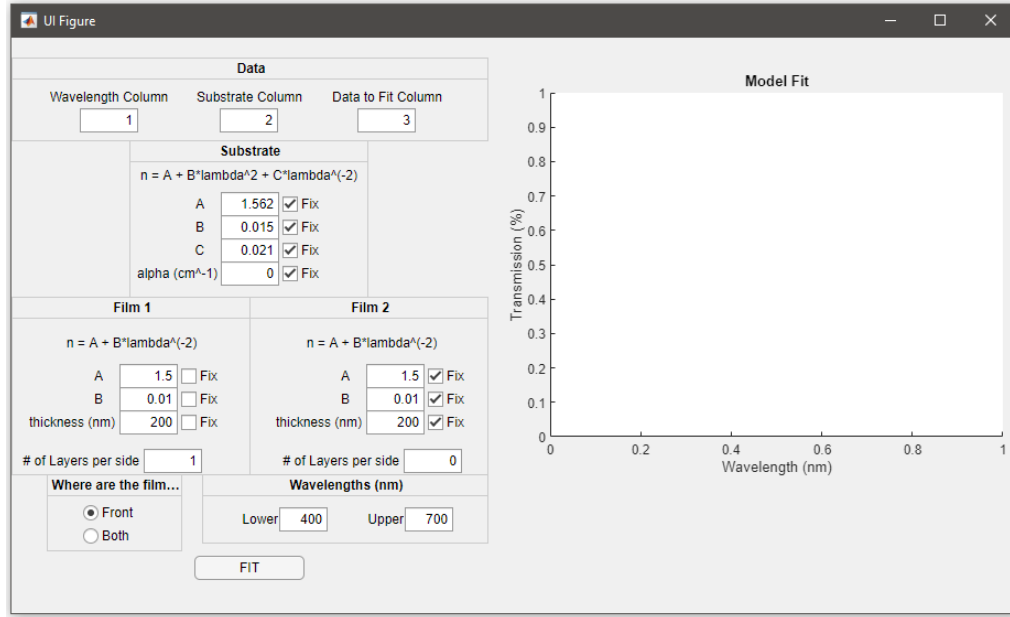


Figure 1.4 MATLAB App for TMM Screenshot of home-built code for calculating the refractive index and thickness of multilayered structures.

The MATLAB code will solve for the refractive index and physical thickness for any periodic multilayered structure. The assumptions of lossless thin films and substrates along with Cauchy Equation fits are used throughout this thesis. Expansions to the MATLAB solver for the TMM can include nonzero extinction coefficients and diffuse scattering losses, as well as angle dependent measurements.

1.3 Titanium Oxide Hydrate:PVA Hybrids

One of the most common inorganic materials as fillers in organic matrices is titanium dioxide, TiO_2 or titania.^{15,19,20} Titania is an extremely versatile material which is used in paints and ceramics as a pigment, healthcare products as antimicrobial coatings, and in photocatalysis and photovoltaics.²¹ Titania has several crystal forms, each with their own properties: bulk anatase is characterized by a refractive index of 2.54 (at 550 nm) and a band gap energy of 3.20 eV, bulk rutile is characterized by a refractive index of 2.75 (at 550 nm) and a band gap energy of 3.03 eV, and amorphous TiO_2 is characterized by a

refractive index of 2.51 and band gap energy of 3.27 eV.²² The refractive index of nanoparticles is known to decrease with decreased particle diameter¹², and anatase titania was found to be more stable than rutile when particle size dropped below 14 nm.²³ There are several ways to produce titania thin films and nanoparticles, including sol-gel, chemical vapor deposition, hydrothermal, and ion cluster beam.^{24,25} However, with the exception of sol-gel processing, these processes typically require high temperatures and/or vacuum level pressures. Thus, the production of hydrous titania via sol-gel processing is investigated in this thesis. Hydrous titania has been studied for over 100 years.²⁶ Titanium tetrachloride and titanium tetra-alkoxides are typical precursors to the production of TiO₂ via sol-gel processing, but their intermediate, titanium oxide hydrate, has not led to detailed research into its composition. Amorphous titania is produced using a hydrolysis method but not if heat is added.²⁶ Titanium oxide hydrates are thus given a chemical formula as TiO_x(OH)_y(Cl)_z, with x=1 indicating a mononuclear species, and x≥2 for the polynuclear species, each of which having unique optical characteristics.²⁷ The distinction between mononuclear and polynuclear species is important due to their different photochromic response and potentially different light scattering response.

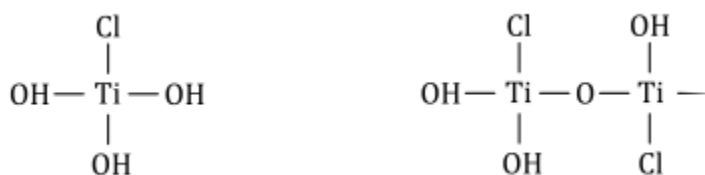


Figure 1.5 Representation of Mono- and Poly-nuclear Titanium species. Mononuclear titanium oxide hydrate (left) contains only 1 Titanium atom while polynuclear titanium oxide hydrate (right) contains multiple titanium atoms. Residual chloride is possible in each structure due to the incomplete hydrolysis reaction.

When adding the hydrates to poly(vinyl alcohol) (PVA) that has been predissolved in water; and casting as a film of this hydrolysis solution with PVA via spin coating or dip

coating, the result is a very versatile hybrid. There is no optical loss even when the volume fraction of titanium oxide hydrates reaches close to 100%, i.e. there is no loss due to scattering, and refractive indices of 1.5-1.9 were demonstrated with these materials.¹⁴ However, the exact relationship between the titanium and polymer has not been extensively studied. The hydroxyl groups on the titanium oxide hydrate are proposed to act as crosslinkers for the polymer through strong hydrogen and likely, covalent bonding with its hydroxyl groups.²⁸ The organic molecule may indeed act as a chelating agent with the hydrate, since the mixture of it with glycerol produces a stable and transparent solution.²⁷ First, the titanium oxide hydrate:PVA hybrid must be produced and proven to be a highly transparent material before moving into the physical and chemical investigations.

1.3.2 Low Optical Loss Materials

Exceptional optical properties in hybrids and nanocomposites comes from the more intimate mixing of the two components. Better mixing can lead to fewer interfaces that cause scattering losses. The high hydroxyl group density of PVA along with the sub-nanometer-sized titanium oxide hydrate is prime for intimate mixing thus reducing potential titanium oxide aggregation. If the titanium species remains as extremely small particles homogeneously mixed throughout a PVA matrix, then the interfaces will be small enough to not affect optical properties. The next step in mixing of the inorganic and organic components would be a covalently bonded network known as a molecular hybrid. Molecular hybrids will have no interfaces between the two components and thus no scattering points making it the ideal optical material.

To assess the efficacy of a nanocomposite or hybrid, one of the easiest ways is to measure the thin film transmission. The transmission curve can immediately inform you on any

optical losses including diffuse scattering and absorption. The TiOH:PVA hybrids have a unique transmission curve seen in Figure 1.6. Both 30% and 60% hybrids show Fabry-Perot oscillations like mentioned in Section 1.2.3. When measuring the transmission of optically transparent films, it is critical to measure of everything in comparison to the glass substrate that supports the film. Glass itself does not have full 100% transmission due to its refractive index of ~ 1.5 , additionally, the transmission is slightly wavelength dependent due to its refractive index dispersion. If the optical film in question has the same or greater refractive index than the glass, then the total system cannot have a greater transmission than the glass alone. Optical films with lower refractive indices than glass will have oscillations occurring above the glass transmission, creating a pseudo-antireflective coating.

Hybrid film oscillations exist below the glass transmission line and therefore will have higher refractive indices than glass. Additionally, the maxima of the oscillations reach that of glass which indicates no optical loss due to absorption or scattering. The depths, or amplitudes, of oscillations increase with titanium content as well, confirming an increase in refractive index. Hybrid films refractive indices and dispersions are model with the Cauchy Equation, and Figure 1.6 shows good agreement between the raw data (solid lines) and model fit (dotted lines). Table 1.1 details the Cauchy coefficients for several titanium content hybrids.

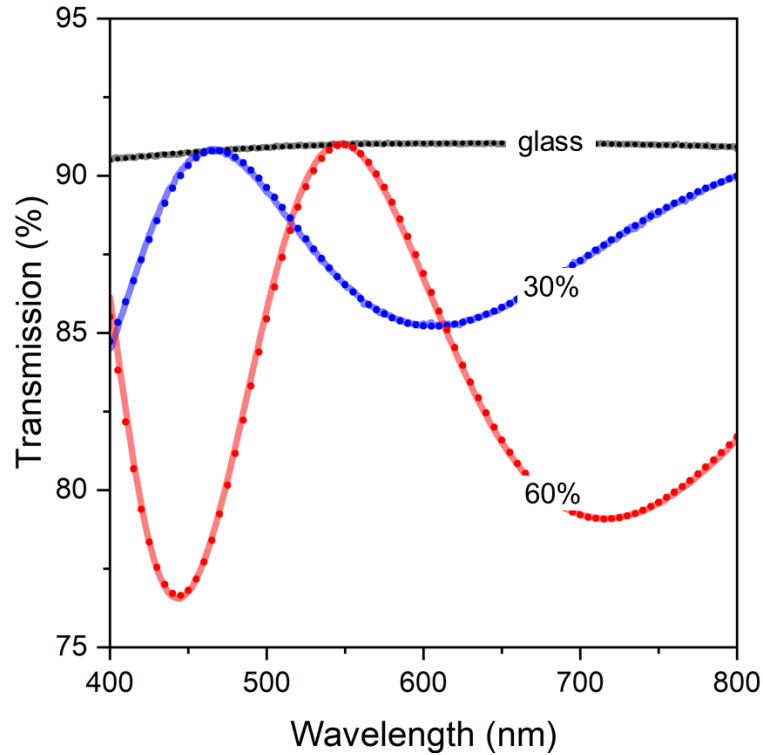


Figure 1.6 Optical Transmission of Hybrids. Oscillations in the transmission curves indicate the hybrids are highly transparent and have high refractive indices. 30 vol% Ti hybrids (blue line) show a smaller amplitude than the 60 vol% Ti hybrids (red line) highlighting the increase in refractive index of the 60 vol% Ti hybrid. Dotted lines are the TMM model fits and show good agreement with the data.

The Fabry-Perot oscillations help show the high transparency of the hybrids however can only qualitatively measure the optical losses as it is limited by the TMM code built. To assess optical losses, in accordance with the law of conservation of energy, reflection can provide insight. If the total reflection summed with the transmission is equal to 100% then there is no absorption losses. Then the reflection can be broken into specular and diffuse, and similarly, if the specular reflection and transmission total 100% then no diffuse scattering occurs. Figure 1.7 shows the transmission as well as the specular reflection of hybrid films between 25% and 90% titanium. The specular reflection increases as the transmission decreases which is consistent with a refractive index increase. Additionally, the total between the transmission and reflection equals roughly 100% across the visible

range. Some slight deviations from 100% are seen, however the reflection measurement is done at 8 degrees compared to normal incidence. The transmission and reflection is angle dependent, and therefore, deviations from 100% are attributed to this artifact.

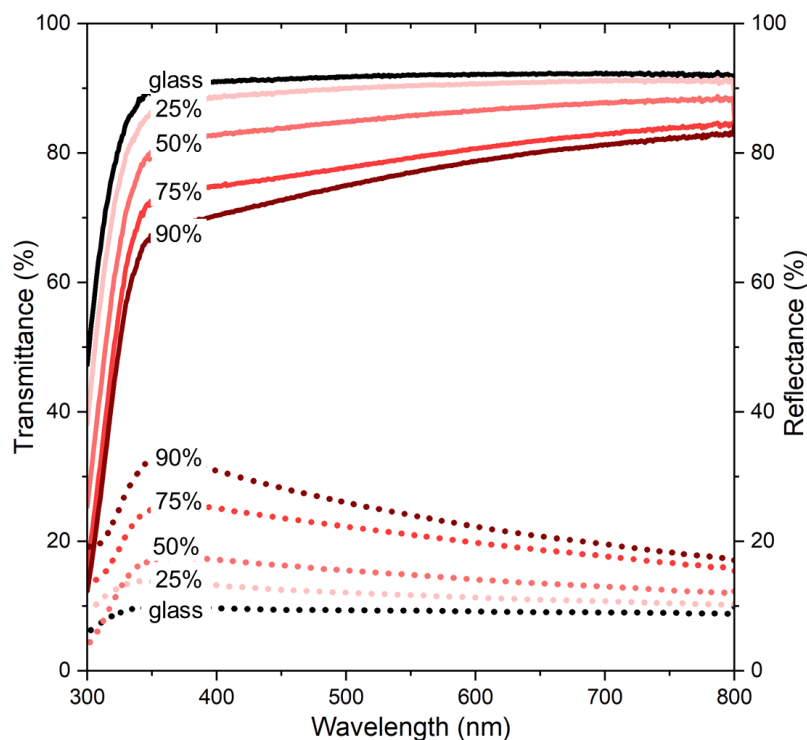


Figure 1.7 Transmission and Reflection of Hybrids. Solid lines show the transmission curves of several vol% Ti hybrids. Dotted lines show the specular reflection curves of the same films. Oscillations are not as apparent due to the sample thickness. In all cases, summation of transmission and reflection equals about 100%. Absorption losses are seen starting in the UV range.

There is the start of an absorption band near 350 nm for all hybrid compositions. The absorption band is due to the bandgap of the titanium species which is assumed to be similar to that of TiO_2 at ~ 3.2 eV.²² There is a slight shift to lower energies of this absorption band with titanium content which suggest the titanium species is getting slightly larger in diameter²⁹, not accounting for any residual chlorine. This diameter increase still does not affect the visible and near-IR transparency. With transmission, reflection, and absorption all considered, these materials can be labeled as little to no optical-loss hybrids.

1.3.3 Tunable Refractive Index

In the previous section, the high transparency of the hybrids is shown, but to further characterize and use these materials in optics and photonics, the range of refractive indices needs to be known. Table 1.1 shows the Cauchy coefficients for a wide range of titanium content hybrids.

Table 1.1. Cauchy Coefficients of Hybrids

| Material | Cauchy Coefficient | |
|------------|--------------------|-------|
| | A | B |
| PVA | 1.50 | 0.006 |
| 30 vol% Ti | 1.63 | 0.013 |
| 60 vol% Ti | 1.75 | 0.018 |
| 90 vol% Ti | 1.84 | 0.023 |

With titanium content increase, there is an increase in both Cauchy coefficients, A and B . An increase in A is consistent with an increase in the wavelength independent regime, and the increase in B states that the dispersion of the hybrids increases with titanium content. Generally, an increase in dispersion is seen when approaching the bandgap of the materials. Since there is a consistent shift to lower bandgaps seen in the absorption of the hybrids in Figure 1.7, this dispersion increase is expected. Dispersion can play a large role in optical fibers and waveguiding, with generally, lower dispersions being more favorable.² When sending a pulse of light through the fibers, a single wave packet which consists of a very fine wavelength range will spread out through the fiber as the wavelengths experience slightly different travel speeds. The dispersion of the fiber will dictate how much the wave spreads and therefore the maximum frequency of wave packets sent. A figure of merit for the dispersion of materials is the Abbe number which is the ratio between the Fraunhofer

spectral lines.^{30,31} A higher Abbe number means lower dispersion, and for the hybrids, the Abbe number decreases with increasing titanium content, and have a value between ~ 80 and ~ 10 . Figure 1.8a shows the refractive indices versus wavelength across the visible range, and generally there is a linear trend of refractive index with vol% titanium which is consistent with the Bruggemann effective medium theorem.³²

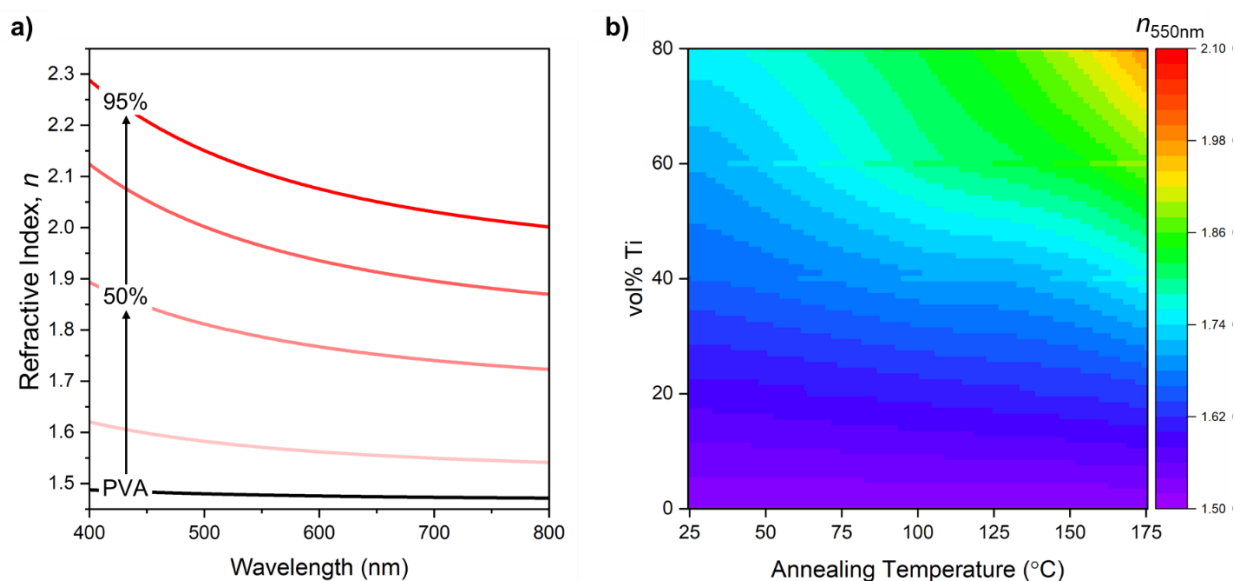


Figure 1.8 Tunable Refractive Index Hybrids (a) Refractive index increase with titanium content in the hybrids up to 95 vol% Ti. The refractive index is tunable up to nearly 2.3 in the visible range. (b) Annealing the hybrids leads to a further increase of refractive index due to the removal of residual chlorine in the material. Credit to Stefan Bachevillier and Andrew Strang to fill in more data points.^{33,34}

In addition to the refractive index increase with titanium content, post-deposition annealing also affects the refractive index. Figure 1.8b shows the 2D heatmap of the refractive index at 550 nm, for hybrids of varying titanium contents and annealing temperatures. For annealing temperatures below ~ 75 °C, the refractive index does not have a large change with increasing titanium content. The refractive index only varies between 1.5 and ~ 1.78 . However, with annealing temperatures around 150 °C, the refractive index varies between 1.5 and ~ 1.95 . This increased dependence of annealing temperatures, especially at high

vol% Ti hybrids suggests that there is a significant change in the material, likely from chemical reactions. Investigations into these changes are discussed in the next section. As long as the hybrid contains less than 95 vol% Ti and annealed under 175 °C, it's no optical-loss property remains, making it a highly versatile material for optics and photonics.

1.3.4 Physical and Chemical Investigations

The uniqueness of the highly transparent hybrids suggests very favorable interactions between the titanium species and PVA. Crosslinking through hydrogen bond intermolecular forces or even covalent crosslinking by the condensation of titanium species with the hydroxyl groups are both potential pathways. Crosslinking can affect several physical and structural characteristics of polymers, including the hydrophilicity, glass transition temperature, and thermal stability, and thus will be investigated to elucidate the interactions.

PVA is known for its pronounced hydrophilicity due to its high density of hydroxyl groups, which also imparts the water solubility. Water contact angle measurements highlight the hydrophilicity of PVA with an amplitude of roughly 33°. Any change in the chemical or physical interactions between the hydroxyl groups of PVA and the water droplet are expected to shift this. Higher hydroxyl group densities will lower the amplitude and hydroxyl group removal will increase the angle. Since the interactions between PVA and water are so strong, the water droplet will start to absorb into the PVA film, thus for consistency, the contact angle is measured as quickly as possible. To obtain an in-focus picture and measure the contact angle, this took about 30 seconds, thus all contact angle measurements are taken at the same time interval.

Even with 10 vol% Ti hybrids, there is an increase to 66° in the water contact angle which is double that of neat PVA. This large change suggests that several hydroxyl groups are interacting with the titanium species and therefore do not have the same affinity towards water. Further increase of titanium content appears to have a limited effect on the contact angle, with 90 vol% hybrids also around 66° . Annealing of the hybrids, leads to a slight increase in contact angle at most concentrations which suggests some additional crosslinking. With both neat PVA and neat TiO_2 being hydrophilic due to surface hydroxyl groups possible on nanoparticles, the contact angle of hybrids and nanocomposites are likely to be between the two.³⁵ The rate of change in the contact angle is not measured so absorption rates are not accessible. It is possible that the absorption of the water droplet happens at different rates between neat PVA and hybrids thus the change in water contact angle is more of a qualitative tool than a quantitative tool to measure exact changes in interactions.

In addition to changes in hydrophilicity, the thermal properties of hybrids are expected to change with titanium content. An increase in the elastic modulus can be expected, however, well defined thick films are difficult to create of the hybrids. Therefore, the glass transition temperature is only reported of the hybrids as it is not dependent on the raw moduli intensities, but instead of the ratio between the elastic and loss moduli. Both the neat PVA and hybrids are measured at a 0.02% strain, 10 Hz damping factor, and $3^\circ\text{C}/\text{min}$ heating rate on a parallel plate rheometer. The PVA shows a peak in the $\tan(\delta)$ at 78°C , which is similar to expected values.³⁶ Crosslinking polymers will lead to an increase in glass transition temperature (T_g).³⁷ Even just the 1 vol% Ti hybrid shows an increase in the glass transition of $\sim 16^\circ\text{C}$. Additionally 10% and 20% hybrids show even higher T_g increases up to 116°C and 141°C , respectively. The extremely large increase in T_g

suggests significant covalent crosslinking occurs, however, this still could be due to hydrogen bonding interactions between the PVA and titanium species. For example, polypropylene and PVA have T_g 's roughly 90 degrees apart which is due to the hydrogen bonding PVA has with increasing the barrier to segmental motion.³⁸

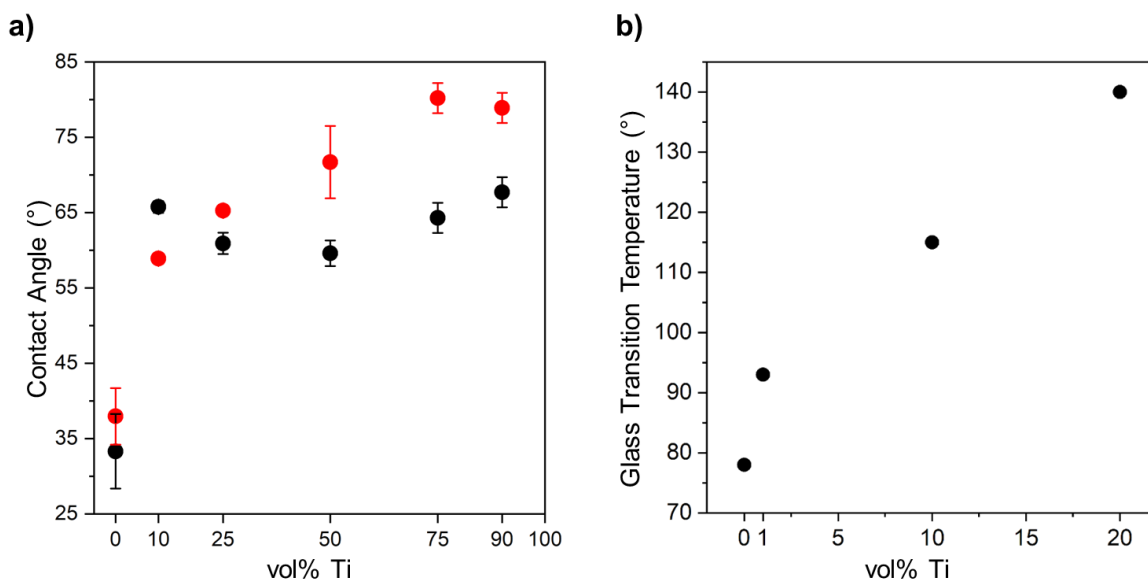


Figure 1.9 Evidence of Crosslinked Network. (a) Water contact angle measurements of as-cast (black) and 150 °C annealed (red) hybrids. (b) Glass transition temperature as function of vol% Ti measured via rheometry.

Improved hydrophobicity and increased glass transitions in thermal measurements suggest the crosslinking of hybrids. To gain further insight, DSC is performed to potentially measure similar glass transition temperatures and any other microstructural changes like crystallinity. Figure 1.10 shows both the first and second heating curves of drop-casted hybrids. For neat PVA, there are two prominent endotherms during the first heating, with the lower temperature attributed to absorbed water evaporation, and the higher temperature endotherm to crystal melting. A glass transition temperature is not very clear, with perhaps a small slope change occurring around 25 °C, which could be the glass transition of PVA

when plasticized by the water. Upon second heating, the glass transition temperature of PVA is clearly seen at 78 °C which is in agreement with the rheometer measurement.

Hybrids show 2-3 strong endotherms in the first heating scans, with the lower temperature endotherm increasing to slightly higher temperature with more titanium content. The slight increase in temperature is attributed to both water and HCl loss from the hybrids since HCl solutions boil at a slightly higher temperature. The higher temperature endotherms around 180 °C are not expected to be crystal melting, as the proceeding cooling curves of the hybrids show no corresponding exotherms of crystallization. Thus these endotherms are attributed to further chlorine loss, oxidation of titanium, and even crosslinking.

Second heating curves of hybrids are remarkably featureless, and with the known change in refractive index upon annealing, the hybrids have been effectively annealed up to 240 °C. The hybrids during the second heating are likely to be heavily crosslinked and/or slightly degraded samples, both of which can appear as featureless DSC curves. TGA will give further insight to evidence of degradation.

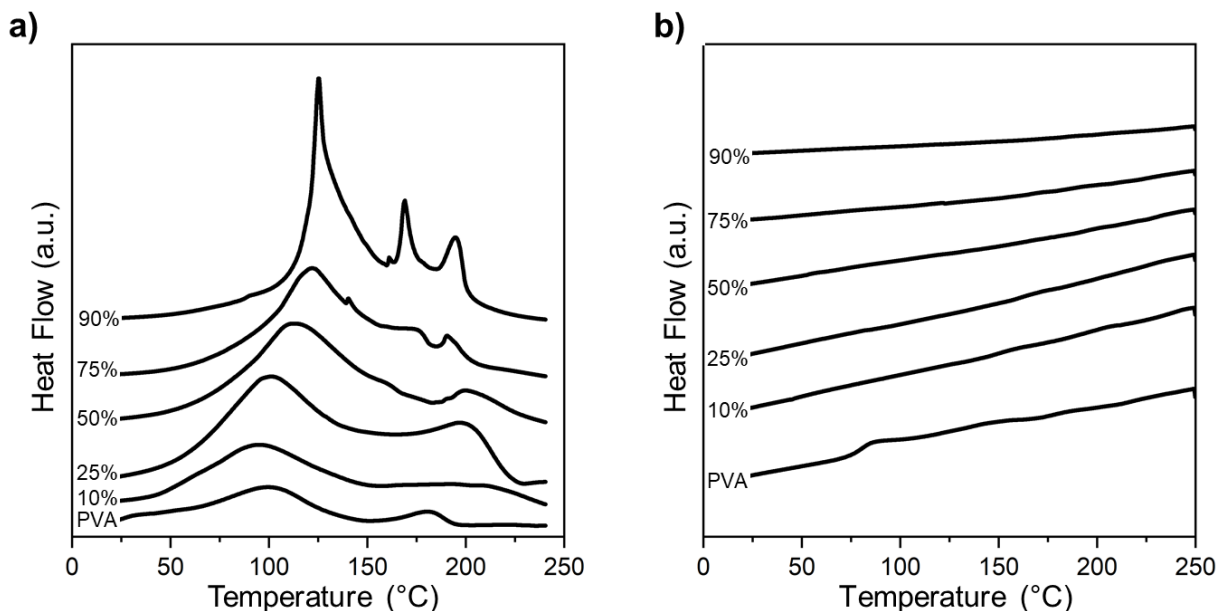


Figure 1.10 DSC of Hybrids (a) First heating scan of drop-casted hybrid samples. Large endotherms are attributed to mass loss and not phase transitions, with the exception of neat PVA crystal melting at 180 °C. (b) Second heating scan of drop-casted hybrid samples. All hybrids show featureless scans.

Thermogravimetric analysis (TGA) is highly useful in determining the degradation onset temperature of materials. For polymers, the degradation onset will increase with degree of crosslinking.^{39,40} This is generally attributed to the reduced reactivity of side-chains from the covalent crosslinks. PVA has been widely investigated using TGA and degrades through two steps. The first is elimination of the hydroxyl groups, and the second is degradation of polyene segments.^{41–43} Figure 1.11 shows the degradation of PVA in the black curve. There is an initial mass loss at 100 °C which is from water evaporation. Then the lower degradation step occurs around 250 °C and the second step at ~375 °C. The two-step degradation is crucial because it indicates the stability of hydroxyl groups.

Similar to the DSC, the hybrid materials have much richer TGA curves than neat PVA. First to note, at the high temperature range, above 500 °C, there is an increase in residual mass with increasing titanium content. There is not a linear increase in residual mass with

vol% Ti therefore the titanium species is expected to change, likely from the mononuclear to polynuclear structure with increasing titanium content. Worth noting however, is that drop-casted hybrid films to perform TGA do not form the same homogeneous morphology as spun-cast or dip-coated films. The water is not as easily evaporated and removed from the system, as it takes 24-48 hours for the drop-casted films to dry leading to large cracks and more titanium aggregation. Films with less than about 30 vol% Ti generally maintain the large, homogeneous transparency attributed to the comparatively large amount of hydroxyl groups available on the PVA leading to interaction between the species.

At low temperatures, the hybrids show a continuous loss of mass especially below 200 °C. This is attributed to chlorine loss from the incomplete hydrolysis of TiCl_4 . Loss of chlorine, and therefore oxidation of titanium is consistent with the increase of refractive index with annealing temperature. Around 400 °C, there is a loss of mass in the 10% and 25% samples which is related to the polyene group degradation of the PVA as it happens at the same temperature range as neat PVA and the backbone is not expected to change with titanium content.

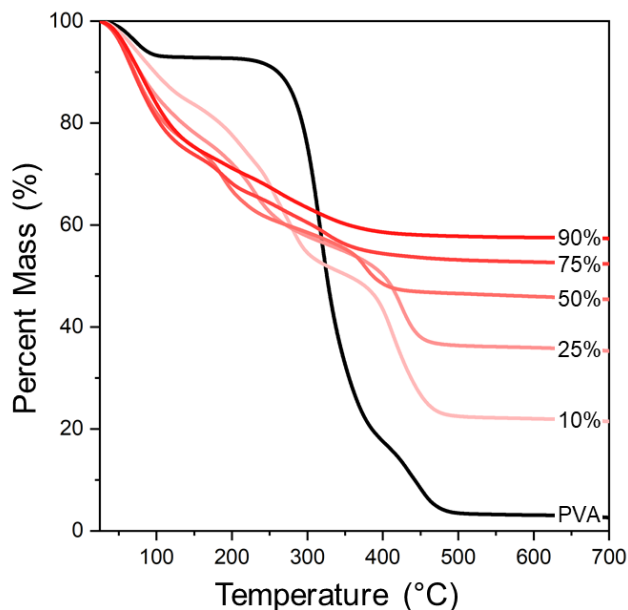


Figure 1.11 TGA of Hybrids Increasing titanium content leads to improved thermal stability. The hybrids show low temperature mass loss due to the incomplete hydrolysis of titanium tetrachloride.

With the gradual decrease in mass at lower temperatures, the hybrids films are post-treated both with annealing and washing steps to elucidate the process occurring. The annealing step is to gain further insight into the refractive index increase. Figure 1.12 shows both 10% and 25% hybrids after annealing at 150 °C for 5 minutes. Higher vol% Ti content films are not post-treated due to them not being great film morphologies. For both 10% and 25% hybrids the mass loss, with the exception of water loss, is limited below 150 °C. This verifies that the removal of chlorine is irreversible, thus the hybrids will behave as the highest, previously annealed samples. For example, a hybrid annealed at 150 °C then 100 °C will have the same properties as the 150 °C annealed only sample. The annealing is only expected to change crosslinking density and not any crystallinity because no crystallization transitions occurred in DSC.

Similar to the annealing post-treatment, hybrids washed in water show further improved thermal stability. Hybrids were submerged in water in 5 minute increments, with the pH of

the water measured after each soak. Once the pH equilibrates to neutral water, the removal of chlorine and further oxidation of titanium is expected to be complete. Washed hybrids have mass-loss onsets even greater than that of annealed hybrids. The refractive index of the hybrids are expected to be even higher than the 150 °C annealed ones, however were not tested in this thesis. Washing steps may not be favorable post-treatments especially in photonics and optics thus annealing is only considered throughout the thesis. Regardless of post-treatments, the high temperature degradation steps, ~400 °C, are unaffected and thus attributed to polyene segments. The first degradation step which is attributed to the hydroxyl group removal also increases slightly with post-treatment which suggest the post-treatments crosslink the network further.

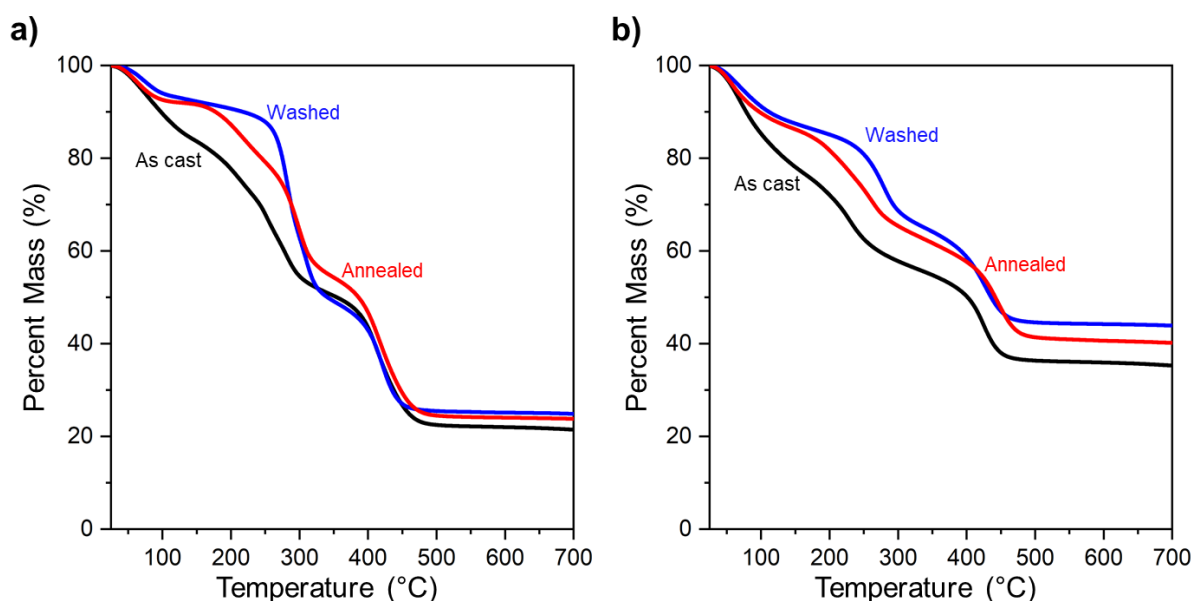


Figure 1.12 TGA of Post-treated Hybrids (a) Mass loss of as-cast, 150 °C anneal, and water washed 10 vol% Ti hybrids (b) Mass loss of as-cast, 150 °C anneal, and water washed 15 vol% Ti hybrids.

The thermal investigations suggest that covalent crosslinking is possible in the hybrids, however, XPS can help gain information to nearest neighbor bonds in the network. XPS spectra are measured at four binding energies of interest that relate to the energies for

carbon, oxygen, chlorine, and titanium as these are the only four atoms expected in the hybrid other than hydrogen which is not accessible in XPS. Figure 1.13 represents the corresponding spectra for each atom at varying vol% Ti hybrids. For neat PVA, three peaks are expected and seen in the XPS spectra which correspond to CH₂ at ~284 eV, C-OH at ~286 eV, and C=O at ~289 eV.⁴⁴ As more titanium is introduced to the hybrid there is a shift in these carbon peaks to higher binding energies. This increase is attributed to an increased local strain due to the crosslinking leading to more cationic behavior of the carbon atoms. Similar shifts in binding energies are seen in crosslinked polyacrylimides.⁴⁵ There is also a decrease in intensities of the ~286 eV peak of the C-OH which suggests that the crosslinking occurs through these groups. Similar decrease in the C-OH signal is seen in crosslinked pullulan nanofibers⁴⁶ and PVA.⁴⁷ There is little change in the C=O intensity indicating that the processing does not significantly hydrolyze the PVA and crosslinking does not occur through the acetyl groups.

XPS spectra of oxygen atoms are split primarily into two different species, O-C at ~532 eV and O-Ti at ~531 eV. There is a broadening and shift of the oxygen spectra towards lower binding energies which is consistent with increasing titanium content in the hybrids. The broadening of the oxygen spectra indicates that there are several species of oxygen which are due to O-C bonds as well as mono- and poly-nuclear titanium species. The binding energies of Ti-O-Ti and Ti-O-C are at very similar binding energies and difficult to deconvolute but are both expected to be present in this hybrid to be consistent with the carbon spectra.⁴⁸ Chlorine spectra show a steady increase in chlorine content with vol% Ti with two peaks appearing that are the *p*-orbital splitting signals in XPS. Finally, titanium spectra show a slight increase in binding energy with vol% Ti in the hybrid with multiple

peaks, separated by about 6 eV, is consistent with the p -orbital splitting of Ti^{IV} .⁴⁸ Overall, the consistent shifts in XPS spectra with titanium content in the hybrids suggests good homogeneity of the hybrid with no vertical phase separation as the XPS is surface sensitive.

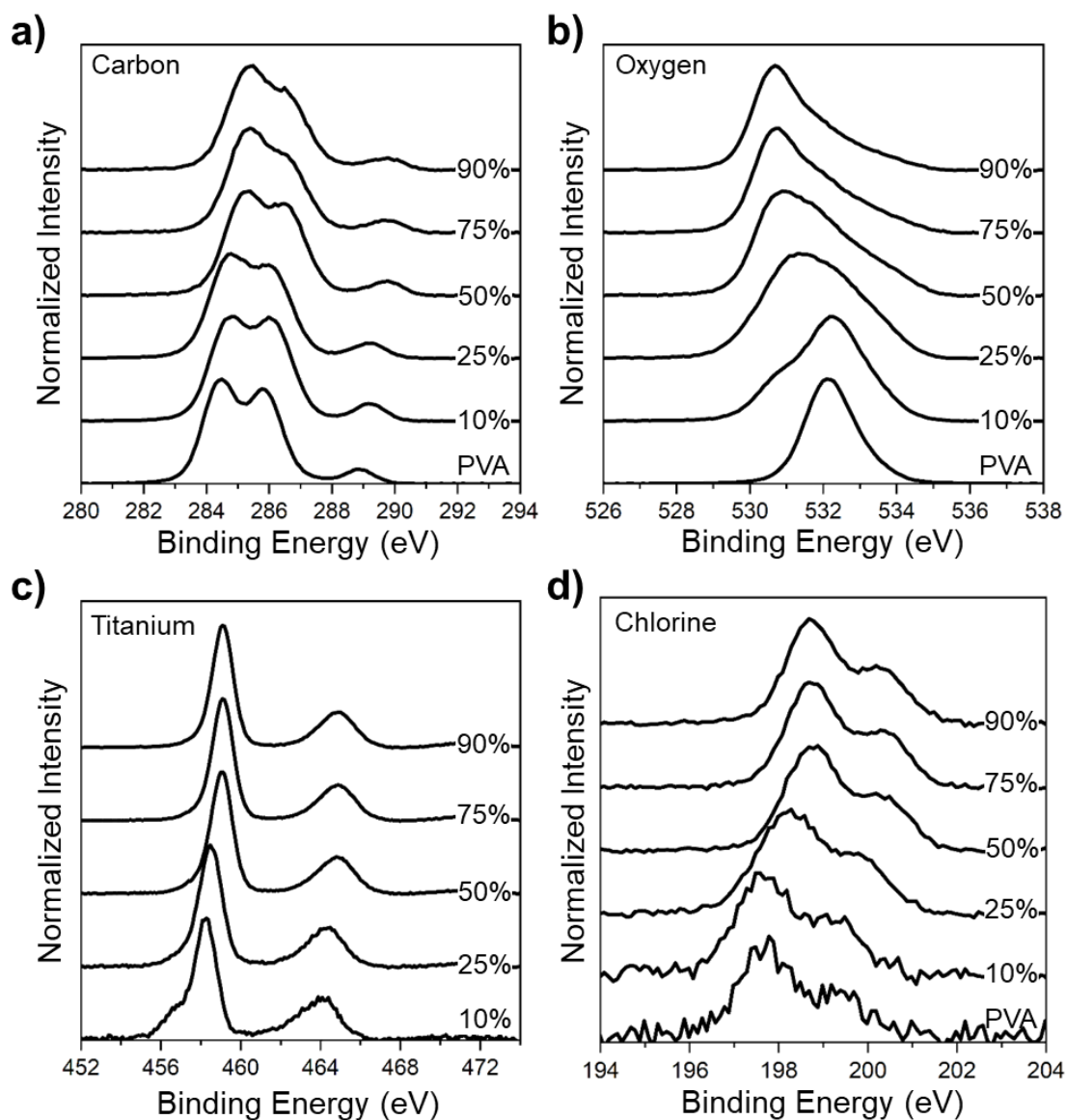


Figure 1.13 XPS of Hybrids (a) Carbon peaks of hybrids show an increase in binding energy with titanium content as well as a decrease in the C-OH peak. (b) Oxygen peaks showing a trend from mostly O-C to O-Ti bonds. (c) Titanium peaks with evidence of the p -orbital splitting. (d) Chlorine peaks with noisy signals indicated there is very little residual chlorine in the hybrids.

In addition to the trends with titanium content in the hybrids, XPS can provide insight into chemical species evolution due to annealing. Figure 1.14 shows the atomic percentages for a 60 vol% Ti hybrid after different annealing temperatures. There is significant mass loss of the hybrids from room temperature to 150 °C seen in TGA. Additionally, the refractive index increases slightly with annealing which suggests new bond formation and polarizations. For the 60 vol% hybrid, there is a decrease in the amount of chloride in the film and a subsequent increase in oxygen. The titanium atoms are hypothesized to oxidize further during this annealing. Oxygen's greater electronegativity compared to chlorine is expected to increase the dipole moment which can affect the polarizability and therefore refractive index. When compared the ratio of titanium to chlorine atomic percentages, this ratio increases from ~2.5:1 to 13:1 in a parabolic-like trend. This parabolic-like trend in Ti-O conversion mirrors the optical thickness changes in the hybrid with annealing temperature. The relation between the two are not expected to be exact since densification of the hybrid occurs during annealing as well which affects refractive index but is not a measurable feature in XPS.

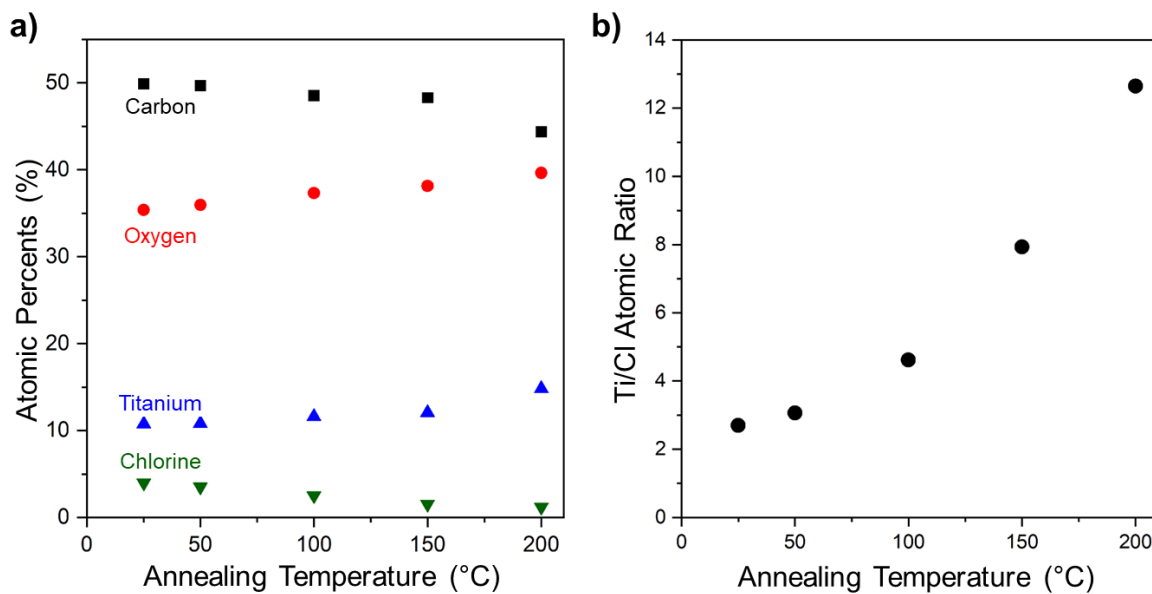


Figure 1.14 Annealing Effects of Hybrid Atomic Ratios (a) Atomic percentages for each element present in the hybrids at various annealing temperatures. (b) Ratio of the amount of titanium to chlorine atoms as a function of annealing temperature. This ratio is the largest change between two atoms and is expected to contribute to the refractive index.

To gain further insight into the XPS spectra of the hybrids, we can look at materials that are known to crosslink PVA and traditional nanocomposites with PVA. Borax (sodium tetraborate) will crosslink PVA, through the boron atom with sodium acting as an ionic stabilizer. In particular, borax has been reported to consume neighboring hydroxyl groups on PVA forming a bidentate-like crosslinking scheme.⁴⁹ Borax hybrids were prepared by dissolution of borax in water and added to a PVA solution and spun-cast. Figure 1.15a shows the carbon spectra of neat PVA with 10, 30, and 50 wt% borax. Most notably, there is a significant drop in the peak assigned to C-OH which are consumed through the crosslinks.

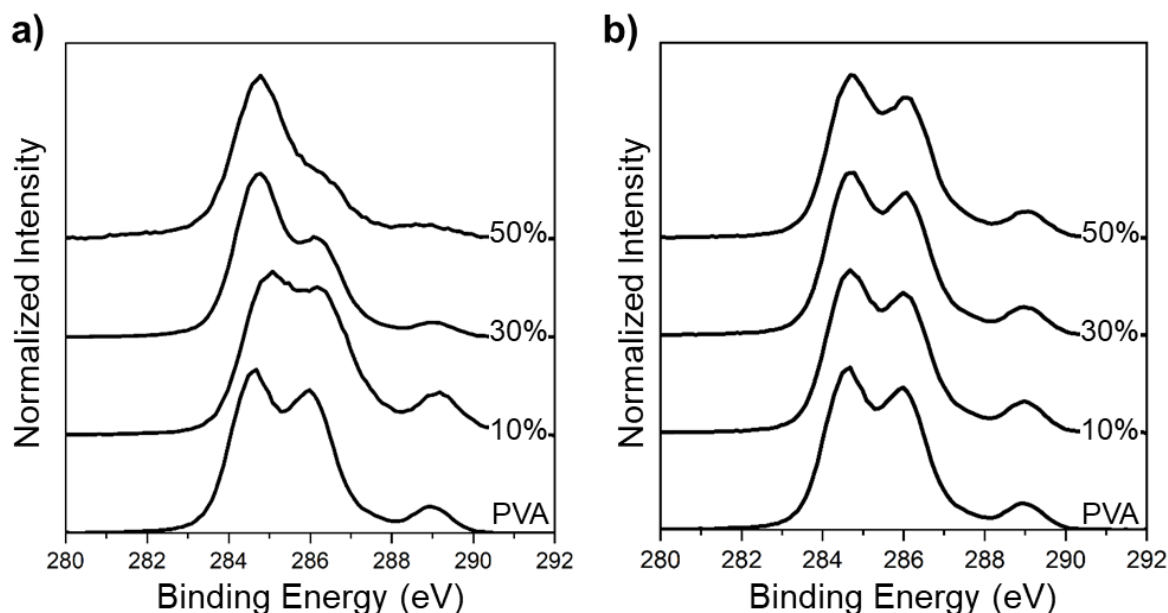


Figure 1.15 Comparing XPS to other Hybrids and Nanocomposites. (a) Carbon XPS peaks of borax-crosslinked PVA. The sharp decrease in the C-OH peaks is consistent with then covalent crosslinking of the hydroxyl groups. (b) Carbon XPS peaks of a traditional TiO₂:PVA nanocomposite where only hydrogen bonding interactions are expected. The consistency in XPS spectra confirm no hydroxyl group chemical interactions.

TiO₂ nanocomposites with PVA are not expected to consume C-OH bonds, and instead will only interact through hydrogen bonding. To produce these nanocomposites, TiO₂ nanoparticles were dispersed in water and adding to a PVA solution and then spun-cast. In Figure 1.15b, the carbon spectra in XPS of neat PVA and 10, 30, and 50 wt% TiO₂:PVA nanocomposites show no change with TiO₂ content. Therefore the nanocomposite does not covalently crosslink PVA, and is contributor to scattering losses in films.¹⁴ The hybrid material's carbon XPS spectra more closely resembles that of the borax crosslinked PVA.

1.3.5 The Case for a Molecular Hybrid

The superior optical properties of the hybrid suggests exceptional mixing of the titanium species and PVA. Without any apparent diffuse scattering, the titanium species are expected to be below 5 nm in diameter, and the homogeneity of the films support no phase

separation. In addition to the optical characterization, thermal and rheological measurements suggest significant crosslinking occurs evidenced by the sharp increases in T_g . XPS measurements suggest the chemical crosslinking of the PVA through the condensation of the titanium species. In particular, the hybrid is expected to form a bidentate crosslinking scheme, like that of Borax-crosslinked PVA. The stability of the bidentate form of the titanium species is consistent with that titanium hydrolysis solutions.⁵⁰

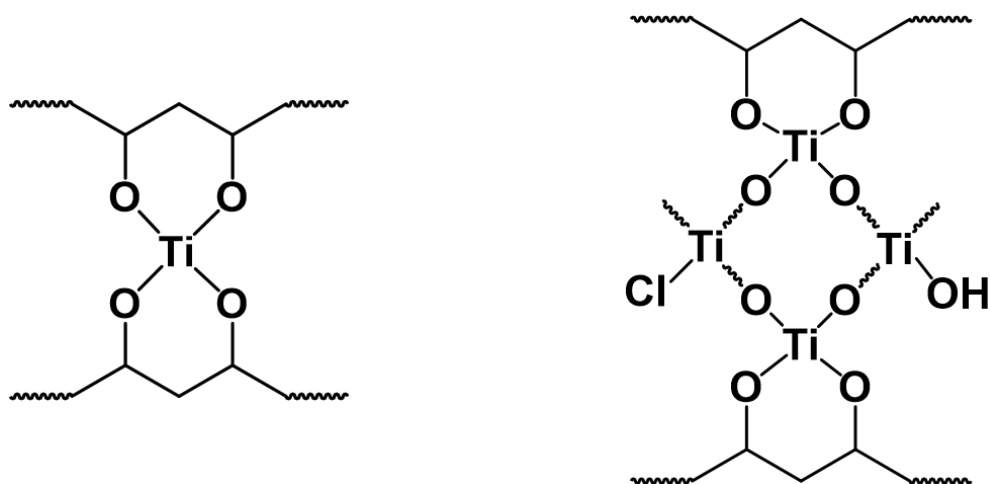


Figure 1.16 Proposed Titanium Oxide Hydrate:PVA Molecular Hybrid Structure.

Thus, this formation is deemed a molecular hybrid, as it best explains the thermal, rheological, and spectroscopic measurements. This molecular hybrid, to the best of our knowledge, exhibits superior optical properties compared to that of other polymer-based hybrids. The exact structure is still unknown, however there is an expected population of crosslinking chemistries that are dependent on vol% Ti and post-processing conditions. Figure 1.16 highlights the existence of mono-nuclear (1 titanium atom per crosslink) and polynuclear (multiple Ti atoms per crosslink), which have been identified by the photochromic responses of the hybrid, discussed in Section 1.5. This molecular hybrid is

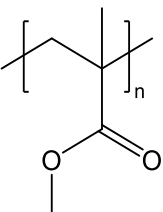
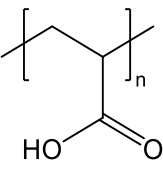
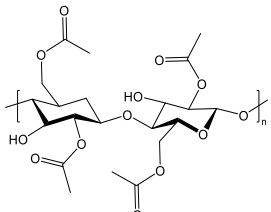
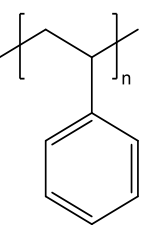
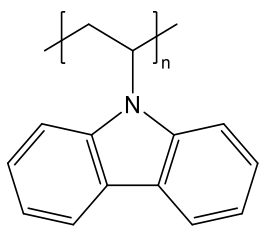
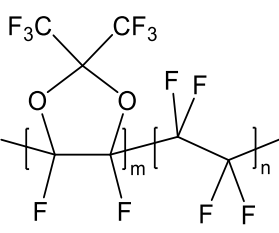
thus a great candidate for several photonic applications, including distributed Bragg Reflectors.

1.4 1D Photonics: Distributed Bragg Reflectors

1.4.1 Introduction

Optical polymers have favorable properties that make them great candidates for photonics. Their absorption occurs in the UV region and with their amorphous structure cause limited optical losses in the visible and near-IR regions. Additionally, they are mechanically flexible and robust, light-weight, and their potential-wide area production makes processing accessible over several substrate geometries.⁵¹ One of the most important parameters is the refractive index of the polymer. Examples of commodity polymers used in photonics are poly(methyl methacrylate) ($n = 1.49$),⁵² cellulose acetate ($n=1.46$),⁵³ poly(acrylic acid) ($n=1.45$),⁵⁴ polystyrene ($n=1.59$)⁵⁵ and poly(N-vinylcarbazole) ($n=1.68$).⁵⁶ Common polymers used in photonics can be found in Table 1.2 along with their refractive index and T_g .

Table 1.2 Commodity Polymers

| Polymer | Structure | Refractive Index, n | T_g (°C) |
|--|---|-----------------------|-------------------|
| poly(methyl methacrylate) |  | 1.49 | 125 ⁵⁷ |
| poly(acrylic acid) |  | 1.45 | 102 ⁵⁸ |
| cellulose acetate |  | 1.46 | 187 ⁵⁹ |
| Polystyrene |  | 1.59 | 100 ⁶⁰ |
| poly(n-vinylcarbazole) |  | 1.68 | 225 ⁶¹ |
| Poly[2,2-bis(trifluoromethyl)-4,5-difluoro-1,3-dioxole-co-tetrafluoroethylene] |  | 1.30 | 240 ⁶² |

One of the most common and simplest photonic structures is a one-dimensional photonic crystal. Photonic crystals have been studied for decades, following the work of Yablonovitch⁶³ and John.⁶⁴ These are multilayer stacks of alternating materials with a refractive index contrast which can create anti-reflection coatings (ARCs) and distributed Bragg reflectors (DBRs). Polymer-based DBRs are generally produced via solution-processing, melt-processing, and self-assembly of block-co-polymers, each having their advantages and disadvantages. Solution processed DBRs are examples of a layer-by-layer production and the thickness of the individual layers is manipulated with process parameters. However, orthogonal solvents must be used for each layer so that there is reduced interdiffusion of layers. Coextrusion techniques heat the polymers above their glass transitions so the polymers flow and can coat large areas. However, polymers that are not insoluble with each other must be used also to not cause layer interdiffusion. Block-copolymers will self-assemble into lamellae when volume fractions of each segment is around 50%.⁶⁵ However, to achieve features in the visible range, layers must be on the order of 100 nm which requires ultra-high molecular weights.

An important parameter of the DBR is the optical thickness of each layer, which is the quarter-wave thickness. In this case, from the TMM, a phase change traversing of quarter-wave layer is $\pi/2$. Thus Equation 1.14 collapses to:

$$M_j = \begin{bmatrix} \cos \delta_j & (i \sin \delta_j)/n_j \\ in_j & \cos \delta_j \end{bmatrix} = \begin{bmatrix} 0 & i/n_j \\ in_j & 0 \end{bmatrix} \quad (1.20)$$

If this quarter-wave layer is paired with another quarter-wave layer of a different refractive index, this constitutes a bilayer in DBRs. Then if the bilayer is repeated N times, the characteristic matrix takes the form:

$$\begin{bmatrix} (n_L/n_H)^N & 0 \\ 0 & (n_H/n_L)^N \end{bmatrix} \quad (1.21)$$

where n_L and n_H are the lower refractive index and higher refractive index, respectively. Combining this characteristic matrix along with Equations 1.13 and 1.15, we can solve for reflection intensity for a DBR¹⁶:

$$R(\lambda_0) = \left(\frac{1 - (1/n_s)(n_H/n_L)^{2N}}{1 + (1/n_s)(n_H/n_L)^{2N}} \right)^2 \quad (1.22)$$

As seen from the equation, the reflectance is dependent on the contrast of the refractive indices, with a larger difference leading to stronger reflections. Due to the traditionally small refractive index contrast of polymers, high reflectance is generally achieved with an increased number of layers. Additionally, the width (Δ) of the stopband of the DBR increases with refractive index contrast, accordance with¹⁶:

$$\Delta\left(\frac{\lambda_0}{\lambda}\right) = \frac{1}{\pi} \sin^{-1} \left(\frac{n_H - n_L}{n_H + n_L} \right) \quad (1.23)$$

A general schematic of a DBR along with model spectra dependences on number of layers and refractive index contrast are shown in Figure 1.17. The area of reduced transmission is referred to as the stopband of the DBR, and is the same area that experiences the high reflection.

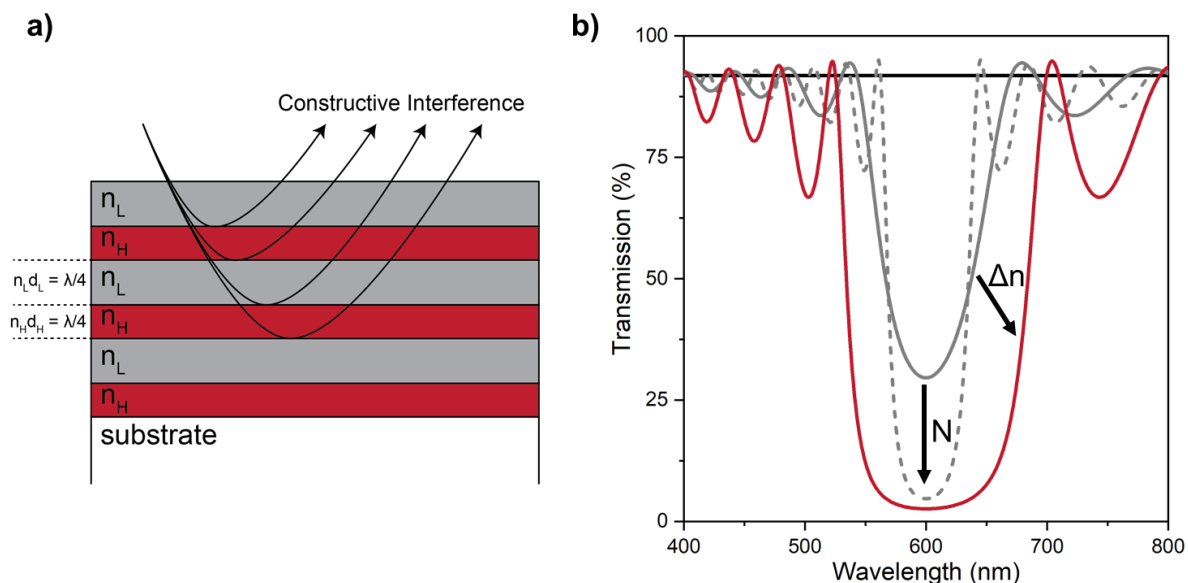


Figure 1.17 DBR Schematic and Transmission. (a) DBR schematic highlighting the bilayer periodic structure with each layer having a quarter-wave optical thickness which creates constructive interference upon reflection. (b) Modeled transmission spectra of DBRs. An increase in the number of layers, N , or a larger refractive index contrast, Δn , lead to stronger stopbands.

To design efficient polymer-based DBRs, a large refractive index contrast is desirable as it creates a much stronger stopband for the same number of layers (Figure 1.17b). DBRs with strong reflection bands create what is known as structural color and DBRs are often observed in nature, seen in butterflies,⁶⁶ beetles,⁶⁷ and plants.⁶⁸ These naturally occurring photonic crystals provide insight to manufactured DBRs and potential applications, including light manipulation for power conversion, heat-management, and colorimetric sensing.

1.4.2 TiOH:PVA Hybrids in DBRs

As mentioned earlier, the DBR stopband or photonic bandgap intensity increases linearly with the dielectric contrast and exponentially with the number of periods composing the structure until unitary reflectance.⁶⁹ Thus strategies to improve refractive index contrast include the introduction of inorganic materials into the polymer matrix thus tailoring of the

refractive index for the bulk material. Using the TiOH:PVA hybrid investigated in this thesis allows for solution processed DBRs with high contrast and tunability. Its high refractive index allows for stronger reflections bands compared with that of other polymers like polystyrene and poly(methyl methacrylate). Figure 1.18 shows the modeled reflection bands for DBRs comprised of bilayers of polystyrene and PMMA compared to that of a 60 vol% Ti hybrid and PMMA.

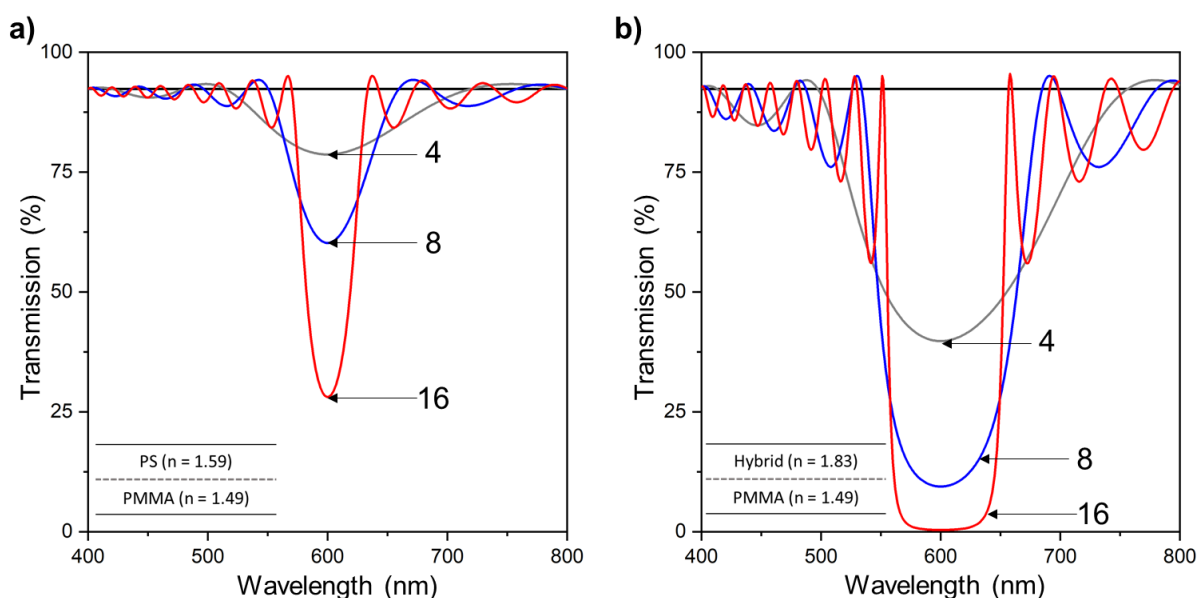


Figure 1.18 Commodity Plastic-based DBRs versus Hybrid-based DBRs. (a) Modeled transmission spectra of 4, 8, and 16 bilayer PS and PMMA DBRs. (b) Modeled transmission spectra of 4, 8, and 16 bilayer hybrid and PMMA DBRs. The hybrid-based DBRs can reflected 99% of light with only 16 bilayers while the PS:PMMA system only reaches ~70% for the same number of bilayers. Additionally the hybrid based DBRs show stopbands twice as wide.

In addition to the stopband reaching less than 1% transmission in 16 bilayers, the width is roughly 100 nm wide compared to the ~50 nm wide stopband of PS and PMMA. For several applications, wider stopbands are desirable, however, the advantage of the hybrid over any other neat material, is its tunable refractive index. If narrow stopbands are desired, the same starting materials can be used with just altering the concentration of titanium in

the hybrid. For the remainder of this thesis, DBRs are produced with hybrids as the high index layer and PMMA as the low index layer. PMMA is chosen as the low index layer for its good thermal stability, insolubility in water, and relatively low cost.

1.4.3 Solution Processed DBRs

Solution-processing is generally cheaper than vapor deposition techniques due to lower equipment costs and continuous high-throughput potential. When producing DBRs, interfacial affects can play a large role in the periodicity of the stopband, thus solution-processed DBRs call for certain considerations like solubility and repeatability. In regards to solubility, as DBRs are comprised of bilayers in a layer-by-layer technique, each layer must not be soluble in the next layer's solvent. This is known as using orthogonal solvents. Full dissolution of polymers in solvents can generally take several minutes to hours especially at room temperature. However, even just partial dissolution can cause poor interfaces between layers so it must be considered.

The hybrid, owing to its heavily crosslinked network, is insoluble in all solvents, which vastly increases the potential workspace. However, when the hybrid is soaked in water, some small chemical changes are seen through the removal of chlorine. Even though the hybrid with not fully dissolve, using water may alter the hybrid's optical thickness too greatly. For the low index layer, PMMA is chosen because it is insoluble in water. Additionally, it is soluble in several organic solvents, including toluene. Toluene is chosen as the solvent because of its relatively low vapor pressure compared to acetone, so loss of solvent due to evaporation will be limited.

The next consideration to solution-processed DBRs is the repeatability of layer thicknesses. As DBR stopbands have quarter-wave dependence, shifts of 5% in thickness can result in

20% shifts in stopband wavelengths.⁷⁰ Dip-coating is chosen as the deposition method over spin-coating due to its limited edge effects, highly controllable deposition rate, and dual layer deposition. Spin-coating can lead to large edge effects during deposition which decreases the effective area of the DBR and the layer thickness repeatability is poor.⁷¹ The dip-coater has a controllable rate with precision reaching 0.01 mm/min, which is highly advantageous for repeatability. There is also no significant acceleration during dip-coating given the slower rates. Finally, dip-coating submerges the glass slide in the solution, then, upon retrieval, produces a layer on each side, which effectively cuts the time in half to produce similar structures through blade-coating. However blade-coating has been beneficial in large area production of solution processed DBRs.⁷²

Dip coating is also used widely in industry and capable of depositing excellent quality films. However, a main disadvantage is due to the large solution volume needed to submerge the substrates, hence the need to low-cost materials like the hybrid and PMMA. Figure 1.19 shows a general schematic of dip-coating along with regimes that dictate the thickness of the resulting films: capillary, intermediate/viscous, and drainage.

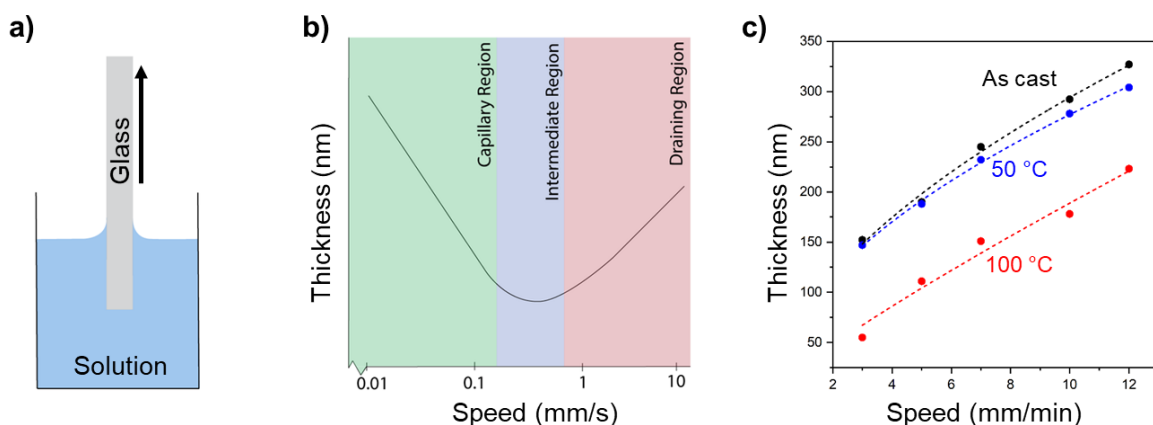


Figure 1.19 Setup and Calibration of Dip-coated Layers. (a) General schematic of how a substrate is dipped into solution. (b) General regimes of dip-coating along with their relative relations of thickness to speed. (c) Calibration curves for 60 vol% hybrids dip-

coated at several rates and annealed. Significant densification occurs upon annealing and thus must be considered. (Credits for A and B: Ossila⁷³)

The thickness of the film is directly related to withdrawal speed and the regimes experienced in the hybrid systems and PMMA are somewhere in the viscous and drainage regimes. This regime has a meniscus drawn from the solution, which increases with increasing speed.⁷⁴ There are several other factors that affect film thickness like surface tension and viscosity, however all other variables are kept constant to eliminate these effects. The resulting correlation between thickness and speed is assumed to be a power law.

The hybrid material contracts upon annealing, thus separate calibration curves are required to predict dip-coating speed to reach a particular quarter-wave thickness. Annealing hybrids at 50 °C causes about a 10% contraction, and 100 °C annealing contracts the hybrid by about 50%. In addition to the physical thickness contraction, the annealing effects on refractive index of the hybrid must be considered. The produced calibration curve and model fit provides information for dip-coating speeds needed for a variety of DBRs with stopbands across a wide range.

1.4.4 DBR Applications

The tunability of a hybrid-based DBR with regards to the stopband leads to applications both during and post-processing of photovoltaics that have a wide spectral absorption. Due to the spectral broadness, time-varying incident angle, and directional/diffusive nature of solar radiation, various strategies have been developed to enhance the power-conversion efficiency of PV cells. Polymer DBRs offer new strategies to improve photon collection in both inorganic and organic-based PVs.⁷⁵ Often one uses inorganic DBRs made of alternated layers of MoO₃ and LiF fabricated by thermal evaporation that are implemented

into bulk-heterojunction photovoltaic cells to achieve semitransparent devices with enhanced efficiency, but with new organic photovoltaics reaching higher efficiencies and maintaining mechanical robustness, polymers show promise for improving device performance. Device architectures include a DBR inserted in the back of the cell to reflect transmitted light back into the device allowing such photons a second chance to interact with the semiconductor. Enhanced spectral absorption increases the device fill factor, while retaining the transparency of the base cell.^{76,77} The implementation of blade-coated DBR from commercial inks as back reflectors in transparent perovskite photovoltaic devices provided for instance a significant increase of the short-circuit current with limited effects on the open-circuit voltage, thus enhancing the power conversion efficiency of about 20%.⁷⁸ DBRs integrated as a scaffold into the active layer of a perovskite photovoltaic device have been shown to exhibit high reflectance bands that also direct the non-reflected light into the active layer resulting in high photovoltaic conversion.⁷⁹

Light and energy management of greenhouses can be improved through implementation of semi-transparent organic solar cells. Lighting demands will depend on the crop of interest and geographic location. Luckily, there are several absorption bands accessible using organic photovoltaics, and lettuce has been shown to grow well under semi-transparent solar cells due to its shade-tolerance.⁸⁰ The active layer of the semi-transparent solar cell is thus chosen to utilize the absorption bands not predominantly used by the chlorophyll. Ultimately, the active layer is composed of FTAZ:IEICO-4F:PC₇₁BM, which absorbs strongly in the 500-600 nm and near-IR range.

To enhance energy production, the semi-transparent solar cells were paired with back-reflecting DBRs that manage light in the visible and near-IR spectra in the ranges not

efficiently used by the plants. Both of these DBRs are shown in Figure 1.20 and comprised of 60 vol% Ti hybrids annealed at 150 °C paired with PMMA with 8.5 bilayers deposited on both sides of the glass substrate.

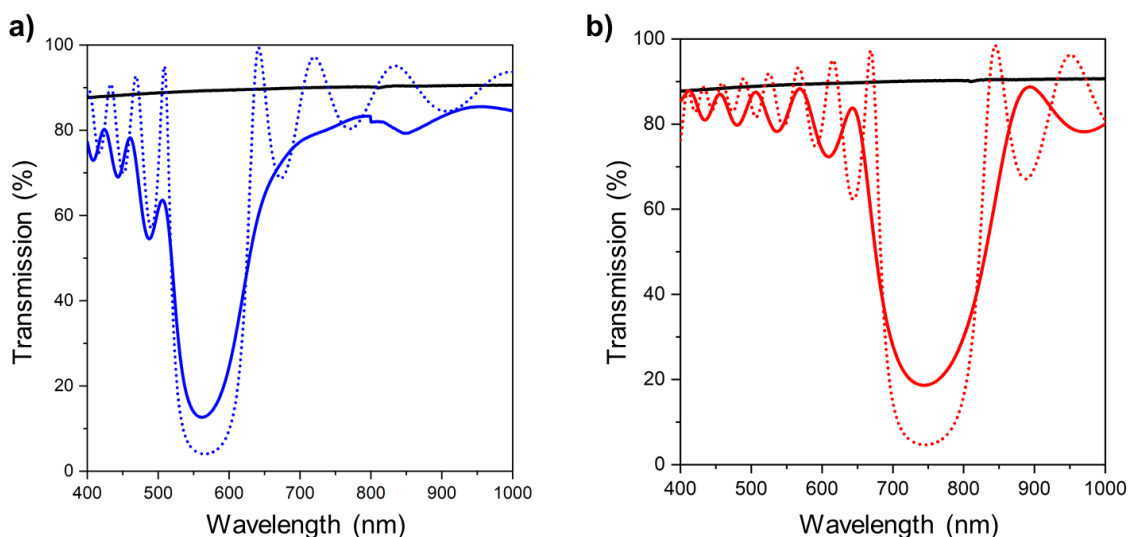


Figure 1.20 Visible and Near-IR Hybrid-based DBRs. Visible and near-IR transmission spectra of 8.5 bilayer DBRs fabricated with titanium oxide hydrate:poly(vinyl alcohol) hybrid and PMMA, glass baseline reference is also shown (black line). (a) DBR-A has a stopband centered at 560 nm with 87% rejection of light in good agreement with TMM calculations (dotted line). (b) DBR-B has a stopband centered at 745 nm with 81% rejection of light which is somewhat lower than the TMM model predicts (dotted line).

Both DBR-A and DBR-B are modeled using the home-built TMM code with the hybrid having a refractive index $n = 1.75 + 0.029/\lambda^2$ and the PMMA refractive index is $n = 1.48 + 0.005/\lambda^2$. The model spectra found a best fit for hybrid thickness to be 63 nm and 98 nm for DBR-A and DBR-B, respectively. The PMMA thickness is 113 nm and 132 nm for DBR-A and DBR-B, respectively. Relatively good agreement between the transmission spectra and modeled fit is found for each DBR. Deviations from the model to the actual spectra can be caused by scattering instances like air bubbles during deposition. Small scattering points will decrease the stopband intensity and flatten the strong periodic oscillations outside of the stopband. Additionally, layer thicknesses are likely to vary

slightly which will also interrupt the phase coherence slightly, however this is limited. Layer interfaces and surface roughness can also play a role but are not expected in this case due to near perfect interfaces capable with the hybrid.^{28,33}

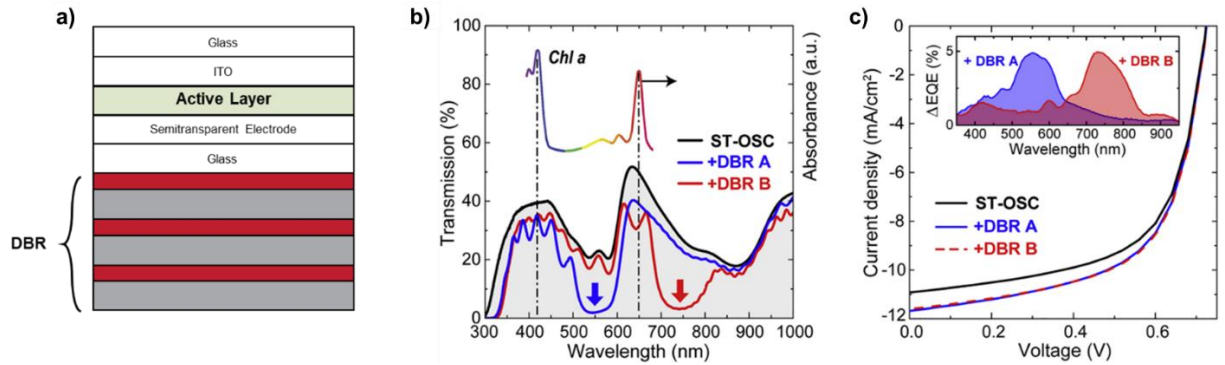


Figure 1.21 Back-reflecting DBRs for Semi-transparent Solar Cells. (a) General schematic of the semi-transparent solar cell with back-reflecting DBR. Light is assumed to enter from top-side. (b) Transmission curves of semi-transparent solar cell on its own and with DBR-A and DBR-B. Chlorophyll a absorption bands in inset. (c) Current density vs voltage curves of the semi-transparent solar cell on its own, and with DBR-A and DBR-B. External quantum efficiencies of solar cell with DBR-A and DBR-B in inset.

The general schematic for a back-reflecting DBR for a semi-transparent solar cell is shown in Figure 1.21 which also shows the transmission curves of the whole system. With addition of the DBRs, the area of the stopband is reduced to less than 5% transmission. Figure 1.21 also shows how the DBR's do not significantly affect the strong chlorophyll absorption bands at ~410 and 650 nm. The addition of the DBRs increases the reflection to the active layer leading to a 5 and 6% increase in the short-circuit current density with DBR-A and DBR-B, respectively. There is also a significant increase in the external quantum efficiency in the stopbands for each DBR. The semi-transparent solar cell has a power conversion efficiency of 4.9%, and addition of the DBRs leads to an increase to 5.16% and 5.19% for DBR-A and DBR-B, respectively. Each DBR shows a system improvement of over 5%. These semi-transparent cells have lower efficiencies than their

opaque counterparts however when considered in the greenhouse, the plant growth in this system is shown to not be significantly affected by the filters making them more versatile than the opaque options.⁸¹

In addition to back-reflecting visible light, DBRs can be used to manipulate the near-IR light to photonically cool PV cells. Crystalline silicon PV modules increase in temperature by 20-30 °C during operation in sunny conditions,⁸² and the module loses efficiency at a rate of 0.4 %/°C due to a decrease in open-circuit voltage.⁸³ The heat is produced by thermalization of carriers to the band edge, carrier recombination, ohmic loss, and parasitic sub-bandgap absorption.⁸³ Several methods to improve device efficiency have been implemented including heat pipe passive cooling, active cooling by water flow, and liquid immersion techniques.⁸⁴ Passive and active cooling techniques are limited due to heat transfer areas and the requirement for large power generation modules, respectively.⁸⁴ Since heat is largely a direct consequence of near-infrared (NIR) and infrared radiation (IR) incident on the cells, an alternative approach is the deployment of highly reflective coatings for the NIR/IR range of solar radiation. A DBR in the near-IR is calculated to decrease the temperature of a silicon-based solar panel by over 5.7 °C.⁸⁵ This photonic cooler can also be used in a concentrated photovoltaic system to significantly reduce the solar cell temperature or required cooling power.

In the case of greenhouses, a near-IR DBR can help manage the energy demand from temperature regulation. As the near-IR wavelengths account for ~50% of the total solar energy (Fig 1.23), a DBR reflecting a significant portion of this range can affect the thermal load. A modeled DBR spectra using the same vol% Ti hybrid and PMMA layers is designed to reject the range of 800 nm to 1600 nm. This near-IR DBR reduces the number

of hours in a year that the temperature in the greenhouse cannot be maintained below the setpoint of 82 °C to grow tomatoes from 280 h to 82 h. This also improves the power generation of the greenhouse by 10%.⁸¹

Thermal energy management via DBRs is a highly sought after passive cooling technique for buildings as well. These are DBRs that selectively reflect thermalizing near-IR light and dangerous UV-light while maintaining visible transparency (Figure 1.22). These so-called ‘heat mirrors’ have already been realized commercially but require thousands of coextruded layers. Hybrid-based DBRs have the potential to reduce the overall number of layers to below 100. The drastic decrease in the number of layers, while maintaining the same near-IR rejection, leads to an overall thinner DBR which means fewer starting materials and lower weight and potentially lower production cost.



Figure 1.22 Heat Mirror Schematic for Passive Cooling DBRs can be designed to reflected near-IR radiation from the sun as well as UV-irradiation while maintaining visible transparency, thus reducing energy costs to cool via air-conditioning.

Traditional periodic structures of the DBR do not create a significant enough stopband width in the near-IR range. Instead of trying to increase the refractive index contrast of the bilayers, the stopband width can be increased by designing a ‘chirped’ DBR. A chirped DBR has an optical thickness that changes in a gradient-like manner throughout the stack which causes a wide stopband across the quarter-wavelengths covered. Thus a semi-infinite stopband can be generated with any pair of non-absorbing polymers. Chirped structures, or even ‘chaotic stacks’ – photonic structure of random optical thickness – are seen in nature, most notably in the beetles. The beetle’s cuticle possesses this chirped structure resulting in a stopband ranging from 500 nm to 800 nm and appearing gold.⁶⁷

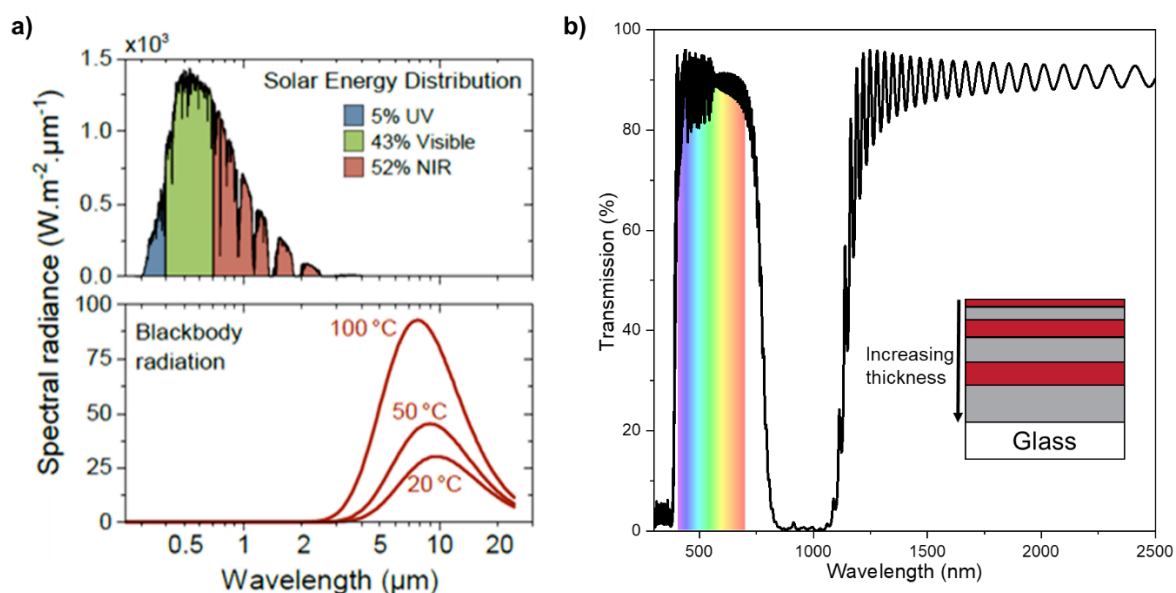


Figure 1.23 Modeling heat-mirrors for maximum near-IR rejection (a) Solar energy distribution across UV, visible, and near-IR wavelengths and black-body radiation from 20 to 100 °C irradiators. Heat-mirrors are more apt at rejecting near-IR light from solar irradiation and not the mid-IR irradiation from room-temperature objects. (b) Modeled chirped DBR from 100 bilayers of 60 vol% Ti hybrid and PMMA to reject 99% of near-IR light from 800-1100 nm. Inset shows chirped DBR schematic.

A schematic of the chirped DBR is shown in the inset of Figure 1.23b. The gradient can be linear, but also could be designed to increase with the change in refractive index at any

given wavelength which would be the most efficient reflectors. Chirped DBRs, given their range of thicknesses, are not any more difficult to solution-process than the periodic structures as dip-coating speeds can easily be varied between layers. Additionally, defects in thicknesses will not affect the overall stopband as significantly. A 100 bilayer chirped modeled DBR transmission spectra is modeled in Figure 1.23b with 60 vol% Ti hybrids annealed at 150 °C and PMMA. Over 99% rejection of the 800-1100 nm range is rejected, along with the range below 400 nm. This additional reflection in the UV-range is due to the wavelengths being a multiple or factor of the quarter-wave thickness. This occurs in any DBR structure and is unavoidable but can be advantageously utilized in heat mirrors. For example, a stopband at 800 nm will also occur at 200 nm and 3200 nm provided there is no refractive index dispersion of the refractive index as dispersions will cause these to shift.

The chirped DBR shows no significant visible light reflections, thus will appear transparent to the eye. The DBR stopband could be shifted to lower wavelength to cover the 700-800 nm range, however the stopband is dependent on incident angle. A higher incident angle from normal will blue shift the stopband, therefore, when considering heat mirrors, the stopband should not significantly shift into the visible range. In general, a 100 nm blue shift is seen in these hybrid-based DBRs. Given the sun's varying angle with respect to time of day, it makes the most sense to design the mirror to account for this, hence the stopband starting at 800 nm.

To assess the potential for DBRs as energy saving heat mirrors, values that calculate the solar and visible spectral responses of a window equipped with such a DBR. These spectral

responses (Eq. 1.24-1.26) are input into an energy consumption software like Energy PlusTM. With known window spectral data, the following values can be calculated⁸⁶:

$$P_s = \frac{\int P(\lambda)E_s(\lambda)d\lambda}{\int E_s(\lambda)d\lambda} \quad (1.24)$$

$$P_v = \frac{\int P(\lambda)E_s(\lambda)V(\lambda)d\lambda}{\int E_s(\lambda)V(\lambda)d\lambda} \quad (1.25)$$

$$P_{hemispherical} = 2 \int_0^{\pi/2} P(\Phi) \cos(\Phi) \sin(\Phi) d\Phi \quad (1.26)$$

Where $P(\lambda)$ is the heat mirror and window's coupled wavelength dependent spectral response, E_s is the solar spectral irradiance function, V is the photopic response function of the eye, Φ is the incidence angle of the light, P_s is the solar spectral value for transmission and reflection, P_v is the visible spectral value for transmission and reflection, and $P_{hemispherical}$ is the angle dependent value for transmission and reflection. The preceding values are all calculated for a heat mirror placed upon a 9750 6 mm EnergyTech SuperGreen Window which has a response shown in Figure 1.24, which also shows the transmission and reflection responses of this window with and without a 100.5 bilayer chirped DBR. The DBR uses a 60 vol% Ti, 150 °C annealed hybrid and PMMA.

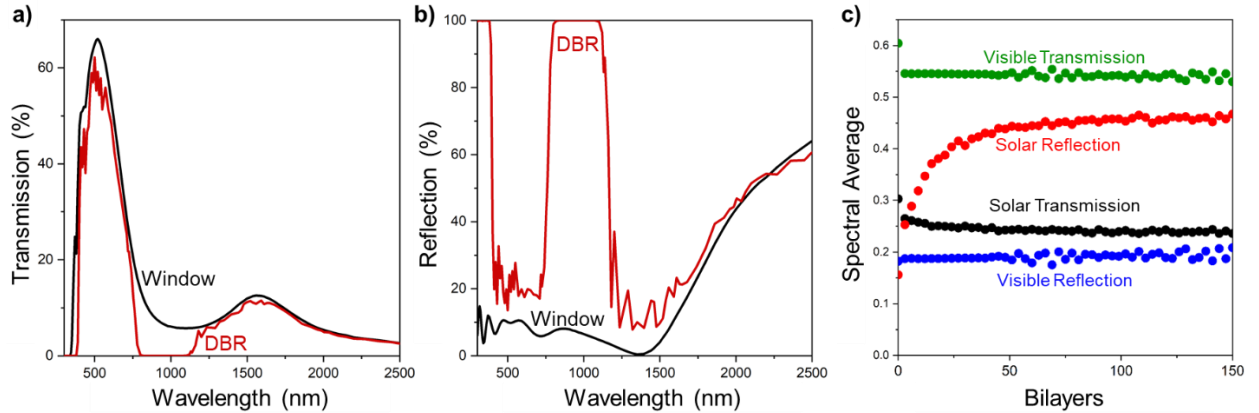


Figure 1.24 Spectral Transmission and Reflection of DBR-coated windows. (a) Transmission curves of EnergyTech SuperGreen window with and without DBR coating. (b) Reflection curves of EnergyTech Supergreen window with and without DBR coating. (c) Spectral values for DBR coated window as a function of bilayers in DBR. Solar reflection value levels off after 50 bilayers.

The window has a unique transmission and reflection spectra, which is unlike glass substrates used earlier. There is only a peak transmission of ~65% in the visible range, however, the curvature matches the eye's photopic response well so the window appears as slightly tinted and not colored. Additionally it has a large reflection band in the mid-IR range from 1500-2500 nm due to a low-emissivity coating, which is advantageous as the DBRs cannot reflect this range without affect the visible range as well. A 100.5 bilayer film shows a complete stopband in the transmission with less than 1% transmission across 800-1100 nm. There is also a small decrease in the transmission in the visible range, however without a significant wavelength dependence to this drop, not structural color is expected. The reflection of the DBR-paired window shows the greatly increased near-IR reflection compared to the window alone.

Calculations of all the spectral responses (Eq 1.24-1.26) as functions of the number of bilayers in the DBR provide insight to design principles. For the solar transmission, visible transmission, and visible reflection there is no dependence of the number of bilayers of the

DBR. However, the solar reflection value changes significantly from 0.15 to 0.45. Additionally, the dependence of the number of bilayers shows that around 50 bilayers, there is a diminishing return to the improved solar reflection beyond this point. This is due to the dependence of the reflection value of a DBR seen in Eq 1.22. For process design, this dependence is highly useful to create the best performing mirror with the fewest number of layers. However, this solar spectral reflection value is only a single value over a large wavelength range, so the actual heat rejection may be underestimated. The hemispherical values are relatively unaffected with addition of a heat mirror, which speaks to the limited dependence of the stopband as functions of incidence angles for chirped DBRs. Additionally, window area to building area will greatly affect the passive cooling capabilities but these calculations are outside of the scope of this thesis. A home-built MATLAB code will quickly calculate these spectral values for any custom heat mirror design for any future work.

Modeling DBRs can assist in energy calculations for buildings, however actual production of these DBRs are limited. As a proof of concept as the hybrid two sets of heat mirrors are produced and their spectra shown in Figure 1.25.

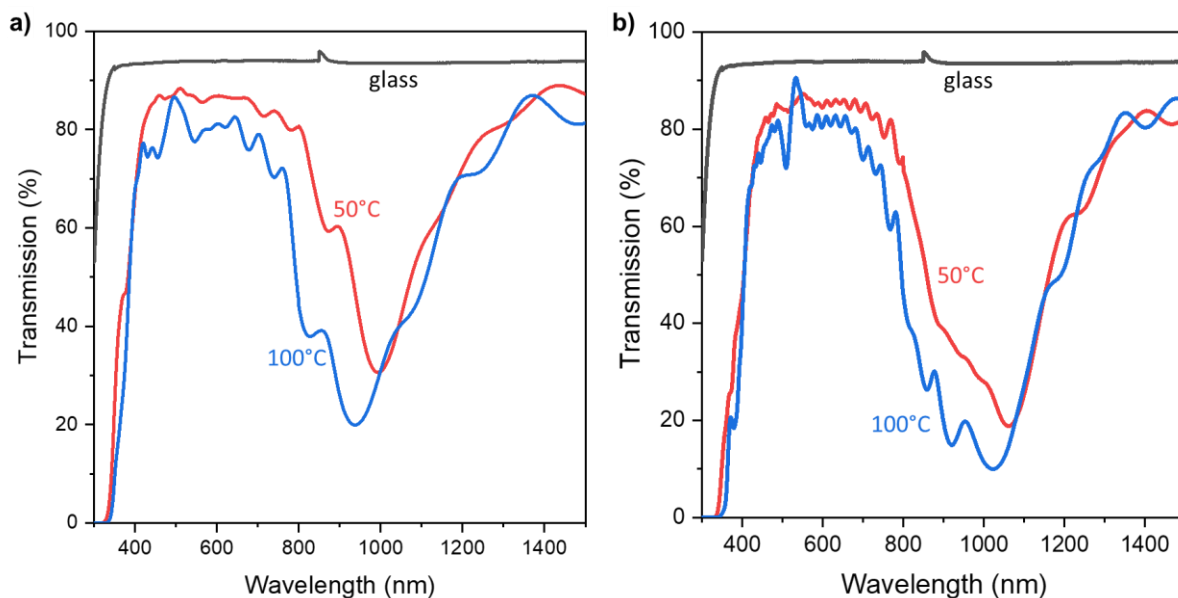


Figure 1.25 Produced Heat Mirrors (a) 8.5 bilayer chirped DBR annealed at 50 and 100 °C (b) 16.5 bilayer chirped DBR annealed at 50 and 100 °C. Each DBR exhibits a wide stopband due to its chirped design, and the increase in stopband strength and blue shift with annealing highlights the densification and refractive index increase of the hybrid.

For both the 8.5 bilayer and 16.5 bilayer DBRs show transmission stopbands with less than 30% transmission. Annealing the hybrids leads to the contraction of the layers, thus shifting the DBR stopband to lower wavelengths which is why the 100 °C annealed hybrids have blue-shifted spectra. The annealing also increases the refractive index of the hybrid without affecting the PMMA which increases the contrast between the two, leading to deeper stopbands. Worth noting is the transmission outside of the stopband range, which the 100 °C annealed hybrid has a lower baseline than the 50 °C. This is likely due to interfacial issues due to different thermal expansions of the PMMA and hybrid, especially since the glass transition of PMMA is around 120 °C. Slower ramp up speeds for annealing can help limit the cracking, and annealing between each layer may limit the effects. Ultimately, the hybrid produces a strong DBR stopband for chirped mirrors with only 33 total layers.

In addition to static light reflection, dynamic applications of polymer-based DBRs are growing exponentially and have shown great potential.⁸⁷ Sensing requires specificity, sensitivity, reversibility, and rapid responses which is achievable with polymer DBRs because an optical parameter change in the layers occurs when the polymer is exposed to the stimuli, thus resulting in a stopband shift. Because of the quarter-wavelength dependence of the stopband, shifts in optical thickness cause a quadrupling of that response. Thus, small changes in the layers, will cause large shifts for the DBR. Colorimetric vapor sensors are widely studied because the swelling of a polymer increases the physical thickness and the swollen polymer depends on the refractive index of the solvent and the relative selectivity of the solvent for each type of layer.^{88–90} Relative humidity (RH) sensing schemes are mostly based on intrinsic swelling behavior of hydrogel-forming polymers. Polyacrylamide (PAAm) and poly(2-hydroxyethyl methacrylate) (PHEMA), have been introduced into DBRs and their RH-responsive behaviors have been studied because of their hygroscopic behavior.^{91–93} Other potential sensors include thermochromic sensing, where the DBR stopband shifts due to a change in temperature. Thermal annealing of many polymeric thin films leads to densification, thus the optical thickness typically blue-shifts. A hybrid material comprised of titanium oxide hydrates and poly(vinyl alcohol) shows a stopband shift of over 100 nm when annealed to 130 °C.²⁸ These densification processes can be non-reversible, thus limiting the lifetime or potential applications.

Given the high hydroxyl group density of the hybrid, there is a high affinity to water, as evidence by the contact angle measurements, and thus swelling of the hybrid can be dependent on the humidity of the system. This opens the potential for humidity sensors

using hybrid-based DBRs, and extension of this to the near-IR range to create a reversible heat mirror. Global efforts to mitigate climate change has motivated an increase in research aimed at reducing energy consumed by central air units used for spaces cooling as the Energy Information Agency projects the energy needed for cooling is pacing to become the largest new contributor to the production of greenhouse gases by the year 2050.⁹⁴ The installation of improved thermal insulation materials has been shown to reduce the energy consumed by an average American residential building spaces by 41%.⁹⁵ Among these technologies' the installation of low emission (low-e) windows account for a reducing the heat transferred into a building envelop by 70%.⁹⁶ Low-E windows are not commonly used in developing nations due to their relativity high cost which stem from the processing and use of precious metals or metal oxides.⁹⁷ Additionally, to fabricate these low-E windows, oftentimes inorganic thin film devices are physically vapor deposited. Therefore, existing and highly transmissive clear glass windows cannot be modified to become Low-E windows with reduced radiative thermal conductance. The solution-processed hybrid-based DBRs can be deployed with a dynamically responsive photonic properties.⁹⁸

To quantify the DBRs dynamic response to water vapor, as cast and thermally treated hybrids film were exposed to 95% relative humidity at 22°C in a humidity chamber. Figure 1.26 shows representative effects of humidity exposure on the thickness and the refractive index of as cast hybrid films fabricated with 30 vol% Ti as a function of exposure time. Notably, the film thicknesses increase is sigmoidal with respect to time, which is not consistent with Fickian-like diffusion kinetics ($t^{\frac{1}{2}}$ dependency).^{99,100} This indicates that the H₂O vapor incorporation could be a convolution of both diffusion and reaction kinetics.¹⁰¹ This is consistent with the affects seen in the thermal stability of the hybrid after water

washing. In contrast the refractive index of the film experiences an immediate and sharp decline during initial exposure to the humidified environment. After this time, the refractive index is observed to gradually increase. The immediate decline in the refractive index and gradual increase in thickness agrees with literature findings on hysteresis effects characteristic of polymer gel systems.¹⁰²

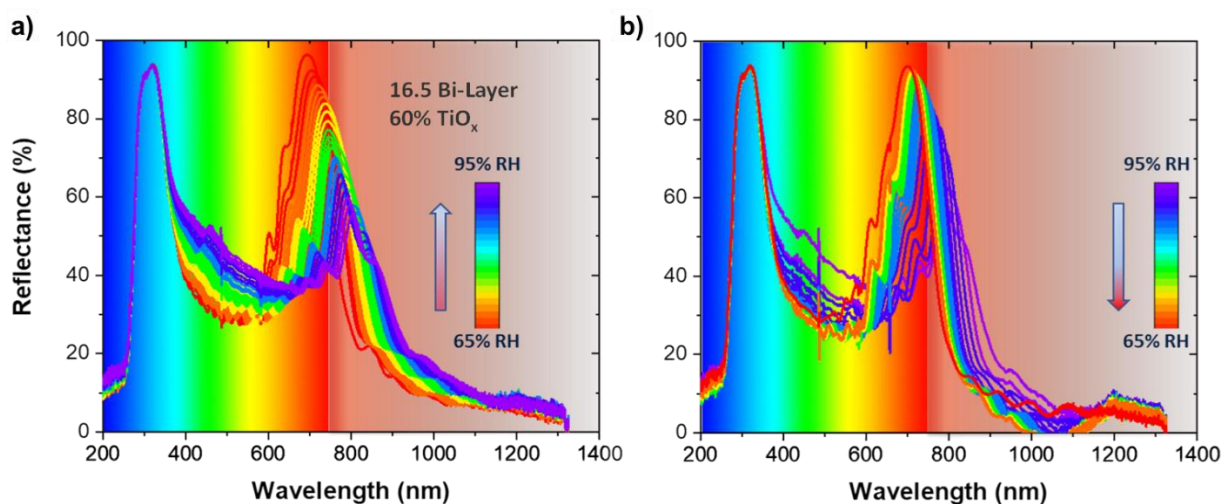


Figure 1.26 Humidity Responses of DBRs. In-situ reflectance UV-Vis-NIR spectroscopy of 16.5 bilayer DBR as a function of humidity cycling. Film characteristics while in the dry conditions at 65% relative humidity are denoted by the red line. Film characteristics while in the humidified state at 95% relative humidity are denoted by the purple line.

The swelling phenomena in single hybrid layers is believed to follow the thermodynamic principles of polymer swelling first presented through the Flory-Rehner polymer swelling theory. In detail water entering the structure has to provide enough energy to overcome configurational entropic forces that cause the polymer to coil. Once the driving force that promotes mixing between the solvent and polymer matrix exceeds this configurational free energy associated with elastic deformation the film begins to swell. The rate of swelling increases until the free energy associated with the elongated conformation for the polymer equilibrates with the free energy of mixing.^{103,104} This trend confirms that the effective

refractive index decreases upon the onset of humidification as low index water molecules immediately enter into the polymer hybrid matrix. Afterwards, chemical and/or density changes to the structure occur and mitigate additional decreases in the refractive index despite continued thickness increases.¹⁰⁵ Polymer swelling characteristics are theorized to depend on the crosslinking density of the hybrid. As the concentration of the titanium is increased, the swelling response in the presence of water vapor decreases. Understanding the precise physical and chemical mechanisms in each regime is an area of future investigation, however, this characteristic was exploited to investigate the dynamic behaviour of polymeric DBRs fabricated with hybrid films at specified concentrations of the hybrid material.

The peak reflection values corresponding to low and high RH condition also were shown to cycle between their original values of 96% and 53% respectively. The switching capabilities of the DBR structure lasted for 15 humidity cycles before the reflective properties became fixed. It is hypothesized that the free bonds believed to be present on the titanium species is capable of interacting with itself and other available bonding sites on the PVA. Further investigation of the crosslinking nature of this hybrid is critical to fully characterise and control the dynamic behaviour of polymeric DBRs for use as radiative shields and thermal switches.

1.5 Future Work and Conclusions

1.5.1 Titanium Oxide Hydrate:Polyalcohol Solutions

In addition to the solid-state with PVA, titanium oxide hydrates have been shown to be stabilized by small molecules in the liquid state.²⁷ This stability is attributed to the small molecule like glycerol having a high density of hydroxyl groups. Additionally, the titanium

species can be photoreduced and stabilized with these polyalcohols. Thus there is potential for energy storage applications including Photosynthetic Rechargeable Batteries (PSRB). A schematic of the PSRB set-up under flowing conditions is shown in Figure 1.27 in which an organic fuel is burnt using an illuminated Ti^{IV} oxide hydrate as an oxidizing agent in an endergonic photosynthetic reaction, the resultant stable Ti^{III} intermediate is stored and then discharged to generate electricity on demand.

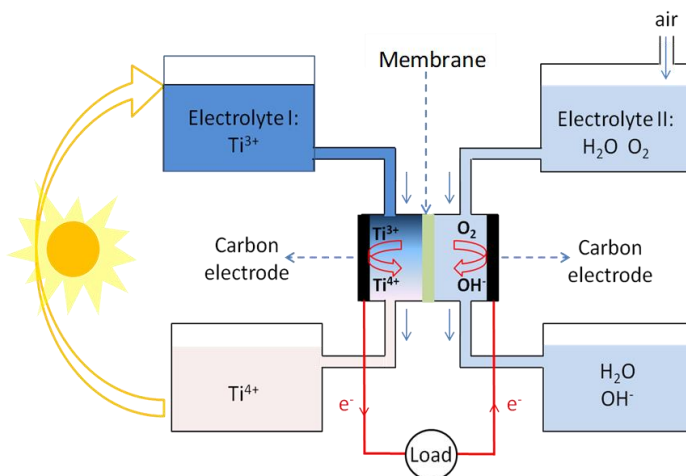


Figure 1.27 PSRB Schematic for Energy Storage and Production using titanium oxide hydrates

The PSRB concept is possible using a number of polyalcohols, but only glycerol and ethylene glycol have been investigated. In both cases, the titanium can be photoreduced upon UV-irradiation, as evidenced by solutions turning from transparent to colored. The polyalcohol is not expected to oxidize or reduce during irradiation as no evidence of new bonds are seen in FTIR. Figure 1.28 shows the responses of both the glycerol-based and ethylene glycol-based hybrids.

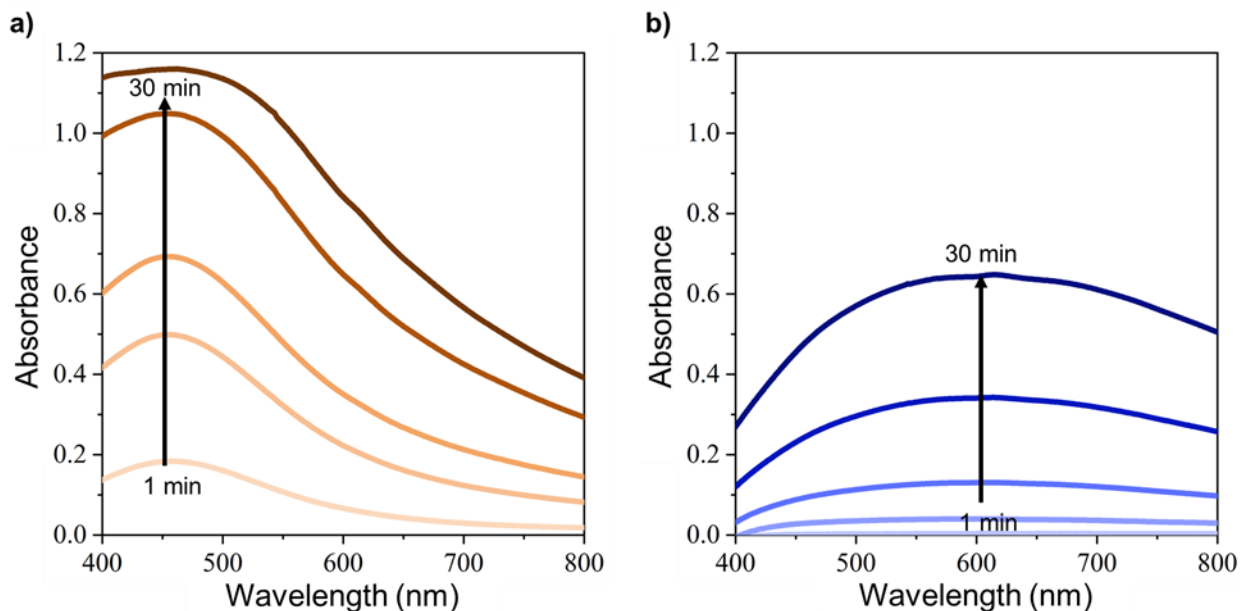


Figure 1.28 Absorption changes upon UV-irradiation of polyalcohol hybrids. (a) Glycerol-based titanium oxide hydrate hybrids exposed to UV-light, turning more amber in color with increased irradiation time. (b) Ethylene glycol-based titanium oxide hydrate hybrids exposed to UV-light, turning more blue in color with increased irradiation time. Glycerol-based hybrids have stronger absorption intensities for the same amount of irradiation time potentially due to the hydroxyl group density.

The hybrid solution, in the absence of oxygen, develops an amber color in glycerol and blue color in ethylene glycol potentially due to mononuclear and polynuclear species, respectively. The glycerol-based hybrid has a much higher absorption intensity for the same amount of irradiation time compared to the ethylene-glycol hybrid. This could be attributed to the glycerol having a higher stability of reduced titanium due to its hydroxyl group density. FTIR results in Figure 1.29 also show the same trend, with glycerol hybrids produced more water as an oxidation product during irradiation evidenced by the drop in transmission around 3700 cm^{-1} .

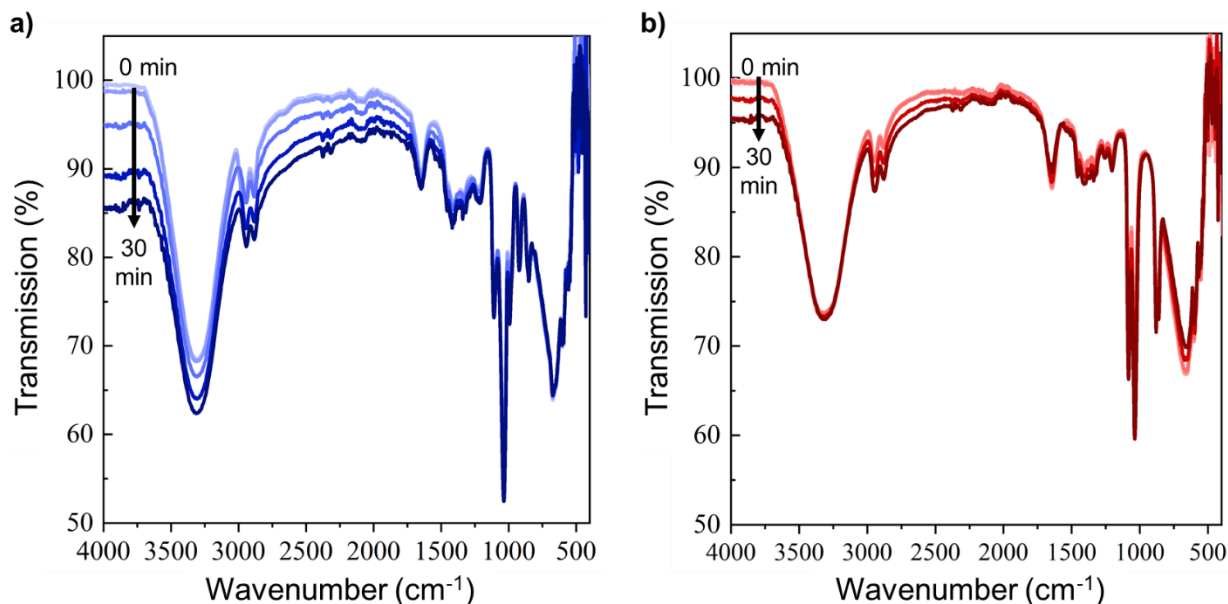


Figure 1.29 FTIR changes upon UV-irradiation of polyalcohol hybrids. (a) Glycerol-based titanium oxide hydrate hybrids exposed to UV-light, producing water as an oxidation product evidence by drop in transmission around 3700 cm^{-1} . (b) Ethylene glycol-based titanium oxide hydrate hybrids exposed to UV-light, producing water as an oxidation product evidence by drop in transmission around 3700 cm^{-1} . FTIR shows no redox reactions of the organic molecules.

The glycerol hybrid also shows more water production than the ethylene glycol which aligns with the higher absorption intensity. The glycerol is likely a better stabilizer of the reduced titanium and the proposed interactions are shown in Figure 1.30.

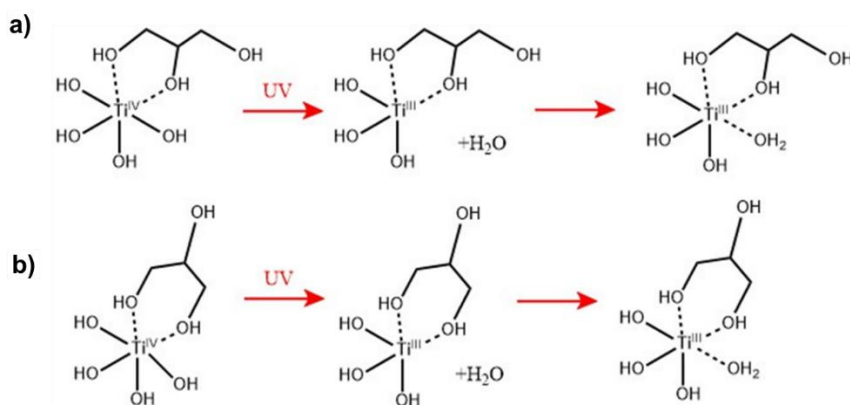


Figure 1.30 Proposed Intermolecular Interactions of Polyalcohol hybrids. (a) 5-membered ring stabilized structure. (b) 6-membered ring stabilized structure.

As the 6-membered ring is evident in PVA-based hybrids, it is reasonable to believe the titanium is better stabilized by this instead of a 5-membered ring that ethylene glycol must form. The increased stability of the 6-member ring also aligns with the increased production of water in FTIR. Further investigations into the photoreduction of titanium species and stored voltages of the hybrids are required for the PSRB, as concentrations and pH are likely to play a role.

1.5.2 Future Work: New Hybrid Formulations and Processing

With the knowledge of the interactions between the titanium oxide hydrate and PVA, new hybrid chemistries can be explored. Focus can be first set on the exploration of other titanium oxide hydrates that do not come from titanium tetrachloride, as to avoid the highly toxic hydrolysis due to the release of HCl vapor. pH still plays a large role in the interactions, so a low pH will still need to be reached, however, addition of other acids like acetic acid may be explored. Even if HCl is still required, removal of the titanium tetrachloride hydrolysis still removes the HCl vapor from the process. In addition to other titanium precursors, other metal oxide hydrates can be investigated. Metals like zirconium and hafnium have a similar valence shell configuration so the chemical behavior can be expected to be similar to titanium.

Other than exploration into new metal oxide hydrates, the processing of the hybrids can be investigated. Even though solution processing is scalable and promising in semiconductor and photonics devices, melt processing is highly advantageous in production of large optical fibers. A melt-processed high refractive index hybrid would have several applications in fiber optics and waveguides. In order to achieve melt-processed hybrid, considerations into the toxicity of the titanium oxide hydrate is necessary, therefore, the

titanium tetrachloride precursor likely should be avoided. There are several other candidates like titanium alkoxides which have organic degradation products like isopropoxide. Water based titanium oxide precursors like titanium bis(ammonium lactato)dihydroxide are soluble in water and can lead to more 'green' options. Additionally, PVA degrades easily beyond its melting temperature so it is not easily melt-processed without the addition of plasticizers. In this case, glycerol make be a great candidate as it can interact with PVA and titanium oxide hydrate which will create a more homogenous film. PVA can also be copolymerized with polyethylene, creating EVAL, a common barrier material in packaging. The copolymer will have a lower melting temperature than neat PVA and thus could be melt processed below degradation temperatures. The copolymer can phase separate due to the large differences in polarity between the two monomers, however, the crosslinking may limit this. Expansions to new polymers can include poly(acrylic acid) or poly(styrene sulfonic acid), and copolymers of varying hydrogen bonding densities.

1.5.3 Conclusions

This thesis has discussed the development of a high refractive index, solution-processable hybrid material. This is achieved through a pseudo-one-pot synthesis of hydrolyzed titanium tetrachloride and PVA. The hybrid material is shown to have a tunable refractive index between ~1.5 and ~2.1 with low optical loss in the near-IR and visible wavelengths. Without evidence of optical scattering, investigations into the interactions between the titanium oxide hydrate and PVA took place. Thermal and x-ray spectroscopy measurements indicate that the titanium oxide hydrates form a bidentate-like covalently

crosslinked PVA network. This chemical crosslinking is the reason for the absence of diffuse scattering points as it limits growth of inorganic particles.

The solution processed hybrid is a great candidate for photonic applications, in particular, distributed Bragg reflectors. The high refractive index of the hybrid allows a larger refractive index contrast between layers of the DBR. When a 60 vol% Ti hybrid is paired with PMMA in DBRs, high strong reflection bands are achieved in only 16 total bilayers. These strongly reflecting and tunable DBRs are paired with semi-transparent solar cells to improve power conversion efficiencies. The selectively reflecting DBRs and semi-transparent solar cells allow for transparency to chlorophyll absorption bands critical to plant growth, thus show great promise in greenhouse applications. In addition to visible light reflection, near-IR light which is responsible for heat generation can be reflected using hybrid-based DBRs. This can lead to passive cooling in buildings, with hybrid-based DBRs using only a fraction of layers and materials as current commercial options. We also measured the thermal conductivity of the DBR stack that has a reversible stopband. The reversible stopband is advantageous in building energy management, as the near-IR light transmission can be easily tuned with humidity changes. The hybrids are able to quickly well under high humidity conditions and thus break the coherence of the multilayer stack. The reversible stopbands of the hybrids and its sensitivity to humidity can be further explored in the Stingelin lab as humidity sensors. The hybrid material discuss is highly versatile and has several applications in optics and photonics. Additionally, the knowledge gained through the physical and chemical investigations has created a platform to predict new inorganic components which may have different electrical or magnetic properties.

2 Fast Scanning Calorimetry

2.1 Introduction

Differential scanning calorimetry (DSC) is an effective tool in polymer characterization and is used to measure phase transitions through changes in heat capacity or latent heat. Generally, melting of polymer crystals occurs with a relatively large latent heat which is easily detectable in conventional DSC. However, in semi-crystalline polymers and polymers that can exhibit multiple partially ordered phases like liquid crystals, the associated heat capacity changes and latent heats become smaller.¹⁰⁶ The output from DSC is generally a heat flow that is a product of the material's mass, heat capacity, and temperature scanning rate. Since, heat flow is directly proportional to the scanning rate, a larger signal can be obtained by scanning faster.¹⁰⁷ Most conventional DSCs can access rates up to a few hundred degrees Celsius per minute. However, this is still well below the time scale that commodity polymers like polyethylene and polyamide require to achieve a fully amorphous material.^{108,109} Additionally, in conjugated polymers, the step-change in heat capacity is greatly reduced with increased backbone rigidity and bulky side-chains due to an increased glassy-state entropy.¹¹⁰ This need for faster scanning rates and resolution has led to ultrafast chip calorimeters capable of exceeding 10^3 °C/s heating rates. First custom-made chip calorimeters were developed^{111,112} and eventually the first commercial chip calorimeter, Mettler Toledo Flash DSC 1, was produced in 2010.

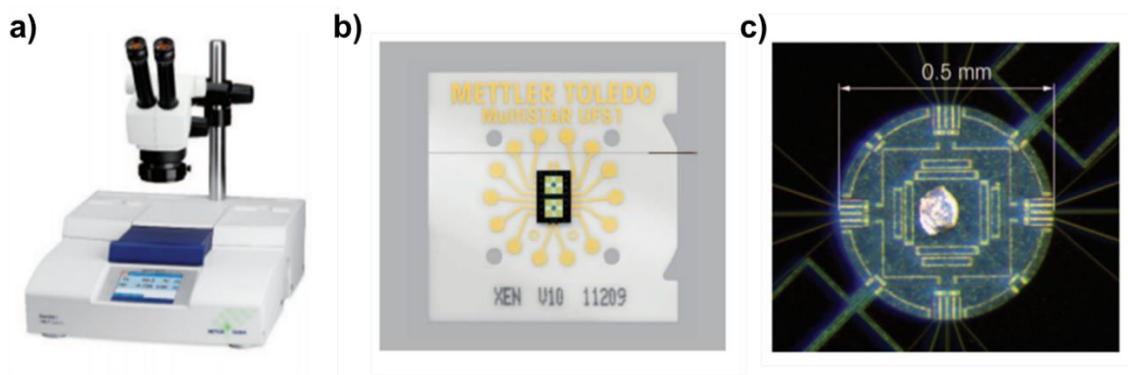


Figure 2.1 Mettler Toledo Flash DSC 1 (a) Mettler Toledo Flash DSC 1 Apparatus (b) UFS 1 Chip Sensor (c) Polarized Microscope Image of Sample Sensor with typical sample

The Flash DSC 1 is capable of heating from 1 to 40,000 °C/s between -100 °C and 450 °C which covers 5 frequency magnitudes and temperatures which cover nearly all major phase transitions of polymers. The small sample size, generally between 10 ng and 10 µg, limits thermal lag within the sample. Additionally, with such a small sample size, it is possible to measure thin films of polymers, thus preserving the same microstructure producing upon processing, instead of using a drop-casting method that has slightly different drying conditions compared to spin- or bar-coated films. The following chapter will discuss how the Flash DSC, and fast scanning calorimetry in general, can contribute to the structure-property interrelations of semiconducting polymers.

2.2 Glass Transitions and Physical Aging

Even with the high resolution of fast scanning calorimetry, identification of the glass transition can still be difficult, therefore different methodology is required. Instead of identifying the glass transition as a step-change in heat capacity, we can identify its properties as a metastable state. The glass transition occurs during cooling, as volume and molecular mobility decrease in the system, it reaches a point where equilibrium can no longer be achieved in the time scale of the experiment.¹¹³ This frozen-in structure is the

glassy state and the temperature at which it occurs is the glass transition temperature. The glass transition temperature is also cooling rate dependent, with fast cooler rates leading to larger glass transition temperatures.¹¹⁴ However, if extrapolated, then an ‘infinitely slow’ cooling rate could lead to an entropy of the glass being lower than that of the crystal and is known as the Kauzmann Paradox.¹¹⁵ To combat this, Gibbs and DiMarzio showed that there is an underlying second-order thermodynamic transition to the glass transition and their reported ideal glass transition temperature is often similar to the Kauzmann temperature.¹¹⁶ Pyda and Wunderlich showed that the Kauzmann paradox can be solved as reduction of the liquid entropy with decreasing temperature and that the external contribution of the equilibrium liquid leads to a positive residual entropy for amorphous polyethylene.¹¹⁷

In addition to the cooling rate dependence, the glassy state is also a non-equilibrium state. In the glassy state a material will slowly densify and become stiffer and more brittle. This process is known as physical aging.¹¹⁸ There is also an associated decrease in volume and enthalpy through small conformation movements toward an equilibrium, and this process is known as structural recovery.¹¹⁹ For the purpose of this thesis, physical aging and structural recovery will be regarded to as the same process. This physical aging and structural recovery lead to an enthalpic overshoot at the glass transition temperature upon heating in calorimetry. This enthalpic overshoot, also known as enthalpic recovery, only occurs when the material is held at a temperature in its glassy state and can be described by in Equation (2.1)¹²⁰:

$$\Delta H(T_a, t_a) = \int_{T \ll T_g}^{T \gg T_g} \left(C_p^{aged}(T) - C_p^{ref}(T) \right) dT \quad (2.1)$$

Where ΔH is the recovery enthalpy, C_P is the heat capacity of the aged and reference samples, and the integral is taken from well below the glass transition temperature, T_g , to well above the glass transition.

The Flash DSC is especially suited for measure recovered enthalpy because of its high resolution and fast scanning rate. The high resolution is advantageous because recovered enthalpy is sometimes a weak signal compared to the rest of the curve. Since the amount of recovered enthalpy is dependent on the time spent below the glass transition temperature, it's important to spend as little time possible which is accomplishable with the Flash DSC. Figure 2.2 describes the procedure performed to scan for physical aging signatures using the Flash DSC.

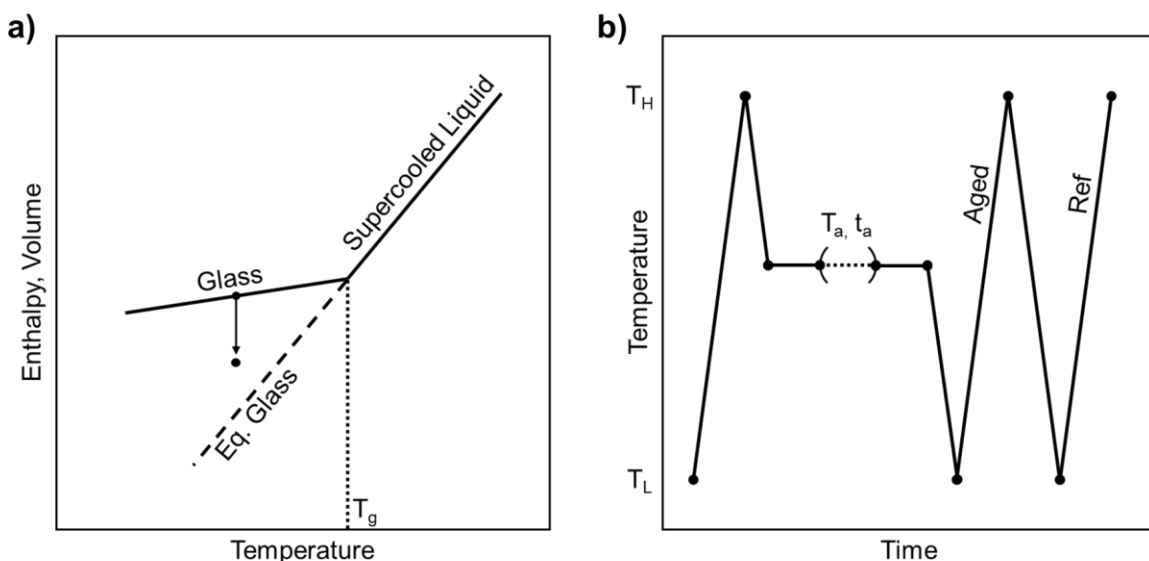


Figure 2.2 Physical Aging (a) Representation of the reduction in enthalpy or volume during structural recovery as the material relaxes towards the equilibrium glass state (b) This physical aging method creates an “Aged” heating curve and “Reference” heating curve with different thermal histories. This difference in these two curves is analyzed for structural recovery effects.

Both the aging temperature (T_a) and aging time (t_a) are varied depending on the particular sample. T_H and T_L are the high and low temperatures, respectively, that the sample is cycled

to. T_H must be sufficiently high enough remove any previous thermal history, which is generally above the isotropic melting point. T_L needs to be arbitrarily low enough such that a good baseline is achievable prior to the enthalpic recovery signatures. Even though the cooling steps are fast (>1000 °C/s), aging will still occur during this process. The cooling steps occur on the time scale of ~ 1 ms so the intended aging steps should be much larger and generally done for 1800 seconds (30 minutes).

Unless otherwise stated, the Flash DSC data in this chapter will be the resulting curves from this method. All heating and cooling is performed at 4000 °C/s and isotherms for physical aging will be held for 30 minutes. There is also a 1 second isotherm held at -90 °C after each cooling step to -90 °C which is there to allow the system to quickly equilibrate before heating. This improves the baseline on heating at the low temperature range and is expected to have negligible effects on the aged and reference curves. The full physical aging scanning process will use the same length of isotherms, with temperatures that changes in increments of 5 °C.

All of the following measurements in this chapter were performed on a Mettler Toledo Flash DSC 1 equipped with a Huber TC100 cooler to control the temperature between -90 °C and $+450$ °C and with a nitrogen flow over the sample at 40 mL/min and 25 psi. Deposition of the samples are performed through direct deposition of a powder or flake onto the chip or through spin-coating onto the back of the sample sensor. Direct deposition is performed by placing the powder or scraped-up film onto the sensor with the bristle of a paintbrush. A silicone oil was sometimes used to help improve thermal contact with the sensor and the oil generally has no significant thermographic features. Spin-coated samples are deposited onto the backside of the sample sensor, with a glucose mask covering the

reference sensor to be washed off with water following deposition. This procedure is described in *Fast Scanning Calorimetry*.¹²⁰

2.3 Semiconductors and their Side-Chains

Organic (polymeric) semiconductors have a number of advantages compared to their inorganic counterparts including being lightweight and low-temperature and solution processable. Applications include, among others, organic photovoltaics (OPVs), organic field-effect transistors (OFETs), and organic electrochemical transistors (OECTs).

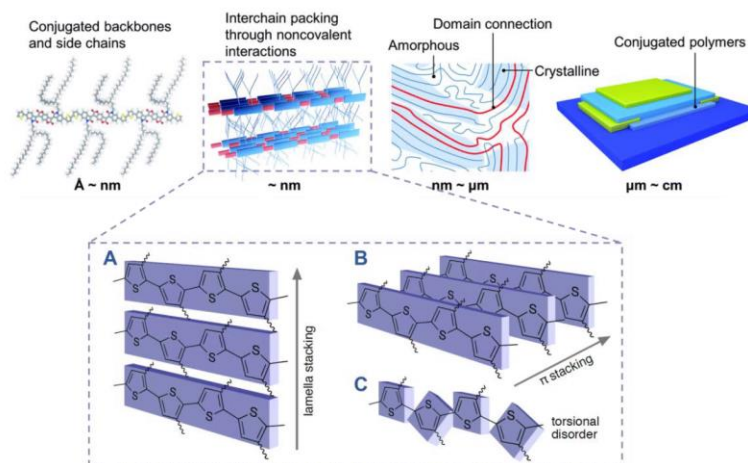


Figure 2.3 Multi-level microstructural features of Conjugated Polymers. Several length scales from molecular packing to interchain interactions to crystalline microstructure and phase morphology.¹²¹ Side-chain chemistry and structure can affect the interchain interactions like lamellar stacking (A), π - π stacking (B) and torsional disorder (C). (Credits for A-C: Matt Dyson)

Each device requires slightly different design and operation principles which means variations among the chemical structures. Thus structure-property interrelations will vary slightly among the devices discussed, however, a major thermal property that dictates many processes and properties is the glass transition temperature. The glass transition temperature of polymers is dependent, among other factors discussed earlier, on the chemical structure. Conjugated polymers consist generally of two parts: a conductive π -

conjugated backbone, and solubilizing side-chains. The focus of this chapter is on the solubilizing side-chains in conjugated polymers which are required for solution processing.

¹²² As these side-chains are necessary for processing, there is a great deal of work on the affects that different side-chains have on OSCs. This realm is known as side-chain engineering and can include tuning for high conductivities¹²³, doping mechanisms and kinetics¹²⁴, and even allowing for solubility in more green-friendly solvents.¹²⁵ However, the effects side-chains and glass transition temperatures as well as side-chain ordering is often overlooked, generally due to the difficulty of the measurement. The following sections will discuss how side-chains affect the glass transition temperature and other local ordering which affects thermal, mechanical, and optoelectronic properties. All relevant chemical structures, if not shown directly in the section, can be found in Appendix A.

2.3.1 OPV Materials

Organic photovoltaics (OPVs) have progressed rapidly in recent years with devices that surpassed 17% power conversion efficiency.^{126,127} The general design for the OPV active layers rely on bulk heterojunction architectures consisting of an electron-donating and electron-accepting component. The interactions between these two components is complex with phase mixing and separation both possible in a device and optoelectronic processes are heavily dependent on this morphology.^{128–130}

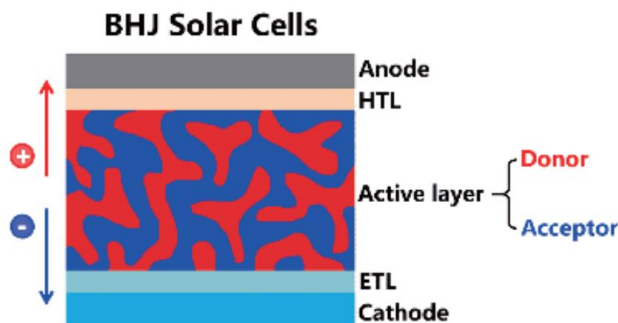


Figure 2.4 Bulk Heterojunction Architecture Schematic. Intermixing of the donor material (polymer) and acceptor material (fullerene, NFA) allows for efficient charge generation, separation, and transfer to respective electrodes.¹³¹

The two molecules are compatibilized in solution and generally kinetically trapped during processing due to fast solvent evaporation, however, the rate at which the molecules will separate is dependent on their mobility and therefore glass transition temperatures.^{132,133}

Post-process thermal annealing is common in OPVs as it can increase the crystallinity of the donor polymer and lead to higher efficiencies.¹³⁴ Growth of polymer crystals cannot occur below the glass transition temperature, and is both temperature and time dependent, therefore knowledge of the glass transition temperature is highly advantageous.¹³⁵

Additionally, the degree of intermixing of donor and acceptor molecules in the amorphous phase can affect the glass transition temperature.¹³⁶ Thus, to develop structure-property interrelations and proper processing conditions for OPVs, knowledge of the glass transition temperature is highly advantageous. In addition to device performance, device stability is also affected through phase separation and chemical degradation. Several degradation pathways exist for OPVs but generally involve light, oxygen, heat or any combination of the three. In polymer:fullerene OPV blends, light- and oxygen-induced degradation occurs through photo-oxidation of the polymer due to fullerene-mediated superoxide formation.¹³⁷

Additional control of the lowest unoccupied molecular orbital (LUMO) to a deeper energy level can improve the fullerene stability and reduce superoxide formation and at the same

time deepening the polymer highest occupied molecular orbital (HOMO).¹³⁸ Proper device encapsulation to prevent oxygen and moisture from penetrating the active layer can improve stability.¹³⁹ However, heat and light can still affect barrier coated devices and cause ‘burn-in’ affects that lead to degradation.¹⁴⁰

Thermal annealing of a bulk heterojunction device near the T_g can lead to vertical phase separation and the polymer can form an electron blocking layer at the electron extracting electrode.¹⁴¹ Even sub- T_g annealing can lead to local changes in nanostructure and thus device performance.¹⁴² Other sub- T_g relaxations can be light-induced, also known as photoplasticization¹⁴³, and has shown to cause planarization of conjugated polymer chains upon white light exposure and thus an increase photoluminescence.¹⁴⁴ There is a need to develop polymers with intrinsic stability in ambient and operational conditions, however with this, a knowledge base of precise degradation mechanisms that are chemical-structure dependent is required.

Even in inert atmosphere, light-induced dimerization of fullerenes leads to a reduce charge carrier mobility and this occurs in an inert atmosphere.¹⁴⁵ The degradation pathway under light and inert atmosphere for electron donated polymers however remains inconclusive. To address the effect of light, in particular UV-light, on conjugated polymers, we looked at poly[N-9'-heptadecanyl-2,7-carbazole-alt-5,5-(4',7'-di-2-thienyl-2',1',3'-benzothiadiazole)] (PCDTBT). PCDTBT-based OPVs have shown efficiencies over 7%¹⁴⁶ and has a relatively high stability in both air and nitrogen.¹⁴⁷ The high stability can potentially be attributed to its high T_g and therefore limited molecular mobility even in operating conditions.¹⁴⁸

To study the degradation pathways for PCDTBT, it was exposed to UV in inert atmosphere and then its physical, optical, and thermal properties were measured. The first step was dissolution of the film after UV exposures, and after only 32 hours of exposure, the film was no longer soluble in the same solvent as it was processed in. Gel permeation chromatography also confirms the reduced solubility as functions of UV-aging. The reduced solubility could be due to several factors including oxidation, chain-scission, and crosslinking. To address the issue of potential oxidation, absorption measurements on the UV-aged films is performed. There is a negligible change in the absorption spectra of PCDTBT which indicates that the conjugated backbone remains unchanged.¹⁴⁹ The stability of the backbone is consistent with other reports, so no photooxidation of the backbone is expected.¹⁴⁷ However, there is a slight reduction in the photoluminescence of the UV-aged PCDTBT which could be due to traps and defects.¹⁴⁹ This leaves two possibilities for the degradation pathway: side-chain scission or crosslinking.

In order to gain further insights into the origin of the reduced solubility, if not full loss of it, we used Flash DSC to measure the glass transition temperature of the neat and UV-aged PCDTBT. PCDTBT films were spun-cast directly onto the Flash DSC chip and UV-aged under the same conditions as the other films. UV-aging should not be confused with the physical aging of the material during the calorimetric measurement.

Figure 2.5 shows the enthalpic overshoots and extrapolated T_g 's for neat PCDTBT, 163 h UV-aged, and 531 h UV-aged. The physical aging isotherms are in increments of 10 °C. There is the gradual increase in the enthalpic overshoot with increasing aging temperature until a point that it starts to decrease as the T_g is approached. Additionally, when aged above the glass transition temperature, there is an endotherm occurring around 250 °C.

This high-temperature endotherm is indicative of PCDTBT's liquid-crystalline state.¹⁵⁰ The nematic liquid-crystal phase appears unaffected with UV-aging which is consistent with the unaffected backbone measured via absorption. In agreement with GPC and optical measurements, we find that the T_g increases from ~ 151 °C for neat PCDTBT, to 157 °C and 163 °C for films irradiated for 163 and 531 h. There is a slight increase in T_g and to verify these are not within error and in-fact real differences, we measured the activation energies of the glass transitions. Neat and 163 h UV-aged samples have relatively comparable glass transition activation energies, while the 531 h UV-aged activation energy drastically increases. A larger energy barrier to cooperative motion is needed to overcome the transition from the solid to liquid state which is expected for a more heavily crosslinked system.^{151,152} This thermal data along with optical data suggest that photodegradation of PCDTBT occurs through crosslinking of the side-chains. The side-chain are the suspected crosslinkers instead of the backbone because there is no evidence of backbone degradation. Additionally, chain-scission can be ruled out because smaller chains would be expected to plasticize the backbone and reduce the T_g .

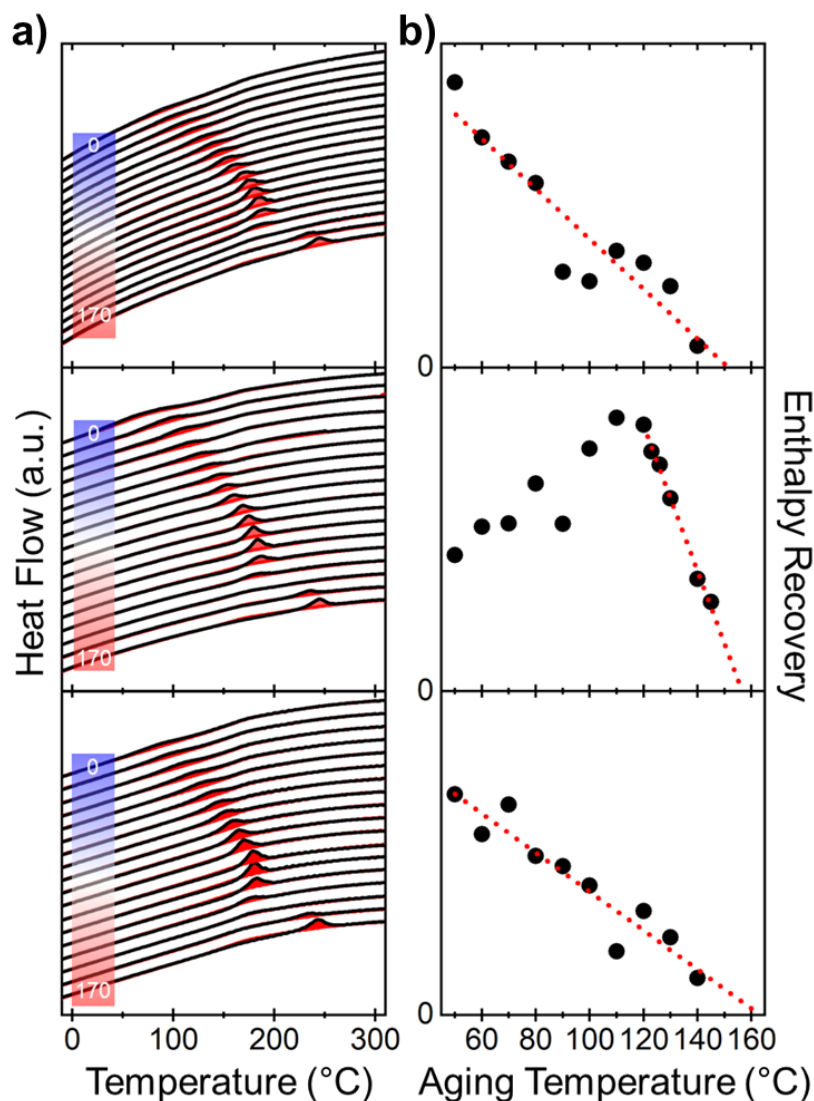


Figure 2.5 Glass Transition Temperatures of UV-aged PCDTBT. Physical aging (a) and enthalpic recovery (b) of neat (top), 150 hour (middle), and 500 hour (bottom) UV-aged PCDTBT. The glass transition temperature increases slightly with further UV-aging.

Design of intrinsically stable conjugated polymers that still require solution processing thus requires side-chain engineered designs that allow for chemical solubility but reduced reactivity to crosslinking. This system is not meant to be an all-encompassing explanation to the photostability of conjugated polymers, but instead a model system to show that even though backbones can be designed with superior thermal- and photo-stability, the side-chains can still attribute to degradation effects.

2.3.2 Hairy Rod Materials

Organic field effect transistors (OFETs), while sharing the same mechanical and processing advantages as OPVs, have also gained interest due to their high field effect mobilities which have surpassed amorphous silicon at $1 \text{ cm}^2/\text{V s}$.¹⁵³ A lot of the progress can be attributed to synthetic efforts in the form of new materials that often exhibit more rigid backbones than first generation polymer semiconductors like P3HT and PPV. The more rigid backbones often require long solubilizing side-chains for synthesis. The combination of these rigid backbones and long side-chains form what will be referred to as ‘hairy-rod’ polymers.

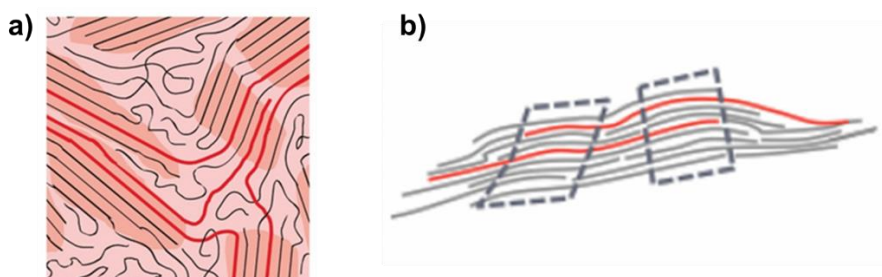


Figure 2.6 Evolution from Semi-crystalline to long, rigid chain microstructure. (a) Schematic of a semi-crystalline polymer film, like P3HT, with crystalline domains in darker highlight and amorphous fractions in lighter highlight. Long polymer chains (highlighted in red) can connect ordered regions also called tie-chains.¹⁵⁴ (b) Schematic of hairy-rod polymer ordering. Chains form more loosely ordered fraction leading to weaker and more diffuse x-ray scattering features and melting endotherms.^{154,155}

The high mobilities of these hairy-rod polymers also challenge previous thought that high degrees of crystallinity are required for sufficient charge transport. Generally, these hairy-rod polymers exhibit weak and broad crystal signatures in x-ray techniques. Additionally, thermal measurements show mostly flat signatures suggesting mostly amorphous materials. At the same time, the materials are generally brittle and not very flexible, contrary to what is expected of glassy polymers. The need for a better understanding of the microstructure and local ordering in these systems is required to develop more in-depth

structure-property interrelations. The following sections will describe the progress in describing the local ordering of hairy-rod polymers through investigation of side-chain and liquid-crystalline ordering among these hairy-rod polymers.

One of the first and model system of ‘hairy rod’ polymers is poly(2,5-bis(3-alkylthiophen-2-yl)

thieno[3,2-b]thiophene) (pBTTT). This polymer contains fused-thiophene rings with side-chains ranging from 10 to 16 carbons long, thus giving it a ‘hairy rod’ structure as it has a stiffer backbone than P3HT and longer side-chains. Hairy rod polymers are generally less ordered on a micro-scale and therefore show weaker crystalline peaks in x-ray techniques, but can order more locally with side-chain organization and liquid-crystalline-like phases through ordering of the backbones. PBTTT can order in three different forms, seen in DSC: side-chain ordering, thermotropic liquid crystal, and crystal. Each of these thermodynamic features appear at high temperatures than the previous, due to increased enthalpic driving forces. Figure 2.7 shows a typical thermogram of pBTTT-C16 measured using the Flash DSC. Upon heating, two endotherms are highlighted in blue: the side-chain softening and backbone melting at ~50 °C and 225 °C, respectively. Corresponding exotherms for each of these transitions are evident upon cooling. The backbone crystallization occurs at ~50 ° of supercooling (~175 °C) while the side-chain organization occurs at only ~10 ° of supercooling (55 °C). The difference in amount of supercooling is further evidence of the reduced order required for side-chain organization compared to backbone and decreased entropic effects. The thermotropic liquid crystal phase is not seen in this scan, however, it generally appears around 120-150 °C.¹⁵⁶

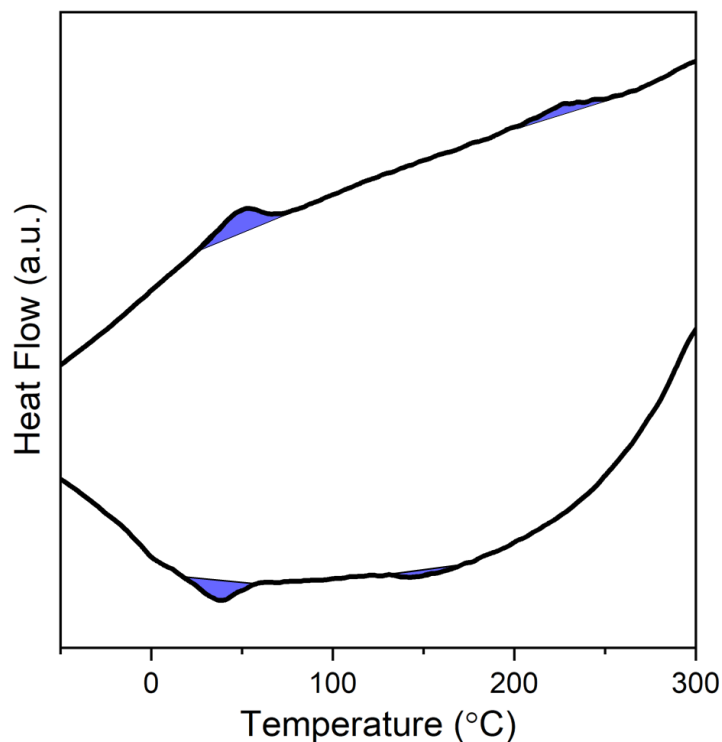


Figure 2.7 Heating and Cooling Curves of pBTTT-C16. Two distinct endotherms appear attributed to side-chain softening around 50 °C and the backbone melting around 230 °C with corresponding exotherms occurring at supercooled temperatures.

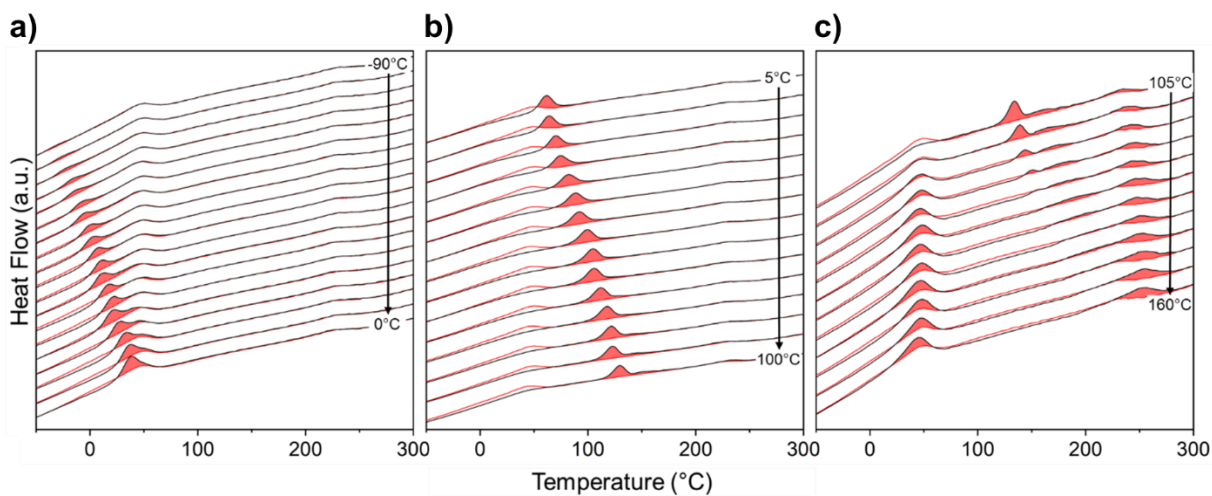


Figure 2.8 Physical Aging Signature of pBTTT-C16. (a) Low temperature aging signatures indicative of physical aging (b) Intermediate temperature aging range indicative of formation of the thermotropic liquid crystal (c) High temperature aging range showing the growth of side-chain ordering and backbone crystal growth.

Performing heating and cooling loops at a given temperature scan rate of this particular pBTTT can only inform on the side-chain and backbone ordering, thus further insight is

gained through isothermal holds at a wide range of temperatures. Figure 2.8 shows the aging and annealing curves after isotherms at low, intermediate, and high temperatures. In the low temperature aging regime, endotherms indicative of physical aging occur. Physical aging is the only expected process occurring in this range because the cooling curve in Figure 2.7 shows that the side-chain crystallization-like exotherm stops around 10 °C, thus no further crystallization/ordering processes are expected. Then, in the intermediate temperature regime, a decrease in the enthalpic recovery is expected, however the endotherms appear to plateau. This plateau is the expected growth of the liquid crystal phase, because the isotherms are above the onset of side-chain crystallization. Additionally, the glass transition temperature of pBTTT is roughly, 5 °C, thus no physical aging will occur above this temperature.¹⁵⁷ The slight increase in peak temperature of the liquid crystal melt as annealing temperature increases indicates slightly longer lamellar stacks of the liquid crystal. Finally, at high temperatures, the liquid crystal melt endotherm disappears around 120 °C, and instead, two endotherms appear. There is a low temperature endotherm indicating additional organization of the side-chains, and a high temperature endotherm indicating melting of pBTTT crystals/backbone melting. The increase in backbone ordering along with side-chain ordering is seen in other rigid conjugated polymers.¹⁵⁸ However, in rigid conjugated polymers with branched side-chains there is more competition between side-chain ordering and backbone planarity during solution processing.¹⁵⁹ There is a clear competition between the two, with different backbone flexibilities and side-chain densities playing a major role.¹⁶⁰ However, these previous studies are examination of the competing effects during solution processing or through simulations. Flash DSC aging experiments are examinations of a melt-process system. In

this case, planarization of the backbone, evident from more prominent melting peaks, is expected to be a pseudo-nucleating agent promoting side-chain organization. The comparably low density and long length of the C16 side-chains allows for large driving force for the side-chain to snap into the same plane as the backbone, thus showing large endotherm as well.

The side-chain organization clearly affects the optoelectronic properties, thus to gain further insight into the role of side-chains especially as it pertains to blended materials, we investigated the influence of fullerenes on the packing of pBTTT. Fullerene derivatives, commonly found in OPVs, are known to intercalate into the side-chains of pBTTT creating a pBTTT:fullerene co-crystal which is a 1-phase system, *i.e.* a solid solution.¹⁶¹ The amount of intercalation is dependent on processing¹⁶² as well as fullerene size and chemistry.¹⁶³ Intercalation is commonly measured via conventional thermal analysis and linear absorption spectroscopy, however, tracking the organization of the side-chains can also give insight to intercalation.

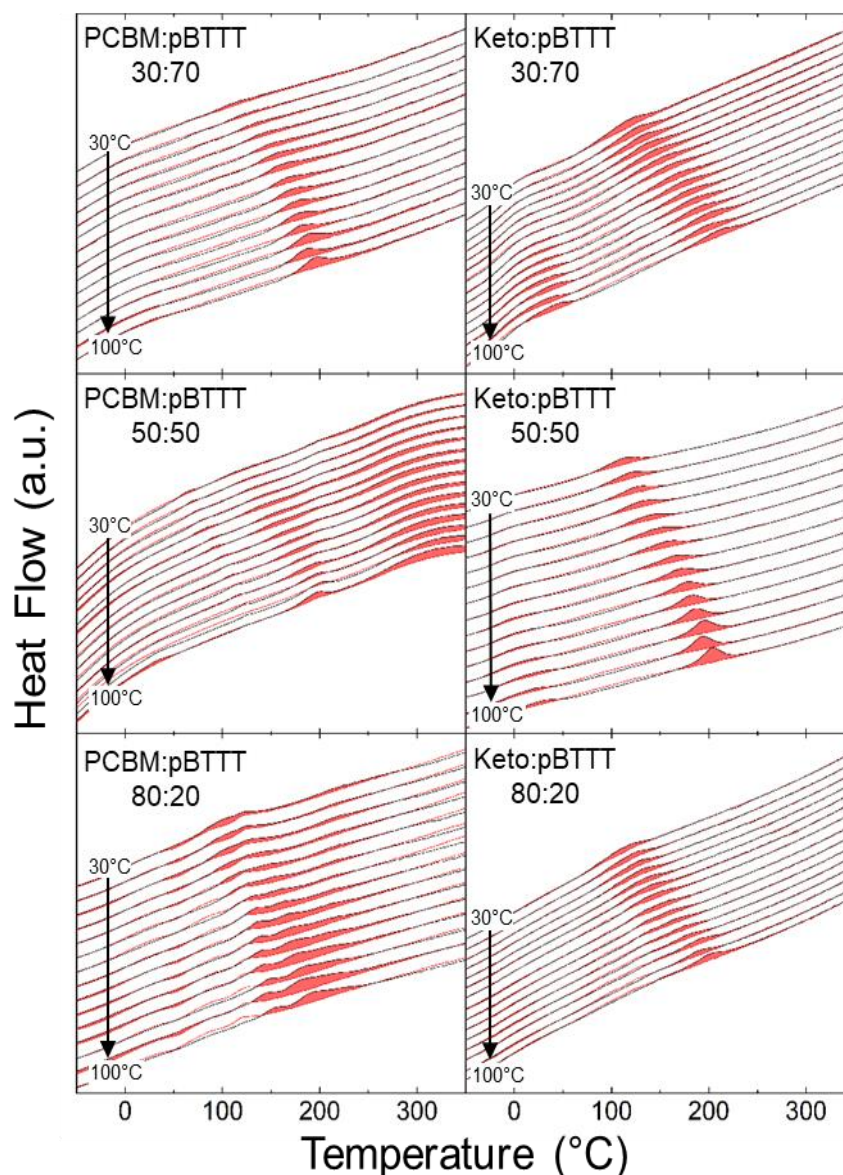


Figure 2.9 Fullerene Derivative Intercalation in pBTTT-C16. (left) Physical aging signatures of blends of PCBM and pBTTT (right) physical aging signatures of blends of ketolactam and pBTTT.

We looked at how two different fullerene derivatives, PCBM and ketolactam (Keto), intercalate into pBTTT-C16. These two fullerenes were chosen for their similar size and absorption behavior. Both systems show double eutectic phase behaviors with co-crystal formation occurring for each system.¹⁶⁴ Infrared vibrational spectroscopy also shows a shift in the CH₂-asymmetric stretch d-frequency in pBTTT which indicates that the all-*trans*

configuration in neat pBTTT side-chains is disrupted with fullerene intercalation.¹⁶⁴ Tracking the side-chain softening peak for these systems also provides information into the extent of intercalation achievable.

Addition of the fullerenes into pBTTT shows a clear decrease in the side-chain ordering with increasing fullerene content. Comparisons at intermediate aging temperatures, 30 °C – 100 °C, show that PCBM:pBTTT blends has a richer phase behavior at the same concentrations, indicated by the presence of several peaks, while ketolactam:pBTTT blends show weak and broad side-chain softening and (co-)crystal melting features. At high aging temperatures, 105 °C – 200 °C, the (co-)crystal melting features of PCBM:pBTTT blends maintain their sharpness, as well as limited change in peak temperature as a function of aging temperature. Ketolactam:pBTTT blends are shown to vitrify at these higher temperatures, which could be due to the relative thermodynamic stability of the co-crystal compared to the PCBM:pBTTT co-crystal, or the lower melting temperature of ketolactam have an influence on the temperature range at which supercooling can occur.

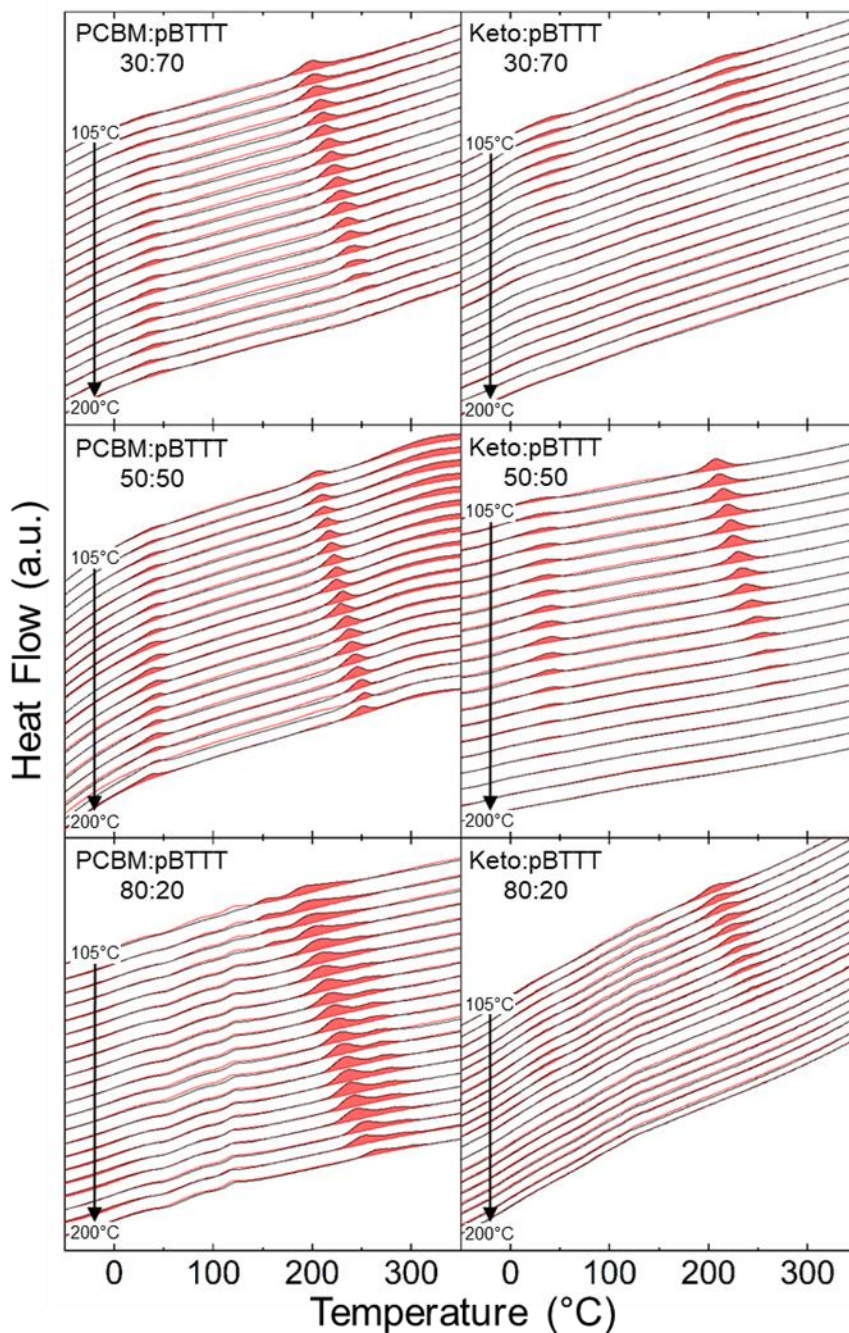


Figure 2.10 Fullerene Intercalation into pBTTT-C16. (left) Physical aging signature of blends of PCBM and pBTTT-C16 (right) physical aging signatures of blends of ketolactam and pBTTT-C16.

The side-chain softening feature of pBTTT is more suppressed in PCBM blends compared to Ketolactam, so tracking the enthalpy of the transition is more difficult. However, when comparing the side-chain softening enthalpy to that of the backbone/co-crystal melting in

ketolactam:pBTTT blends shows a clear decrease of the side-chain softening compared to the backbone. Additionally, clear endotherms of each transition are seen in lower fullerene content blends, likely due to the presence of a pBTT-rich phase in 2 of the measured blends and the hindered molecular intercalation of Ketolactam.

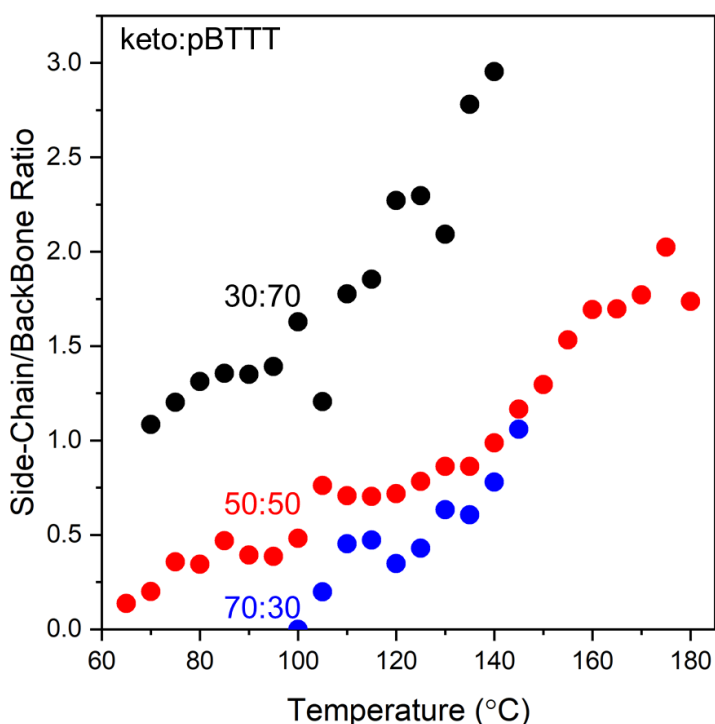


Figure 2.11 Comparison of Side-chain Ordering to Backbone Ordering in Ketolactam:pBTTT Blends. The decreased ratio of the side-chain ordering to backbone ordering with increase ketolactam weight ratios suggest that the ketolactam interrupts the side-chain ordering of pBTTT.

The knowledge gained on pBTTT phases can thus be extended to newer generation polymers that exhibit even more rigid backbones.

New high performing semiconducting polymers surpassing the benchmark mobility of $1 \text{ cm}^2/\text{Vs}$ of amorphous silicon.^{165–168} Generally, these polymers use both electron donor groups and electron acceptor groups in their repeat units leading to several fused rings and a more rigid backbone. Even though mobilities are increasing, the long-range order is

weaker compared to the more flexible polymers like P3HT.¹⁶⁹ This reduced long-range order contradicts the previous knowledge of semiconducting polymers, where high crystalline generally lead to higher mobilities.^{170,171}

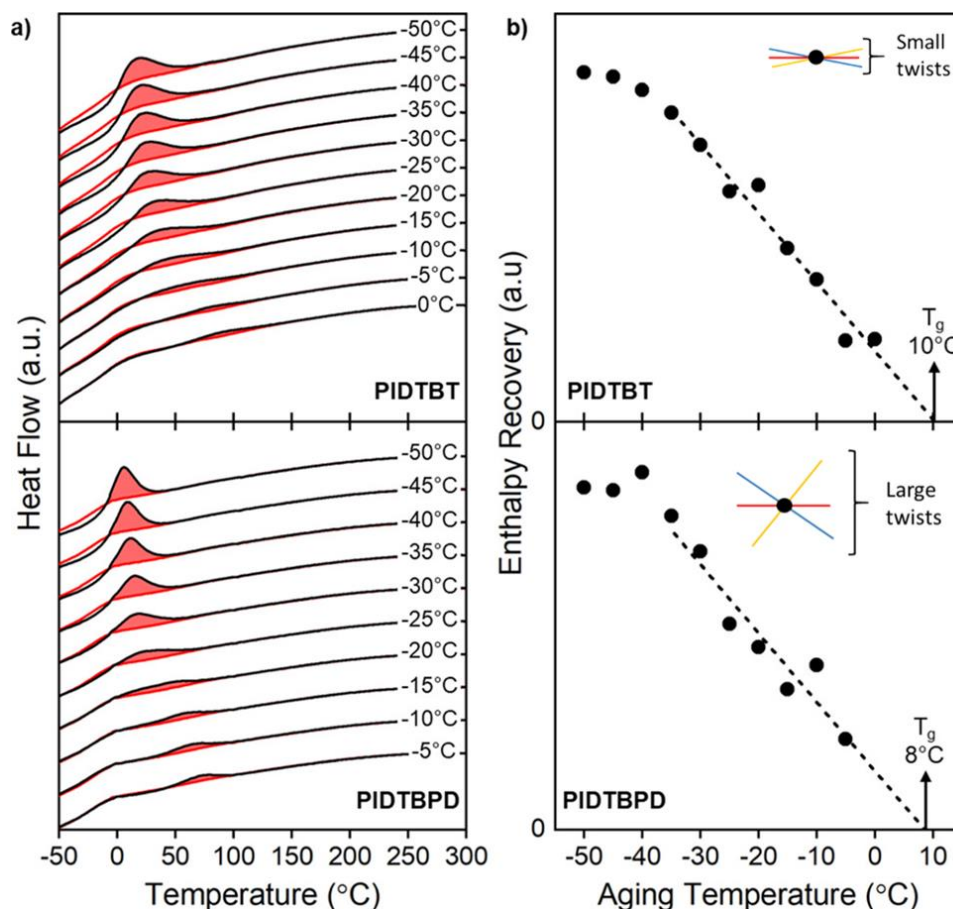


Figure 2.12 Glass Transitions of IDT Copolymers with different backbone torsion (a) Physical aging signatures of PIDTBT (top panel) and PIDTBPD (bottom panel). (b) Enthalpy recovery of PIDTBT (top panel) and PIDTBPD with extrapolations of the glass transition temperature.

The high device performance helps expand the potential applications for plastic electronics, in particular, deformable electronics.¹⁷² The non-crystalline nature of these polymers may be able to handle the mechanical stresses for deformable electronics. However, high mobility polymers like pBTTT and indacenodithiophene-co-benzothiadiazole (PIDTBT), are prone to brittle failure at low strain¹⁷³, and even though higher molecular weight

PIDTBT (>200 kg/mol) can help improve the ductility, plastic deformation still starts at about 5% strain with failure occurring at about 40%.¹⁷⁴ Chemical changes to PIDTBT can improve the ductility, for example substitution of the benzothiadiazole for a benzopyrrolodione unit (PIDTBPD) increases the crack onset strain from 3 to over 100%.¹⁷⁵ The reason for this large increase in crack onset strain however is unclear.

Thus we looked at a series of copolymers with varying amount of the benzopyrrolodione unit. Density functional theory calculations show that the PIDTBT has a highly coplanar backbone.¹⁷⁶ As a large increase in ductility is expected when above T_g , two homopolymers were measured, PIDTBT and PIDTBPD. If there is a difference in glass transitions between these two homopolymers, then the copolymers likely have a correlating change in their T_g . Figure 2.122 shows the T_g s of PIDTBT and PIDTBPD at 10 °C and 8 °C, respectively show that the chemical structure has little influence over the glass transition temperature. Thus the large difference in the crack-onset strain cannot be solely explained by T_g , and since room temperature (~20 °C) is greater than these, another process must be the cause. When annealing the samples above the T_g , seen in Figure 2.13, two endotherms appear. The presence of these endotherms suggest possible liquid-crystalline or liquid-crystalline-like transitions, like that of pBTTT, as well as side-chain softening. Indeed, the lower temperature endotherms are similar to of sub- T_g transitions of CPs attributed to side-chain motion.^{177,178} For PIDTBT, this transition peaks around 25 °C while the same transition peaks around -5 °C for PIDTBPD. Above the side-chain softening peaks, the polymers are expected to gain sufficient motion to allow for more ductility. The PIDTBT is thus only partially softened at room temperature, locking backbones into more frozen states, and reducing backbone motion, while the PIDTBPD has more freedom of motion at room

temperature due to the side-chains being fully softened. Since the polymers contain the same length, density, and sterics, the large difference in temperature of the side-chain softening in these polymers is due to the relative backbone planarity of each. The PIDTBT is more planar along the backbone, therefore, there is a large enthalpic driving force for the chains to order in the same plane, while the more torsionally disordered PIDTBPD does not have the same driving force for in-plane ordering.

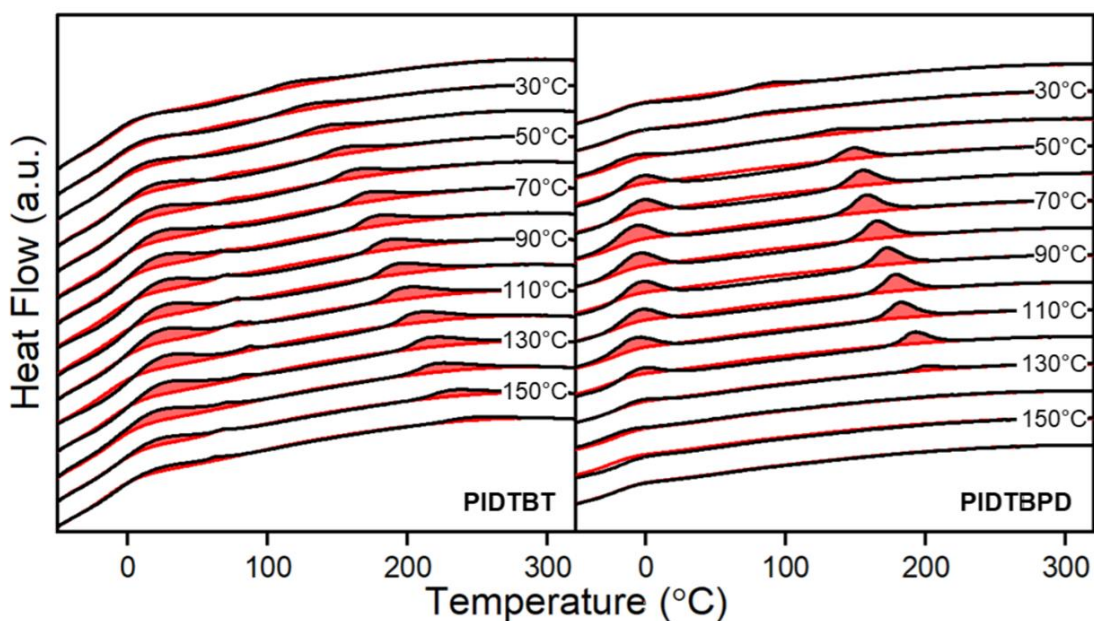


Figure 2.13 Side-chain and liquid-crystalline-like ordering of IDT copolymers. PIDTBT (left) and PIDTBPD (right) using annealing temperatures. Two distinct endotherms appear when annealing samples above the glass transition temperatures, indicating liquid-crystalline or liquid-crystalline-like transitions.

In addition to the side-chain softening endotherms, both polymers exhibit high temperature endotherms reminiscent of liquid-crystals. These endotherms indicate that some ordering at least in one direction occurs in these systems, despite the lack of long-range order detected by x-ray techniques. PIDTBT also exhibits higher liquid-crystalline-like endotherms than PIDTBPD. As with the side-chain softening, this liquid-crystalline-like endotherm temperature is likely affected by the planarity of the backbone. A more planar

backbone will increase the enthalpy required to melt. The more-planar backbone of PIDTBT is also confirmed with DFT, and the hole mobility is also about an order of magnitude larger than PIDTBPD which could be due to better conjugation lengths.

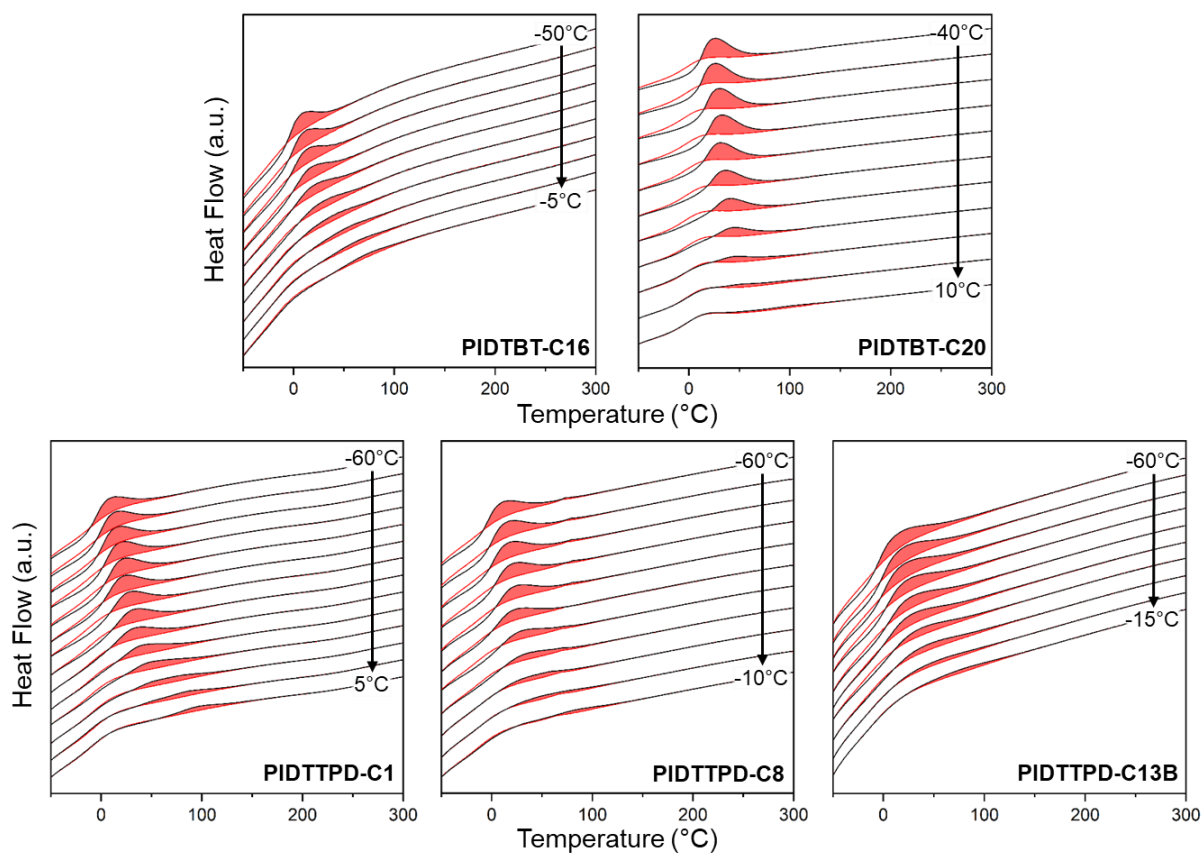


Figure 2.14 Physical Aging of Planar IDT Copolymers. Aged and reference curves of IDT copolymers with aging temperatures listing on the right in increments of 5 degrees per line pair.

Extensions to this correlation between side-chain softening and backbone planarity and how this affects mechanical and optoelectronic properties can be explored. By extending the side-chain length from 16 to 20 carbon atoms but maintaining the same backbone allows for examination of the entropic effect that side-chains have on the backbone T_g . Figures 2.14 and 2.15 show the enthalpic recoveries and extrapolated T_g s of a new set of IDT polymers. This PIDTBT-C16 has the same T_g as reported earlier, however, PIDTBT-

C20 has an even higher T_g at 20 °C. This higher T_g is likely due to the large increase in molecular weight of the C20 samples which is about 30 kg/mol compared to PIDTBT-C16 at 10 kg/mol. Glass transition temperatures are known to decrease significantly when the molecular weight is below about 10 kg/mol and be relatively unaffected at higher molecular weights.⁶⁰ Further discussion on this increase in T_g can be found in Section 2.3.4 as other factors may influence the glass transition.

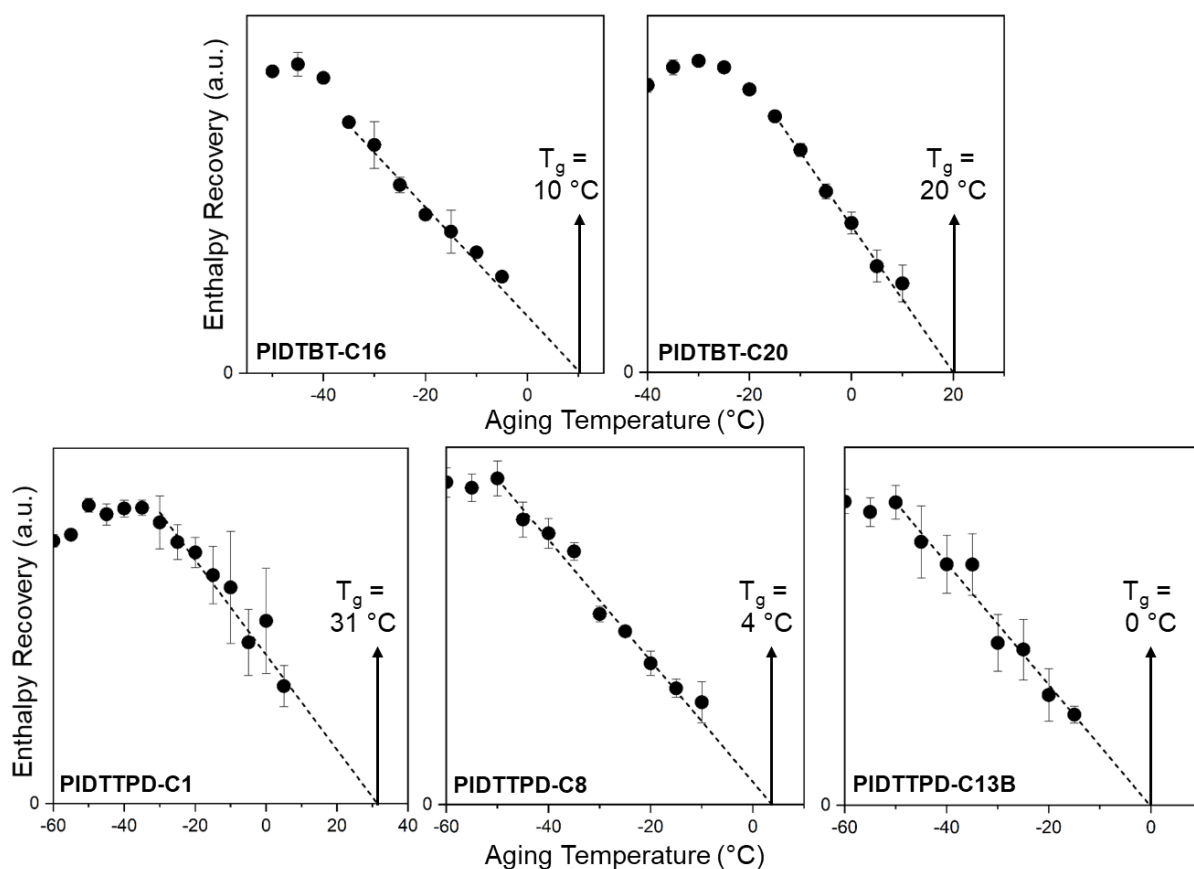


Figure 2.15 Glass Transitions of Planar IDT Copolymers. Enthalpic recovery versus aging temperatures with linear extrapolations to estimate glass transition temperature.

This new series of IDT polymers include a series of PIDTTPD polymers with varying side-chain lengths on the TPD unit. TPD was chosen as the next model system because it has an even more planar backbone than PIDTBT.¹⁷⁶ The TPD unit appears to have a slightly higher T_g than PIDTBT when the side-chain is only 1 carbon long on the acceptor unit.

Additional increase of side-chain length from 1 to 8 carbons long decreases the T_g by 27 °C. Then an additional increase to 13 carbons long only decreases the T_g by 4 °C, however this sample has a side-chain that includes a branching position which have been shown to increase T_g due to decreasing the local chain dynamics.¹⁷⁹

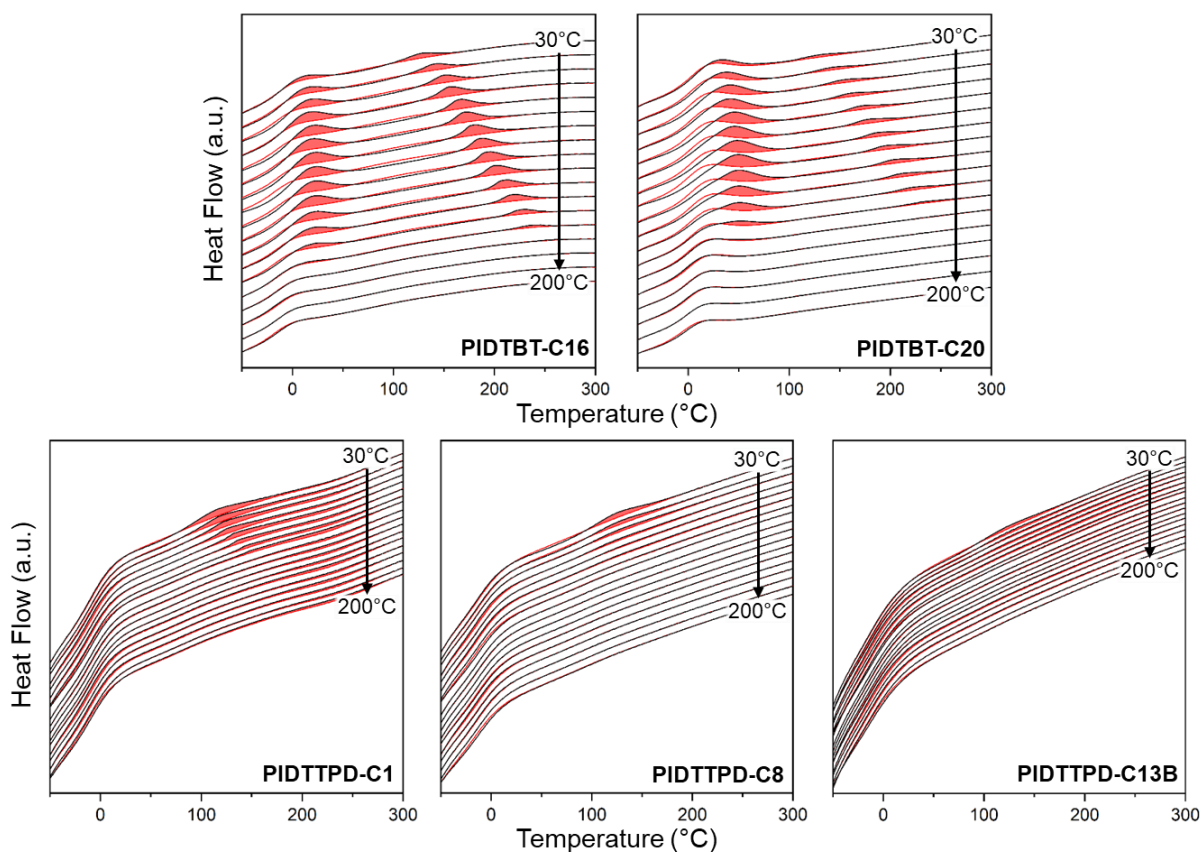


Figure 2.16 Annealing of Planar IDT Copolymers. Annealed and reference thermograms of PIDTBT copolymers with annealing temperatures listed on the right side in increments of 10 degrees. PIDTBT copolymers show side-chain softening and liquid-crystalline-like melting peaks with annealing, while PIDTTPD copolymer show weak endotherms indicate some liquid-crystalline-like ordering, but no side-chain softening peaks.

Annealing was also performed on this series of IDT polymer to examine the side-chain softening and liquid-crystalline-like phases. PIDTBT-C16 shows similar peaks to Figure 2.13 while PIDTBT-C20 shows a side-chain melting at slightly higher temperatures (~50 °C) which is consistent with the increased melting of linear alkanes. There are also liquid-

crystalline-like regions to the PIDTBT-C20 sample, occurring at similar temperatures as the C16, which indicates that the side-chains do not play a large role in this phase. If side-chains were ordered in this phase as well, then the entropic increase of longer side-chains would be expected to decrease the melting point. However, further studies on the molecular weights as necessary as melting endotherm peaks are potentially molecular weight dependent as seen in Figure 2.17. For the TPD series, there appears to be no apparent side-chain softening regions, and only very weak liquid-crystalline-like endotherms occurring 100-150 °C. This indicates that side-chain softening and liquid-crystalline ordering in IDT-based polymers is fragile and heavily dependent on chemical structure and planarity. The additional side-chains on the TPD units are expected to disrupt the side-chain ordered.

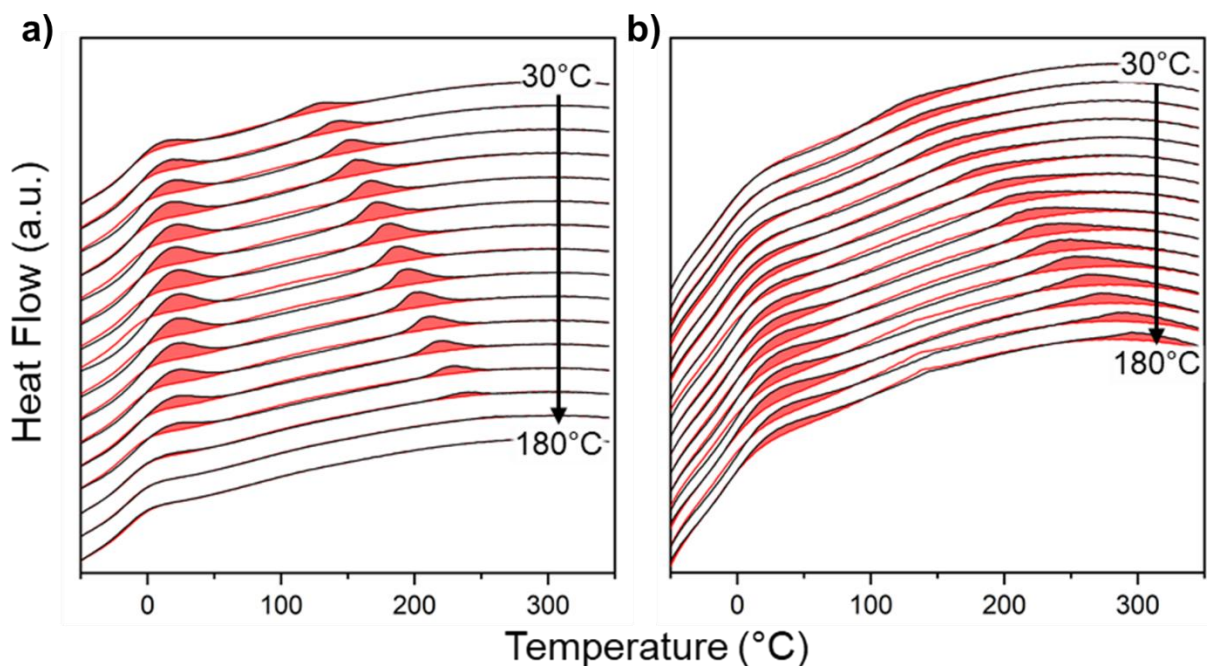


Figure 2.17 Molecular Weight Dependence of Liquid-Crystalline-Like Phase of PIDTBT. Annealed and reference curves of low molecular weight (left) and high molecular weight (right) PIDTBT-C16 both showing side-chain softening and liquid-crystalline-like melting peaks. Side-chain softening endotherms are molecular weight independent because both systems have 16 carbons. Liquid-crystalline-like endotherms appear at higher temperatures for high molecular weight PIDTBT indicating longer lamellar thickness which are possible with the longer backbone.

The liquid-crystalline-like region of IDT polymers requires further investigation to the mesoform: nematic or smectic. It also appears as though the peak temperature of the liquid-crystalline-like melting is dependent on molecular weight reminiscent of chain extended polymer crystals with longer polymers chains having higher melting temperatures.^{180–182} At least in these two samples, folding of these chains is not apparent, but more molecular weights are required for confirmation. Liquid-crystalline-like regions are expected to align with other microstructural features like the (001) peak in x-ray scattering, and optoelectronic features like hole mobilities of transistors. Therefore, thermal screening of these phases can qualitatively predict mechanical properties and device performance.

2.3.3 OECT Materials

Organic mixed ionic-electronic conducting (OMIEC) polymers are able to conduct electronic and ionic charges¹⁸³ with applications of OMIECs spanning bioelectronics,^{184,185} electrochromics^{186,187}, and energy storage.¹⁸⁸ In order to conduct electrons and ion, the material must go through electrochemical doping which is a dynamic process where large variations in microstructure, energetic landscape, volume, ion content, and charge carrier concentration are linked to the oxidation state of the polymer. Consequently, the choice of the backbone and solubilizing groups has profound impact on both the electrolyte affinity and π -orbital delocalization and inter-chain interactions.

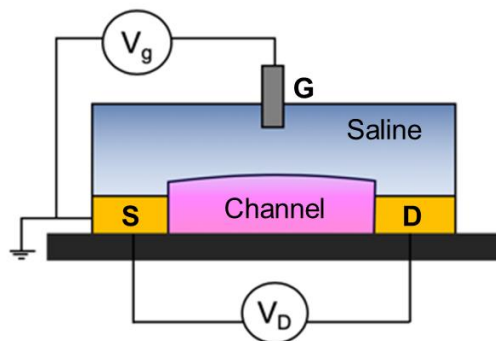


Figure 2.18 OECT Schematic. The channel is comprised of the conjugated polymer and a electrolyte solution (saline) is placed above with solvent and electrolyte able to penetrate the polymer film. Tuning gate voltage allows for ion penetration into the polymer and electronic conductivity across the channel.

Progress and advancements have been made due to establishing structure-property relationships of polymer OMIECs and building off of the knowledge from OPV and OFET materials.^{154,189} Synthetic changes include the addition of polar oligoether side-chains to common semiconducting thiophenes seen in photovoltaics and transistors.¹⁹⁰ Other relationships have been developed through blending with non-conjugated polymer electrolytes.^{191,192} The most common figure of merit in OECTs is the volumetric capacitance (product electronic mobility and volumetric charge storage) and transconductance (signal amplification)¹⁹³ which are performance markers during steady-state operation, however, there is not a standard metric for the transient behavior, *i.e.* switching kinetics, of OMIECS. This could be due to large number of confounding factors that affect the switching kinetics including the size and charge of the ions.¹⁹⁴ Additionally, a factor affecting switching kinetics includes the ionic conductivity and it is assumed to relate to either the Vogel-Fulcher-Tammann or Arrhenius relationship.^{195–197} These relationships have a dependence of the glass transition temperature and therefore understanding ionic conductivity in OMIECs has been limited by difficulty in measuring the glass transition temperature of conjugated polymers.

Here we present a series of poly(3,4-propylenedioxythiophene) (ProDOTs) with varying side chain lengths, polarities, and sterics. Extensive side-chain engineering of ProDOTs have led to knowledge on optoelectronic properties and local ordering however, in most cases thermal properties are not reported, so the relationship between these side-chains and T_g are unknown for ProDOTs.^{198–200}

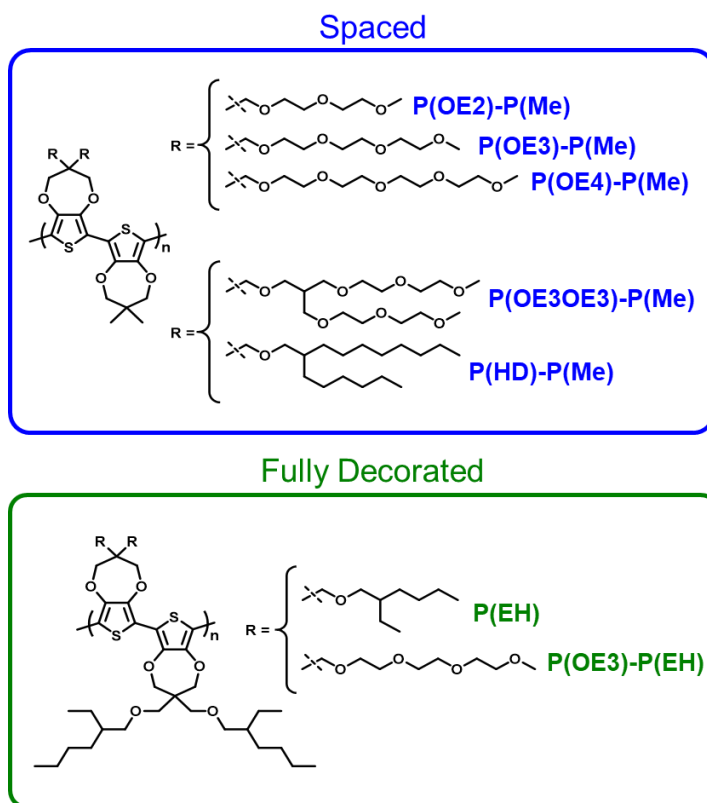


Figure 2.19 ProDOT Series Structures Investigated. ProDOTs of varying side-chain length, polarity, sterics, and substitution degrees are investigate to determine the influence of each on the glass transition temperature.

The propylene bridge causes slight decreases in planarity of ProDOT compared to PEDOT and it also places the side-chains more orthogonal to the backbone. Even though, crystallographic data is not available for the whole series of ProDOTs, others have shown that ProDOTs of varying side-chain chemistries have weak and broad GIWAXS signals indicating they are weakly ordered and highly amorphous.^{201–203} The absence of melting

peaks in calorimetric measurements also verify this claim. Therefore ionic conductivity is expected to not be dependent on transport into crystalline regions which has shown to decrease switching time by a factor of three.²⁰⁴

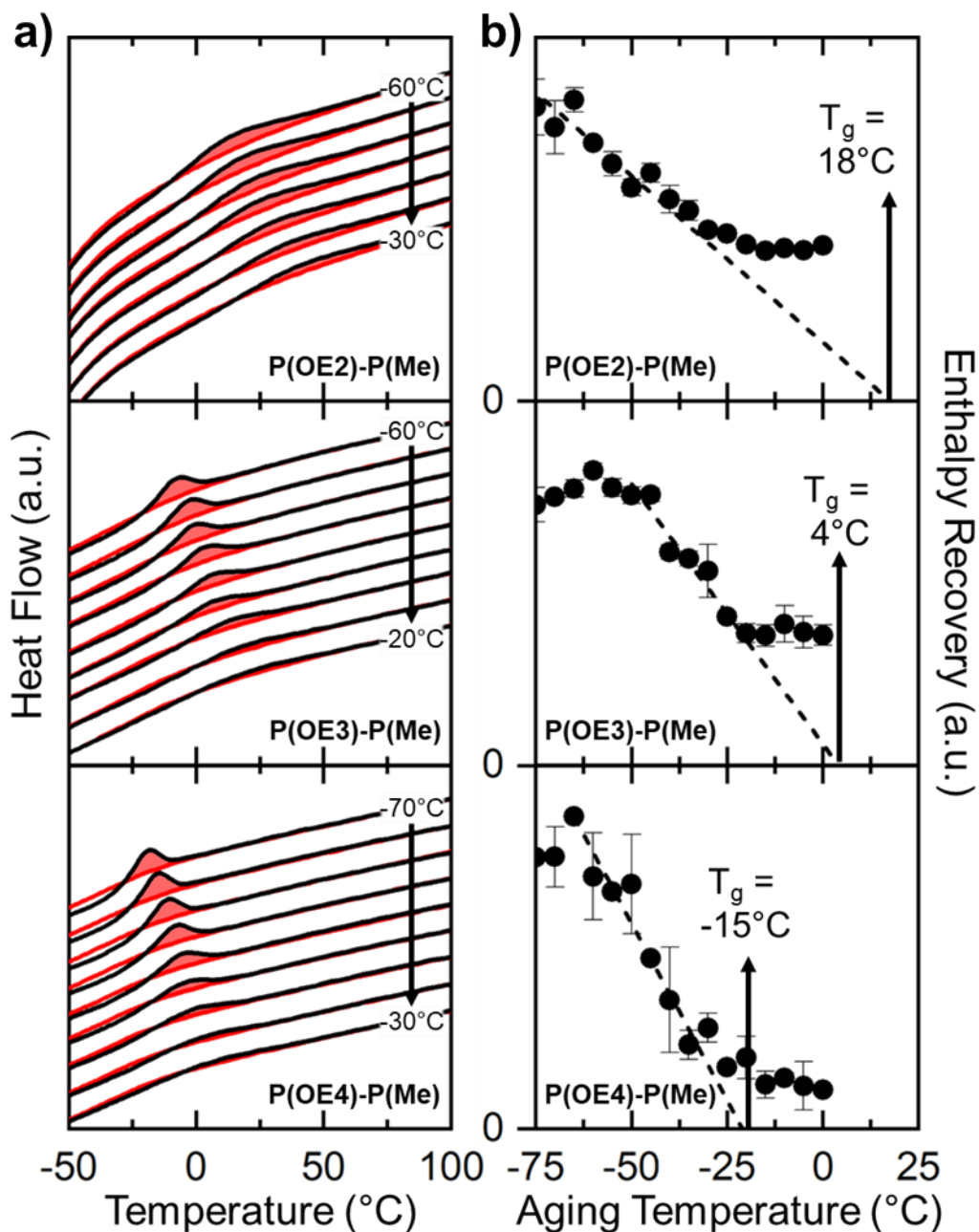


Figure 2.20 Physical Aging of Linear Spaced ProDOTs. Physical aging signatures (a) with aging temperature shown in increments of 5 degrees with extrapolated glass transition temperatures (b).

The first series of ProDOTs include the copolymers with linear oligoether side-chains on one repeat unit with dimethyl groups on the other. The decreased density of the dimethyl unit could decrease the free volume in the system and thus drastically increase the T_g .²⁰⁵ Sharp decreases in T_g are seen with increased side chain length, which tracks with trends seen in P3HT.²⁰⁶ Endothermic overshoots for P(OE2)-P(Me) and P(OE3)-P(Me) show slight evidence of separate processes occurring when aged near T_g evidenced by the overshoots tailing off. Side-chain organization is common in long linear side-chain semiconducting polymers with the temperature at which they appear being dependent on side-chain length and distribution.^{148,176} P(OE4)-P(Me) does not show a drastic tailing off because the T_g is far enough removed some potential side-chain organization temperatures. Other processes like a distribution of T_g s due to the low molecular weight and dispersity of P(OE2)-P(Me) and P(OE3)-P(Me) compared to P(OE4)-P(Me), seen in Table 2.1, may be a cause for these broad overshoots. Side-chain organization does cause mechanical differences separate from the influence of T_g , which can attribute to physical characteristics of swelling during electrochemical doping.

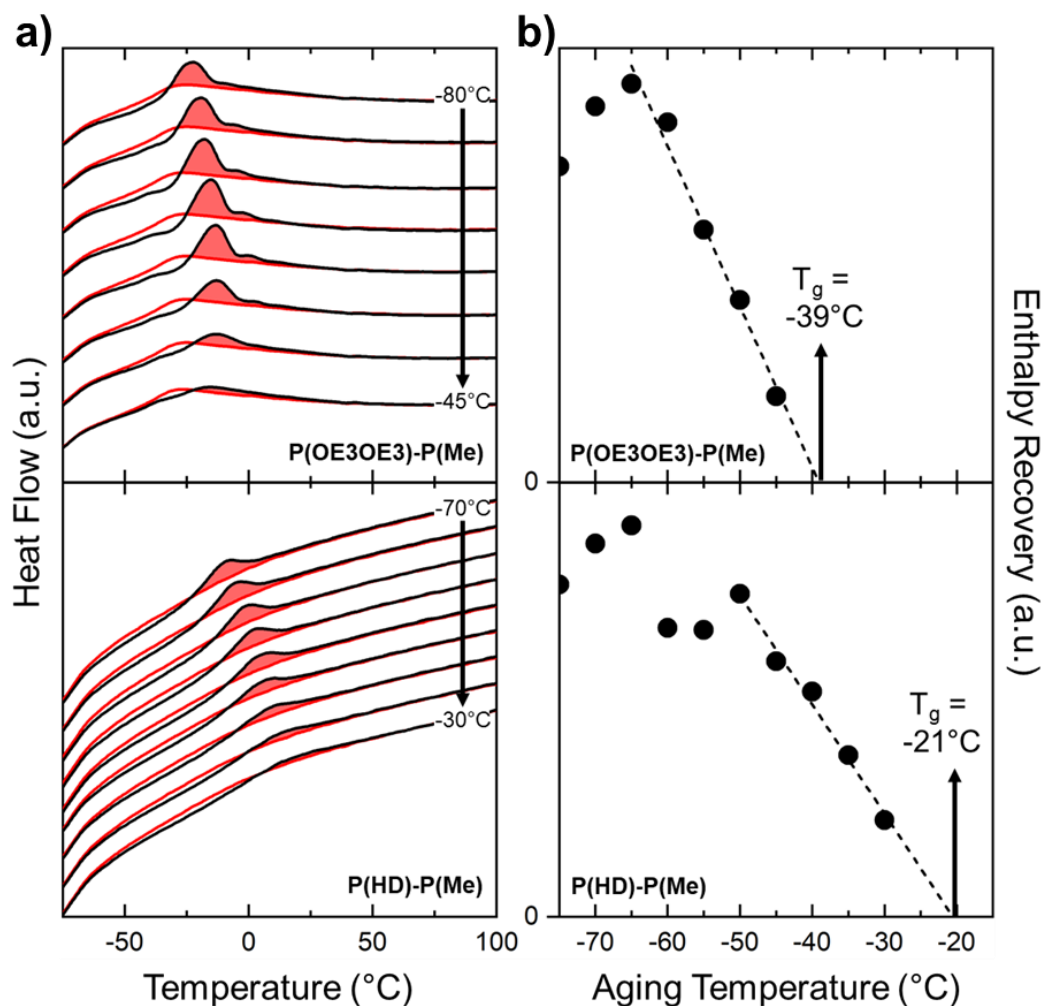


Figure 2.21 Physical Aging of Branched Spaced ProDOTs. Physical aging signatures (a) with aging temperature shown in increments of 5 degrees with extrapolated glass transition temperatures (b).

Branching within the side-chain is known increase T_g for the same number of atoms, so branched-spaced copolymers are examined as well.¹⁷⁹ The same, highly polar oligoether sidechains are added with a branching point. The total number of atoms is significantly increased therefore plummeting the T_g . No evidence of side-chain organization is evident in these samples, however, these features are expected to be much greater than -32°C .

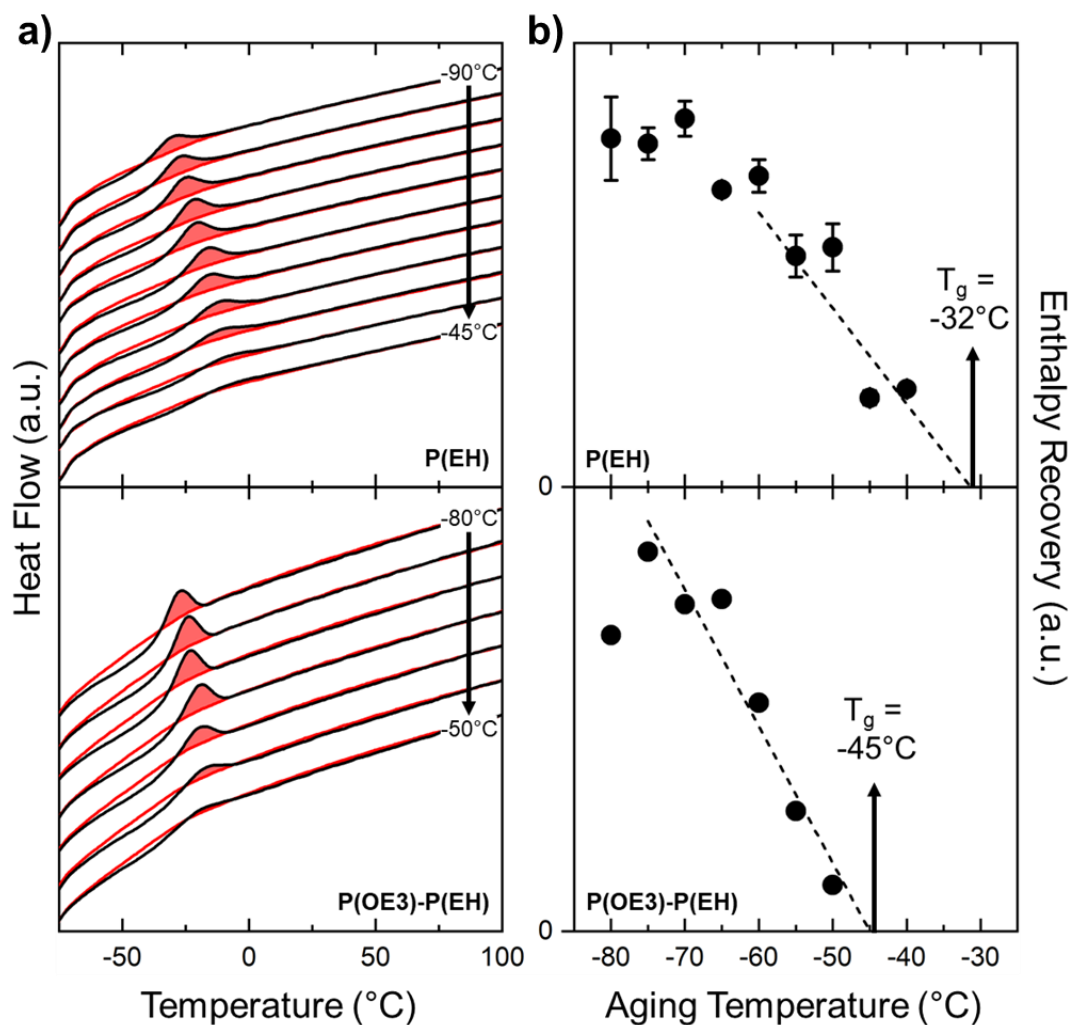


Figure 2.22 Physical Aging of Fully Decorated ProDOTs. Physical aging signatures (a) with aging temperature shown in increments of 5 degrees with extrapolated glass transition temperatures (b).

Fully decorated ProDOTs are examined to determine the influence of a more symmetric distribution of side-chains and no side-chain ordering phases are expected in these either.

Table 2.1 ProDOT Series Data Table. Molecular weight, dispersity, glass transition temperature, and number of side-chain atoms not including hydrogens for each ProDOT.

| Name | M _n (kg/mol) | Đ (-) | T _g (°C) | Side Chain Length (# of atoms) |
|-----------------|----------------------------|----------|------------------------|-----------------------------------|
| P(OE2)-P(Me) | 13 | 1.6 | 18 | 20 |
| P(OE3)-P(Me) | 23 | 2.0 | 4 | 26 |
| P(OE4)-P(Me) | 66 | 2.5 | -15 | 32 |
| P(HD)-P(Me) | 18 | 2.3 | -21 | 38 |
| P(EH) | 11 | 1.7 | -32 | 40 |
| P(OE3)-P(EH) | 37 | 1.6 | -45 | 44 |
| P(OE3OE3)-P(Me) | 15 | 1.3 | -39 | 46 |

Table 2.1 shows that all samples have a number-average molecular weight above 10 kg/mol, so the T_gs reported are not expected to be heavily dependent on molecular weight. Additionally, Table 2.1 shows the total number of side-chain atoms if all heteroatoms outside of the dioxythiophene unit and excluding hydrogens. The shortest side-chain ProDOT, P(OE2)-P(Me), has less than half the total number of side-chains of P(OE3OE3)-P(Me) and the large difference in T_gs show the influence that the side-chains have. The reported T_gs are expected to be effectively the upper bound of the T_g for each material, as the fast cooling rate of Flash DSC will increase the T_g²⁰⁷ and the physical aging experiments measure the T_{g,onset} upon cooling. Therefore future reports on T_gs of ProDOTs may show lower results. A simple relationship between the T_g and number of side-chain atoms in Figure 2.23.

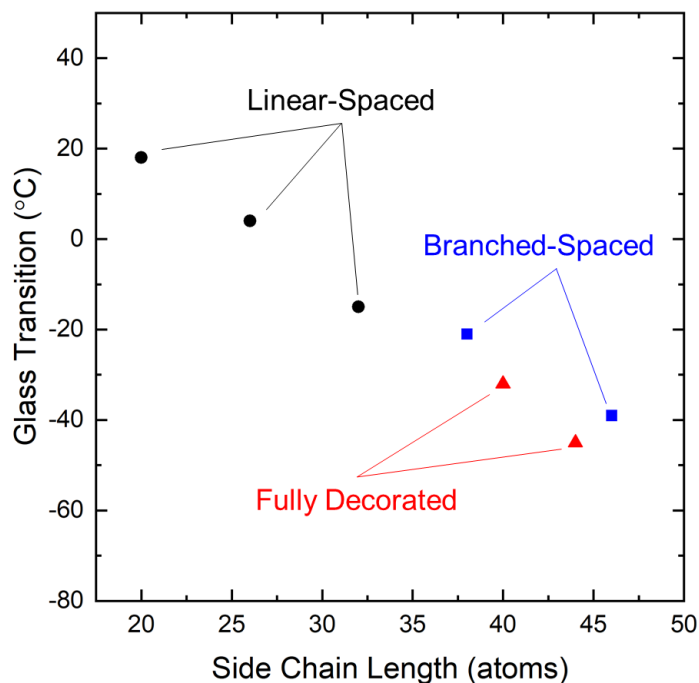


Figure 2.23 Relationship between the Glass Transition Temperature and Length of Side-Chain in ProDOTs. Linear spaced (black circles), branched-spaced (blue rectangles), and fully decorated (red triangles) ProDOTs are plotted with a mostly-linear trend between glass transition temperature and side-chain length appearing. No influence of polarity, substitution pattern, or branching effects are apparent.

The relationship between T_g and side chain length appears linear, with the substitution pattern, chemistry, and sterics being less dominant than the effect of additional atoms. This independence of T_g from side chain polarity and sterics is consistent with other predictions of T_g s for semiconducting polymers.¹⁵⁷ The polarity of the side-chains playing no role is significant in suggesting that the backbone is not plasticized more compared to nonpolar side-chains. The addition of polar side-chains is instead more influential on the solubility and miscibility with polar/aqueous solvents and electrolytes.

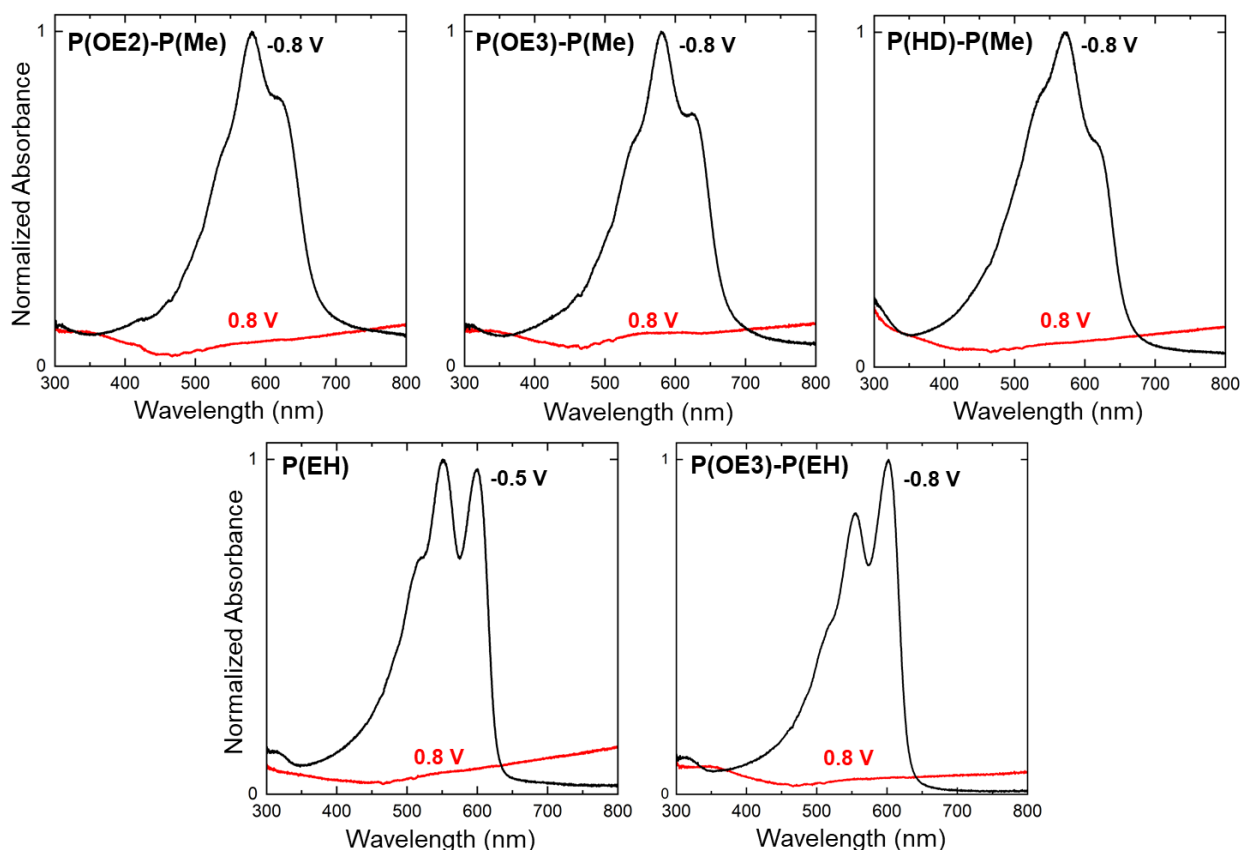


Figure 2.24 Normalized absorbance of fully reduced and fully oxidized ProDOTs. Fully reduced ProDOT (black lines) with voltage measured and fully oxidized ProDOT (red lines) with voltage measured. Each ProDOT exhibits the full removal of their vibronic absorptions with fully oxidized states being mostly transparent.

As switching kinetics and ionic conductivity in electrochemical devices are expected to be heavily dependent on T_g , i.e. segmental motion, this series provides us with a range of T_g s spanning over 60 °C. To measure the switching kinetics, we can look at the change in absorption as functions of applied voltage.

For the spectroelectrochemical characterization, the selected polymers were sprayed onto ITO/glass slides (Delta Technologies Ltd., 25 x 75 x 0.7 mm³, sheet resistance 8-12 Ω /sq, cleaned by sonication in toluene, acetone, and isopropanol) to the desired optical density from 4 mg/mL chloroform solutions using an Iwata Eclipse HP-BC airbrush with an optimized argon pressure of approximately 20 psi. The experiments were performed in a

three-electrode electrochemical cell consisting of a Ag/Ag⁺ pseudoreference electrode (E1/2 for Fc/Fc⁺: 0.075 V), and a Pt flag counter electrode. The electrolyte consisted of 0.5 tetrabutylammonium hexafluorophosphate (TBAPF₆) dissolved in propylene carbonate. All samples were electrochemically conditioned using cyclic voltammetry for 10 cycles at 50 mV/s from -0.8 V to 0.8 V. The in situ spectroscopic analyses were then performed with an Ocean Optics USB2000+ fiber-optic spectrophotometer in 1 cm path length quartz cuvettes. The potential was controlled with a PINE WaveNow potentiostat and AfterMath software. When recording steady-state spectra, the films were held at the desired potential for 20 seconds prior to recording the spectrum. The switching kinetics were probed by measuring the absorbance at λ_{max} as the film was switched between the dedoped and fully doped states using 10 second pulse lengths. Only 5 of the ProDOTs could be examined in electrochemical switching due to limited quantities of the polymer and solubility issues upon oxidation.

The ProDOT series all switch from a colored film to transparent during electrochemical oxidation. At the fully reduced state (-0.8 V), each ProDOT has a vibronic progression of absorption, seen in Figure 2.24, which indicates some intermolecular coupling and photophysical aggregates form.²⁰⁸ Without further temperature dependent photoluminescence measurements, the exact nature of the photophysical aggregates, i.e. H- or J-aggregates, and thus are considered mixed HJ-aggregate.²⁰⁹ The photophysical aggregates, however, are not expected to play a role in optical switching kinetics.

To measure the optical switching kinetics, each ProDOT sample is cycled between its fully reduced to fully oxidized state, and the peak absorption intensity is measured versus time. Figure 2.25 shows the time evolution for each of the ProDOTs. Doping for all samples

occur within 0.5 seconds, and dedoping for P(HD)-P(Me), P(EH), and P(OE3-EH) occur within 2 seconds. Samples that do not fully dedope within 2 seconds are expected to have other factors hindering the process and will be discussed later. A time constant to analyze multiple samples is utilized. This time constant is the reciprocal of the slope of the linear portion of the lines in Figure 2.25 and is analogous to time constants reported by Hassab *et al.*,²¹⁰ with the main difference being a measurement of the absorbance rather than the transmission. This leads to a change in time constants by a multiplier of about 300. Absorption is chosen rather than transmission as it more closely relates to the concentration of the ground state chromophores.

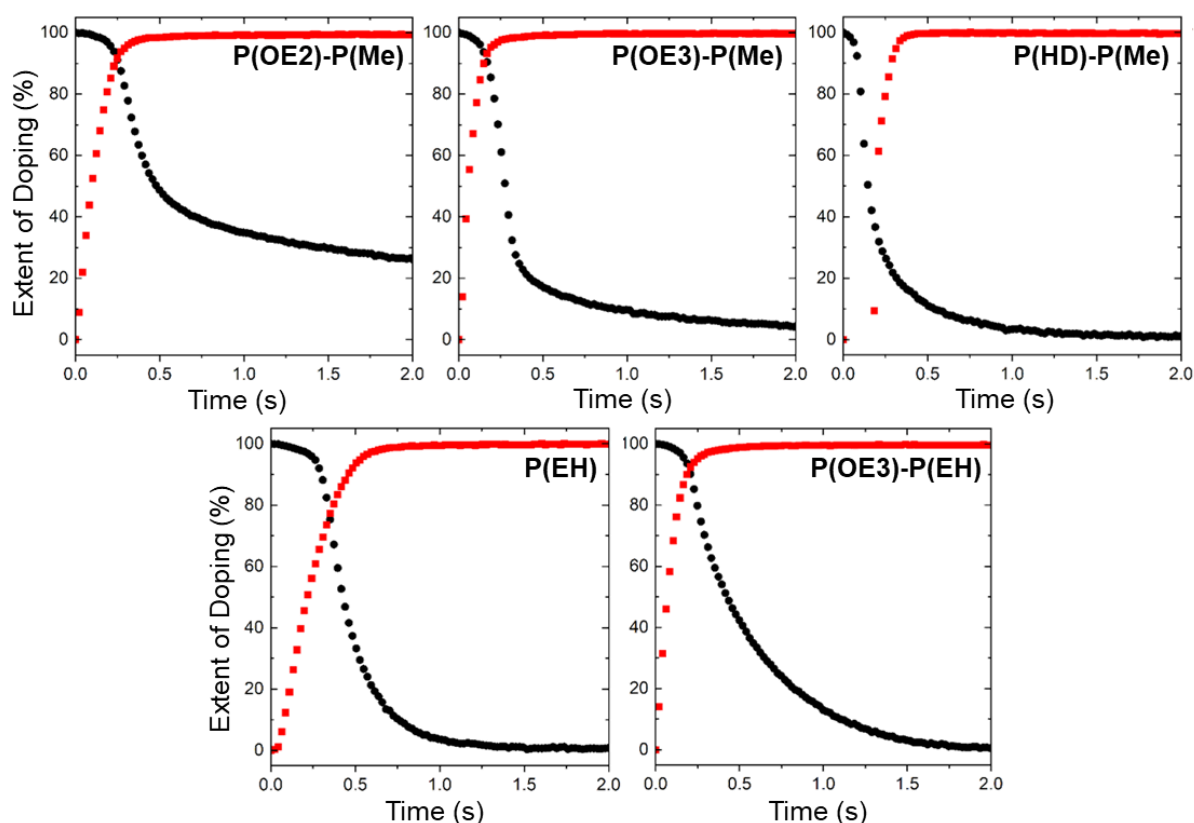


Figure 2.25 Electrochemical Doping and dedoping versus time of ProDOTs. Max absorbance wavelength of ProDOTs measured versus time after the applied voltage switch from fully reduced to fully oxidized state and vice versa. Red scatter points show the doping (oxidation) process and black points show the dedoping (reduction) process.

There is also a small slope portion in the short time range for most of the ProDOTs which were not consistent for each sample and each measurement and therefore likely due to sampling interval differences or other experimental artefacts. Each time constant is plotted versus their respective T_g in Figure 2.26. Doping time constants are about half as much as dedoping, which tracks with the total switching times. Interestingly, the T_g appears to have no effect on the doping or dedoping time constants in this ProDOT series, which means segmental motion is likely not a limiting factor.

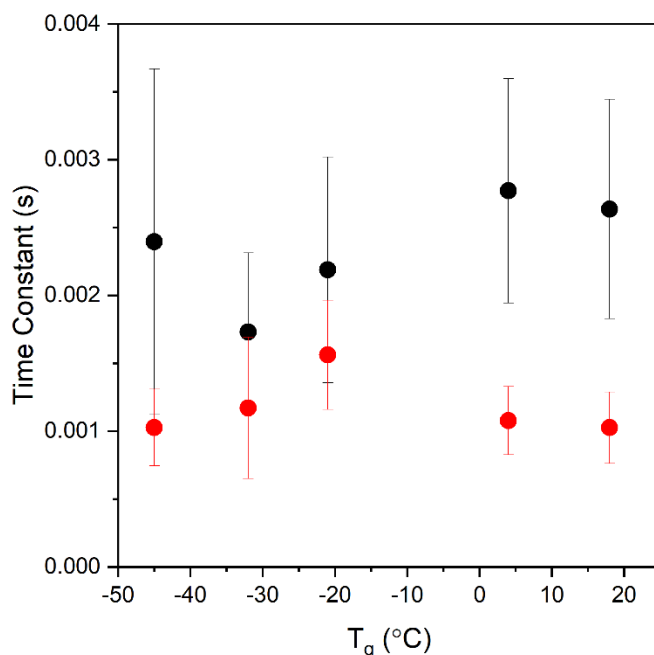


Figure 2.26 Time constants electrochemical doping and dedoping of ProDOTs. Time constants of doping (red) and dedoping (black) measured as the reciprocal of the slope of the linear portion of the absorbance change during doping and dedoping. There is no relation between electrochemical switching and glass transition temperatures.

The lack of dependence of electrochemical switching time and T_g can be due to a few different factors. Since each T_g is below room temperature, segmental motion happens rapidly for each polymer during the measurement. Additionally, swelling measurements show that each polymer passively and actively swells at least 10% upon exposure to solvent and oxidation. The increase of solvent can plasticize the polymer further, leading to a T_g

of the system being even lower than the neat polymer.²¹¹ Swelling measurements on P(OE2)-P(Me) were not possible, however, it is expected to swell similarly to P(OE3)-P(Me) which passively swells over 100%. The similarity in time constants with materials of drastically different T_g s infers that ion diffusion in these systems happens in the solvated-vehicle regime.^{183,212} Without temperature dependent measurements on each sample to verify the relationship with switching speed and temperature, it is difficult to conclusively state the regime of ion transport.

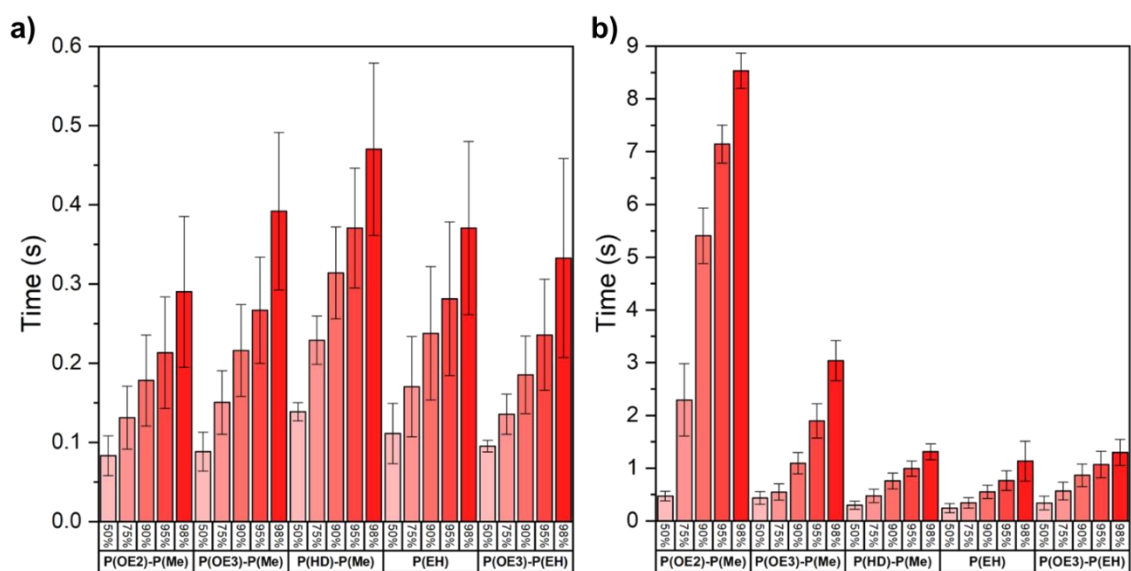


Figure 2.27 Electrochemical doping and dedoping completion times. Time it takes to complete 50, 75, 90, 95, 98% of the doping (a) and dedoping (b) process measured via normalized absorption changes as functions of time.

Another way to measure the electrochemical switching time is through the time it takes partially dope. Figure 2.27 shows the time it takes for 50, 75, 90, 95, and 98% of doping or dedoping to occur, with 100% doping and dedoping defined as the largest change in absorption. The doping process, similar to Figure 2.26, shows very fast doping of ProDOTs, with 98% doping occurring within 0.5 seconds for all materials. Additionally, at every stage measured, there is not changes in the time it takes between different

ProDOTs. This is consistent with the time constants of doping. The largest difference is seen in the dedoping of P(OE3)-P(Me) and P(OE2)-P(Me) which take over 3 and 8 seconds, respectively, to dedope. As mentioned prior, P(OE3)-P(Me) shows super-swelling characteristics, which can lead to mechanical breathing and then delamination from the electrode.²¹³ The same behavior is expected in P(OE2)-P(Me) given its similar chemical structure and with an even higher T_g ductility is likely reduced. Further experiments into the swelling nature of ProDOTs is being pursued in the group.

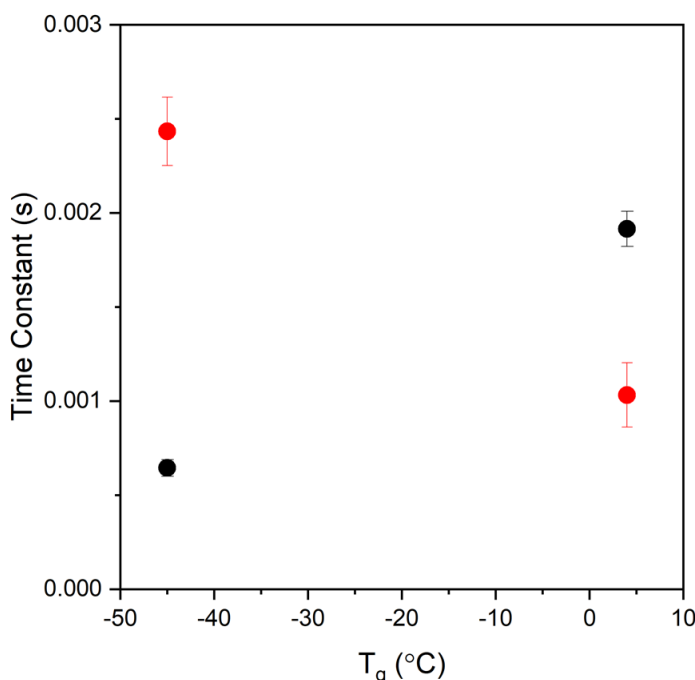


Figure 2.28 Time constants electrochemical doping and dedoping of ProDOTs in aqueous solution. Time constants of doping (red) and dedoping (black) measured as the reciprocal of the slope of the linear portion of the absorbance change during doping and dedoping. There is no relation between electrochemical switching and glass transition temperatures.

Even though previous electrochemical switching kinetics are measured with a nonpolar solvent, and there was a range of side-chain polarities scanned, the same measurements were performed with NaCl in water. Data on several different films with varying thickness was not available, however, time constants and doping times seen in Figure 2.26 and 2.28

appear on the same order of magnitude as nonpolar solvents. Both of these ProDOTs measured have large T_g differences, as well as differences in swelling, however still appear to switch in the same timeframe.

Aqueous measurements on switching speed hint that factors like intermolecular forces and ion size may not significantly affect the switching speeds of ProDOTs. This further implies that ion transport happens in the solvated vehicle regime, and highlights ProDOTs possessing extremely fast electrochemical kinetics.

2.3.4 Additional Side-Chain Effects

In Section 2.3.2, the role of side-chain ordering and its effect on optoelectronic and mechanical properties was discussed. With highly planar IDT copolymers, side-chain ordering played a particularly large role on the ductility of the material. There was also an increase in T_g when the side-chains on IDTBT were increased from 16 to 20 carbon atoms. This increase is primarily attributed to a large difference molecular weight, however, another factor may influence the T_g . Side-chains of increasingly large size have been shown to crystallize rapidly and thus increase the T_g of the backbone.²¹⁴

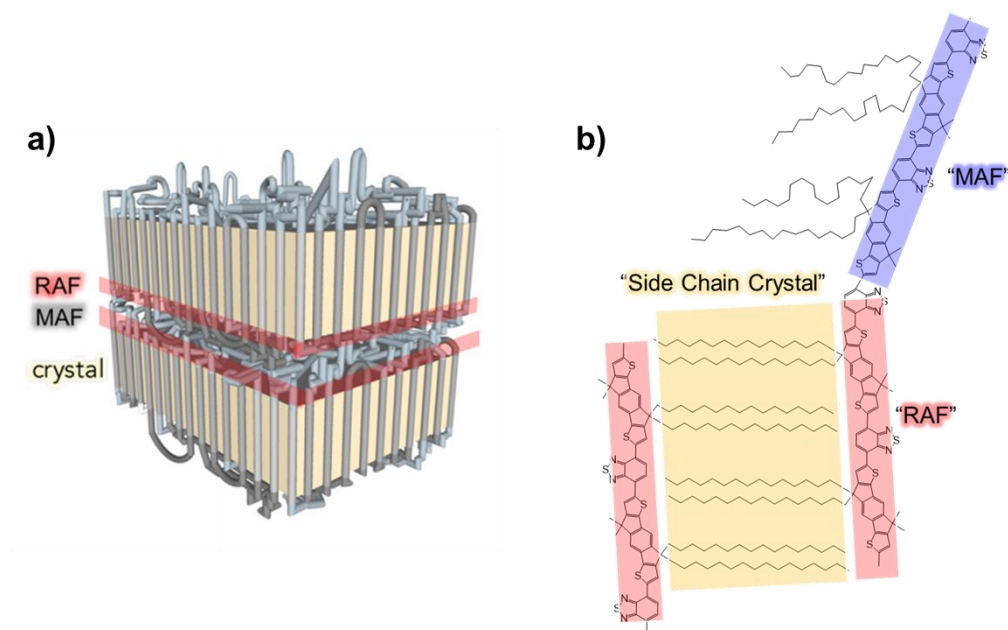


Figure 2.29 MAF and RAF Phases. (a) Traditional mobile amorphous fraction (MAF) and rigid amorphous fraction (RAF) phases right highlighted in blue and red, respectively. Crystal phase indicates the backbone crystals. (b) Proposed “MAF” and “RAF” phases as consequences of side-chain crystals in hairy-rod polymers.

This minimum in T_g as functions as linear side-chain length has been reported in polymers with varying backbones,^{215,216} however the presence of a minimum and subsequent increase in T_g with side-chain length deviates from the entropic increase that side-chains impose on backbones. There are reports of dual glass transitions appearing in long side-chain poly(alkyl itaconates) with each glass transition having similar activation energies indicative of major relaxation processes, i.e. cooperative motion.^{217,218} Additionally, there is a reported increase in glass transition temperature as a function of side-chain crystallization.²¹⁹ Thus prior reports of the increase in glass transition with side-chain length are expected to be artefacts of the measurement technique with side-chain softening and glass transitions have similar and overlapping signals.²²⁰ The dual glass transitions is more reminiscent of the mobile amorphous fraction (MAF) and rigid amorphous fraction (RAF) phases of semicrystalline polymers. Since the MAF and RAF phases were not

proposed until 1985,²²¹ and most of these reports predate this, what was reported could likely be RAF phase T_g s.

The participating atoms in this MAF and RAF phases differ from the conventional backbone crystals. Figure 2.29 shows the pictograms of conventional MAF and RAF phases, along with the newly proposed MAF and RAF phases as a consequence of side-chain crystallization. The new RAF phase consists of the backbone atoms that contain the side-chain atoms participating in the crystallization, however, these backbone atoms are not expected to contribute to the side-chain crystal and therefore are denoted as the RAF. The new MAF phases, is the amorphous backbone phase which has side-chains that do not participate in side-chain crystallization and is expected to have the same T_g as the fully amorphous material.

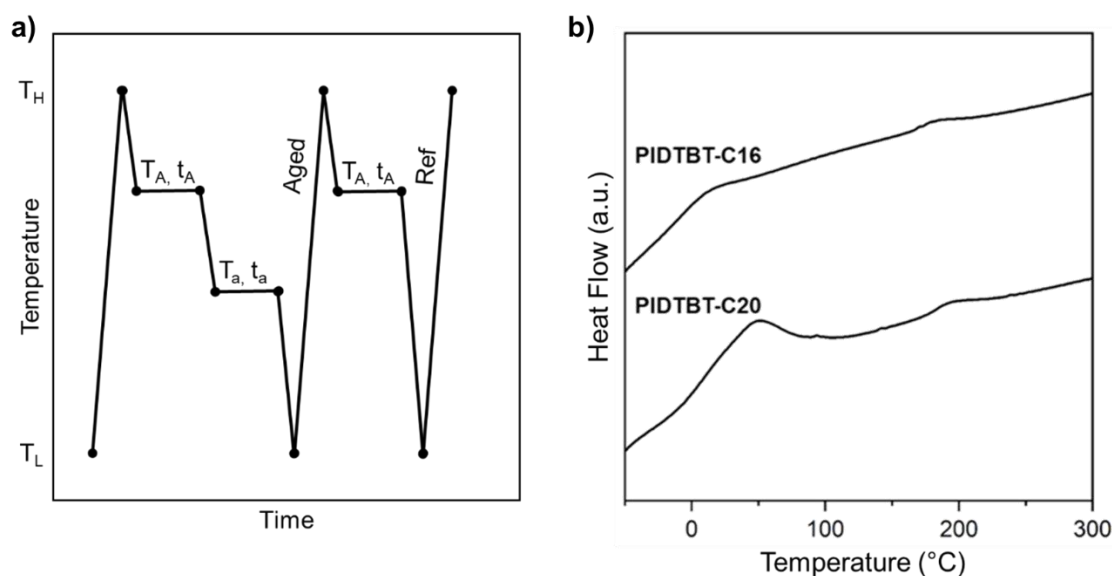


Figure 2.30 Annealing and Aging Protocol for Side-chain crystal ordering. (left) Flash DSC annealing and aging protocol in create side-chain crystals and then age below the glass transition temperature (right) Flash DSC reference curves from annealing protocol. PIDTBT-C16 and -C20 both show side-chain softening endotherms and liquid-crystalline-like melting endotherms

In order to induce side-chain crystallization and thus the MAF and RAF, an annealing step is taken prior to aging. This annealing process has been shown to create traditional MAF and RAF phases in poly(l-lactic acid).²²² Figure 2.30 shows the new thermal experiment as well as the reference curves for both PIDTBT-C16 and -C20 which show side-chain softening peaks and liquid-crystalline-like backbone melting peaks.

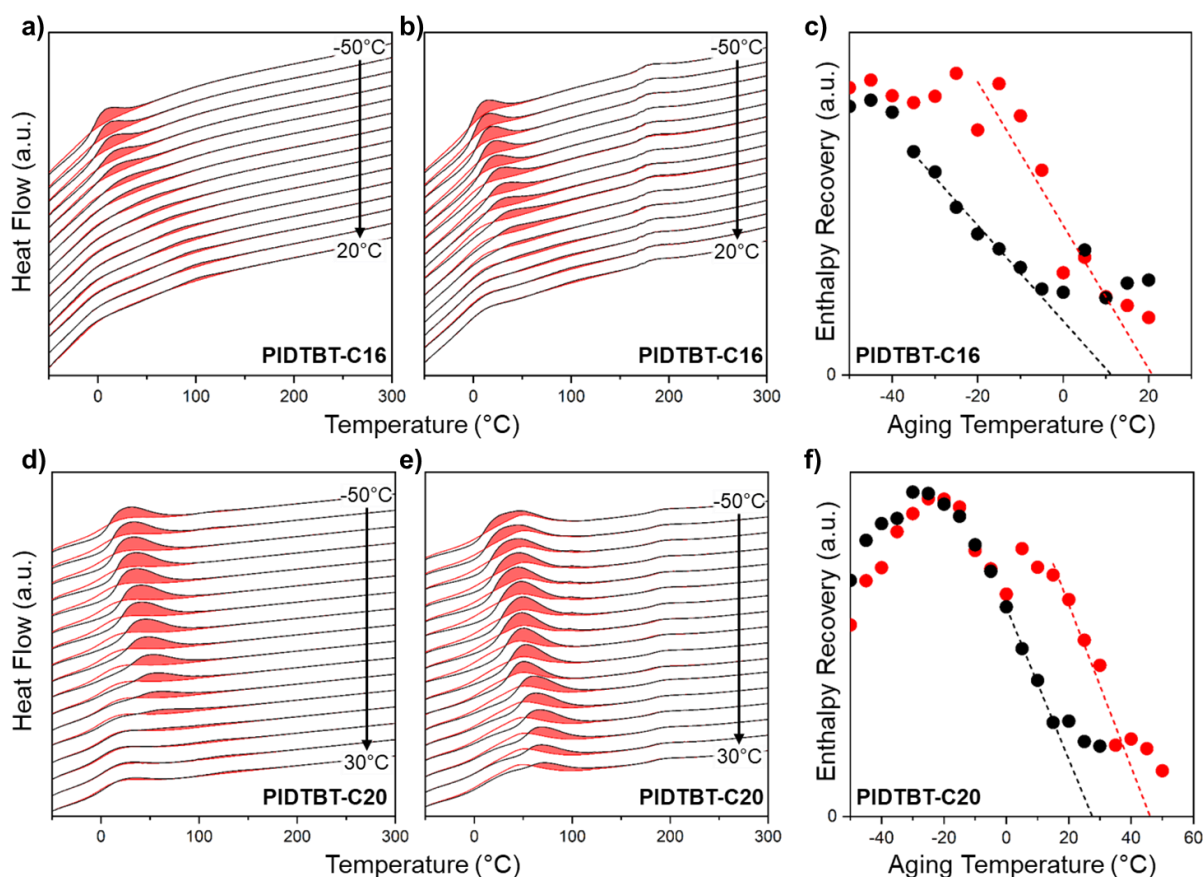


Figure 2.31 MAF and RAF Evidence in PIDBT. (a) Physical aging curves of non-annealed PIDTBT-C16 samples that will have mostly amorphous phase. (b) Physical aging curves of annealed PIDTBT-C16 samples that have side-chain crystals prior to aging. (c) Enthalpic recoveries of the aged (black) and annealed and aged (red) samples with linear extrapolations of the glass transition temperatures for the MAF and RAF phases. (d) Physical aging curves of non-annealed PIDTBT-C20 samples that will have mostly amorphous phase. (e) Physical aging curves of annealed PIDTBT-C20 samples that have side-chain crystals prior to aging. (f) Enthalpic recoveries of the aged (black) and annealed and aged (red) samples with linear extrapolations of the glass transition temperatures for the MAF and RAF phases.

Physical aging is measurements for a large range of temperatures just like in previous protocols and the enthalpic recovery can be used to estimate the T_g s of the polymers. Figure 2.31 shows the resulting thermograms of the polymers aged (Figure 2.31a and 2.31d) and annealed and aged (Figure 2.31b and 2.31e). In both polymers, the annealed and aged samples show additional endotherm overshoots at high aging temperatures. The enthalpy recovery graphs also show the extrapolation of T_g for the aged sample and annealed and aged sample. The annealed sample, which has side-chain organization, shows extrapolated T_g s that are approximately equal to the peak temperature for the side-chain softening endotherm. Additionally, in PIDTBT-C20, the annealed enthalpic recovery appears to have two decreasing ranges, the first of which is between aging temperatures of -15 and 0 °C which, if extrapolated aligns with the aged sample. The dual extrapolations possible with PIDTBT-C20 is like that of P3HT MAF and RAF phases.²²³ Dual extrapolations in PIDBT-C16 are difficult, however, the increased enthalpic recovery of the annealed sample compared to the aged sample indicates there is a larger driving force towards the equilibrium glass which means that the T_g would be higher. Finally, the RAF T_g for these systems is expected to align with side-chain softening, because once the side-chains are no longer ordered, there is nothing hindering the backbone from cooperative motion. The new ‘critical length’ of a side-chain that causes an increase in T_g is actually a critical length of the preferred kinetics and thermodynamics of side-chains forming crystals in the time-scale of the experiment. If the material can be fully vitrified, then no critical length will exist. The mechanical implications of these new MAF and RAF phases are likely insignificant because the side-chain crystals are already hindering cooperative motion. This is the first

known report of MAF and RAF phases through side-chain crystallization of conjugated polymers.

2.4 Crystallization and Vitrification Kinetics

In addition to physical aging to measure the T_g of polymers, the Flash DSC's rapid heating and cooling opens avenues to explore crystallization kinetics of fast-crystallizing polymers. Because crystallization involves transformation from a liquid to the solid state and it has profound effects on melting temperature, residual stress, shape distortion and mechanical properties, polymer crystallization is essential in polymer powder-bed based 3d printing. Polyamide 12 or PA12 is a commodity plastic used in many industries for packaging as well as insulating and chemical resistant tubing. It is also very common in powder-bed based additive manufacturing. The mechanical and thermal properties are dependent on, among other things, the crystallinity of the polymer. PA12 crystallinity can range from 25-50% and the size of the crystals affects the properties as well.²²⁴ During crystallization, PA12 can shrink in volume causing potential issues during processing. Thus it is important to understand the extent and kinetics of crystallization.

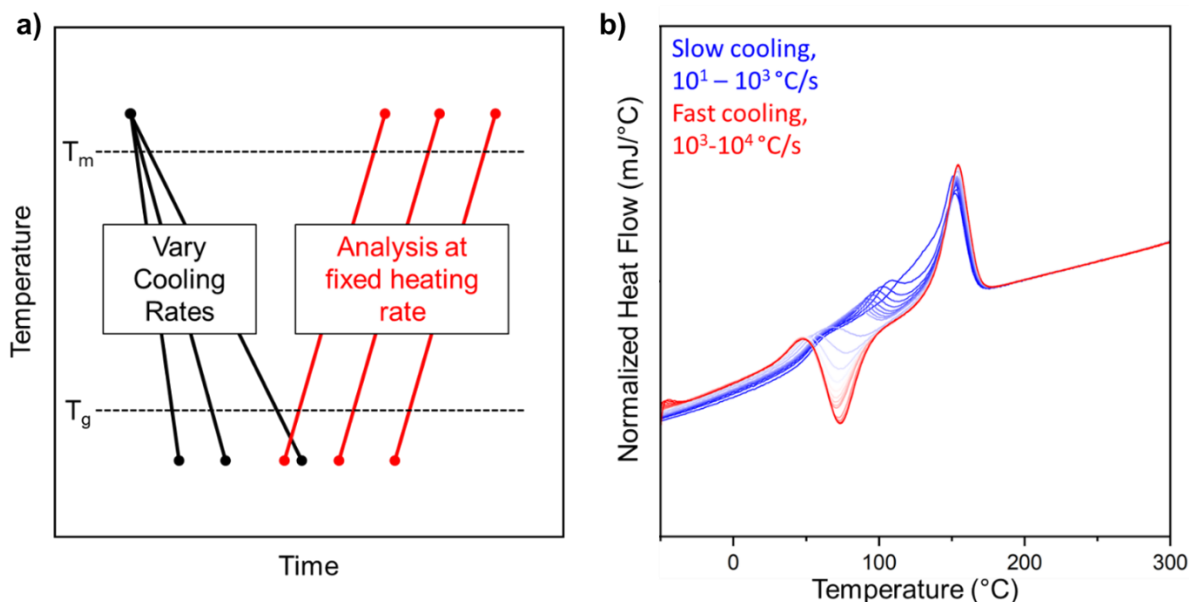


Figure 2.32 Vitrification Kinetics Protocol of PA12. (a) Flash DSC temperature vs time protocol to measure the cooling rate at which no crystals are formed. (b) Heating thermograms at 1000 °C/s of PA12 immediately following a varied cooling rate between 10 and 10^4 °C/s.

One method to measure crystallization kinetics is with the Avrami equation which estimates crystalline shape during isothermal and non-isothermal crystallization conditions.^{225–227} However, the sample must be quenched prior to isothermal crystallization so a minimum rate needs to be calculated.

PA12 crystallizes extremely quickly due to its linear, flexible backbone and hydrogen bonding units, which makes crystallization kinetics studies difficult using conventional differential scanning calorimetry. Thus, fast scanning calorimetry, using a Mettler Toledo Flash DSC 1, is required for more accurate determination of the crystallization kinetics and potentially identify effects of nucleation. Figure 2.3.2a shows the heating traces performed in fast scanning calorimetry to help identify critical cooling rates. Cooling rates as chosen in a logarithmic pattern, while heating rate is maintained constant. Then the process is repeated several times for several different heating rates. In this case, heating rates between

500 and 5000 °C/s are chosen. Figure 2.3.2b shows the resulting heating curves at 1000 °C/s after cooling rates varying from 10 to 10,000 °C/s. At very slow cooling rates, a strong melting peak is seen upon heating. Then as cooling rates increase, the melting peak area decrease slightly and a cold-crystallization exotherm appears and grows with cooling rate. Faster cooling rates will quench the PA12 leading to fewer crystals. The enthalpy of fusion for each cooling rate minus the cold crystallization enthalpy will tell us how many crystals are present in the sample at a given cooling rate. This relationship is shown in red in Figure 2.33. Additionally, the cold crystallization enthalpy as a function of cooling and heating rate is measured. A straight baseline is drawn between the endset of the glass transition temperature and melt phase to calculate the areas.

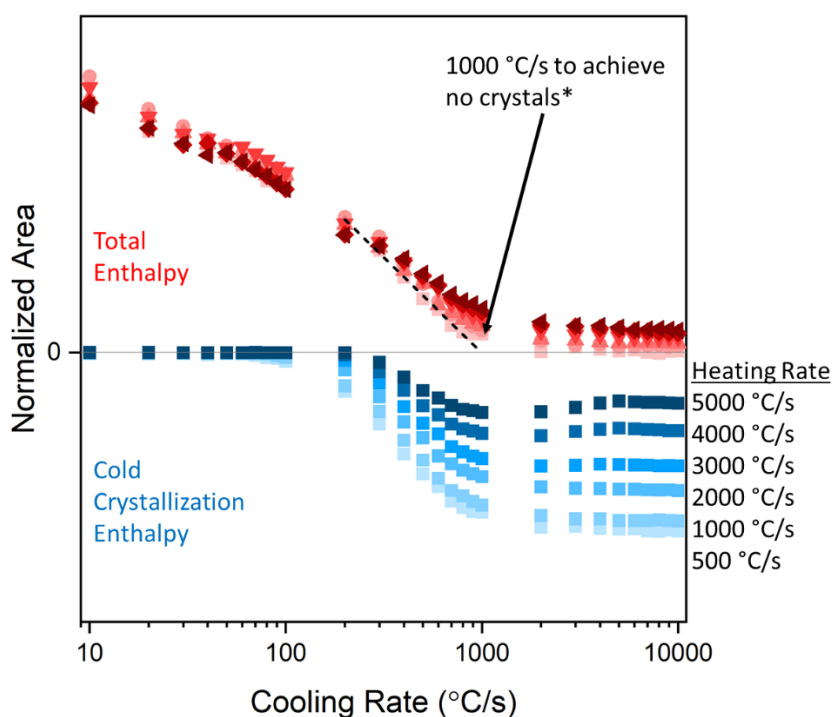


Figure 2.33 Vitrification Kinetics of PA12. Total enthalpy change (red symbols) as functions of cooling and heating rates. Linear extrapolation to zero enthalpy indicates the rate, ~1000 °C/s, at which no crystals form during cooling. Cold crystallization enthalpies (blue) as functions of cooling and heating rates. Larger magnitudes of cold crystallization enthalpies indicate formation of PA12 nuclei that form crystals upon heating.

The total enthalpy change between the cooled sample and an baseline will collapse to zero at the critical cooling rate for vitrification. This critical cooling rate is seen in Figure 2.33 and extrapolated to approximately 1000 °C/s using the heating rate data at 500 °C/s since faster heating rates show a small drift due to baselines not being as flat. This vitrification rate should be independent of heating rate so only one extrapolation is necessary. Additionally, at 100 °C/s there is an increase in the absolute value of the cold crystallization enthalpy which indicates nuclei formation that have not had enough time to crystallize. Even though the sample cooled at 1000 °C/s and higher can be thought of as amorphous, there are still nuclei present which only detected upon heating. As heating rate increases, there is a decrease in cold crystallization enthalpy because the process is time-dependent and faster heating rates decrease the overall time for crystallization. There is a heating rate fast enough that cold-crystallization will not occur even with nuclei present. The heating and cooling rates achievable in the Flash DSC 1 are not sufficient to completely eliminate nucleation and therefore cold crystallization peaks remain in all heating rates that follow a cooling rate of 100 °C/s and faster. Now that a critical cooling rate to crystal-free PA12 sample is determined, isothermal crystallization steps can be performed. The chosen cooling rate is 4000 °C/s as it is much faster than the critical cooling rate, but not too fast to cause nonlinear cooling in the Flash DSC. Figure 2.34a shows the isothermal crystallization protocol where the isotherms are varied in 5 °C increments and held up to 1000 seconds.

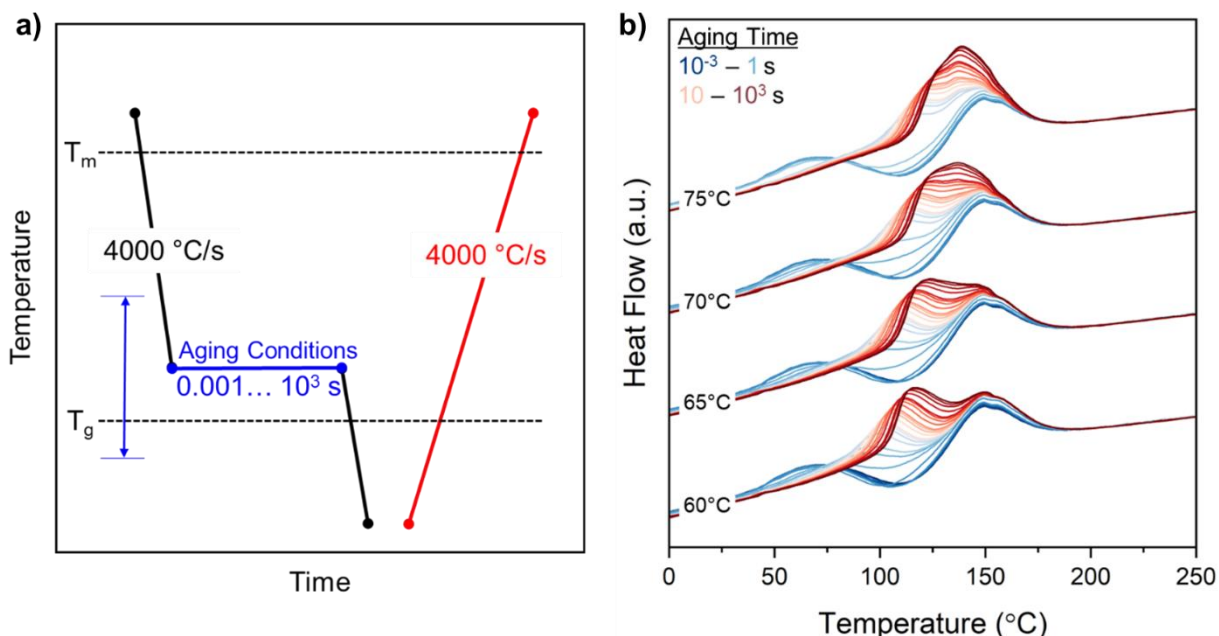


Figure 2.34 Isothermal Aging Protocol of PA12. (a) Flash DSC temperature vs time protocol to measure isothermal conversion kinetics. (b) Example thermograms of PA12 aged at temperature indicated on the left side for times indicated by color.

The growth of these nuclei and subsequent crystals are examined isothermally using the heating traces shown in Figure 2.34b. The isothermal holds vary in time logarithmically from 0.001 sec to 1000 seconds and the temperature is varied from 0 °C to 160 °C which covers ranges slightly below the glass transition to slightly below the melting temperature. The range will cover almost all nucleation and crystallization regimes of the polymer as it cannot crystallize far below the glass transition and above the equilibrium melting. Figure 2.34b shows the heating curves that follow the isotherms, with the temperature of the isotherm indicated on the left side of the lines and the time held indicated by the transition from blue to red. Changes in the exo- and endotherms are seen both as functions of temperature and time. The resulting enthalpy changes of the total system and cold crystallization are calculated in the same procedure as mentioned prior, and some temperature scans are shown in Figure 2.35.

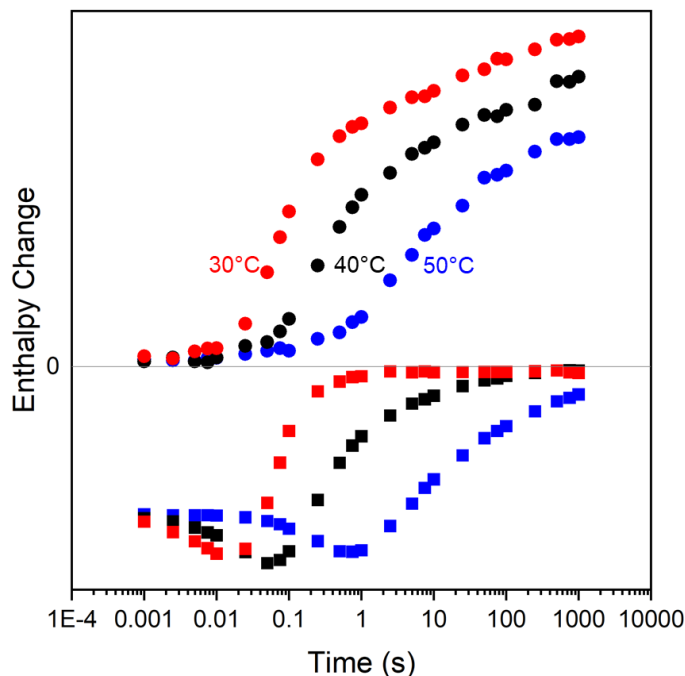


Figure 2.35 Crystallization and Nucleation of PA12. Enthalpy changes as functions of temperature and time, positive changes in enthalpy are indicative of crystallization, while negative changes are indicative of nucleation. Extrapolated lines from the fastest linear growth range indicate onset of crystallization.

Similar trends are found in each isotherm. The first of which is the total enthalpy change remains small and close to zero at very short times indicating an induction time is required before crystallization commences. Then crystallization occurs evidenced by the growth in total enthalpy of the system. Finally, the crystallization slows down as the polymer reaches its maximum crystal volume. The cold crystallization enthalpies remain constant at first because nucleation cannot be suppressed fully in this material. However there is a slight growth in the absolute value of cold crystallization enthalpies which highlights the maximum nuclei present. Finally, as crystallization starts, the amount of nuclei will slowly taper off. The most important process for this work is the start of crystallization which is linearly extrapolated to zero from the initial increase of the total enthalpy change and this time is labeled the characteristic time of crystallization. This times also aligns with the peak

nuclei production in the system because it marks the crossover from nucleation to crystallization. Since the cooling rate of 4000 °C/s does not suppress nucleation, a time of nucleation onset is not accessible, but is shorter than 0.001 seconds. If nucleation can also be suppressed, then the enthalpy change at extremely short times will be due to physical aging if below the T_g .

The characteristic times of crystallization are plotted versus their temperature in Figure 2.36. Heterogeneous and homogenous crystallization arcs appear at low and high degrees of supercooling, respectively.²²⁸ Heterogenous crystallization occurs from nucleation sites not intrinsic to the material, like dust, surfaces, and nucleating agents, while homogeneous crystallization occurs from the natural temperature fluctuations within the sample.^{228–230} Homogenous crystallization for PA12 occurs on time scales faster than 1 second for all temperatures. Even heterogenous crystallization generally occurs on time scales under 2 minutes, which is still relatively short compared to the time scales during 3D printing.

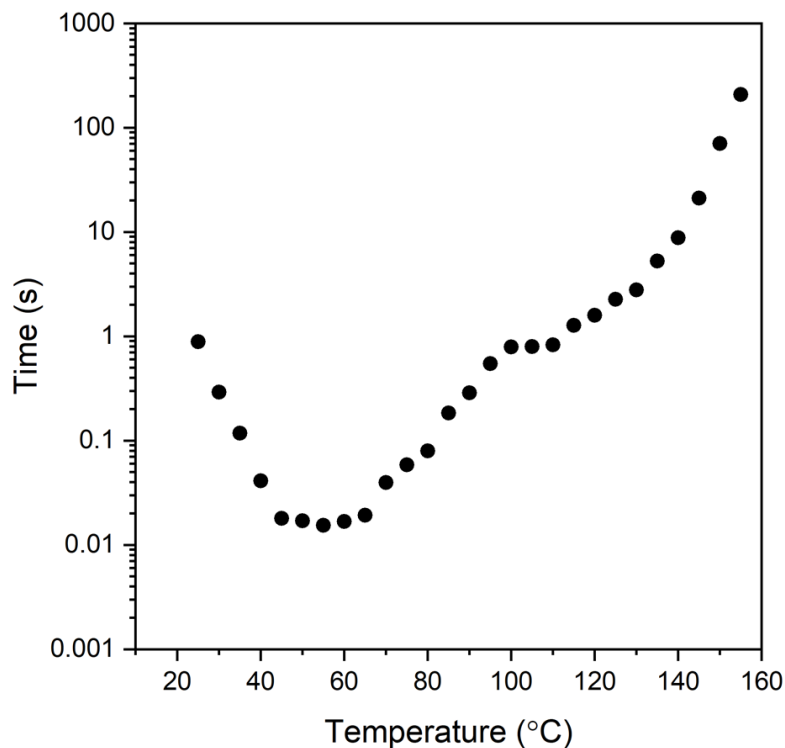


Figure 2.36 Characteristic Time of Crystallization of PA12. Points indicate the induction time at a given temperature required for crystallization to start. Heterogeneous and homogeneous crystallization arcs are seen at low and high degrees of supercooling, respectively.

These extremely short time scales highlight why fast scanning calorimetry is required for the most accurate results. The axes of Figure 2.36 can even be inverted to create a time-temperature-transition (TTT) diagram for this PA12 sample. The TTT diagram is a highly useful curve during processing to help identify expected phases within the polymer. With crystallization times and regions identified, the isothermal kinetics can be extended in the future to modeled kinetics. Additionally, the TTT diagram will be highly useful in modeling the stress and strain experienced during crystallization of the 3D printed PA12.

2.5 Future Work and Conclusions

2.5.1 Future Work: Phase Kinetics

In some cases, evidenced by the work on PA12, careful selection heating and cooling rates in fast scanning calorimetry is required. Effects like nucleation and crystallization may not be fully suppressed even at the fast cooling rates. Therefore, phase separation in blended systems can occur during the measurement due to crystallization of one of the phases. An example of this is in a blended system of P3HT and PVDF. Solution processing a 75:25 P3HT:PVDF blend allows for compatibilization and kinetic trapping of a blend in a non-equilibrium state. The two polymers show good intermixing with large cold-crystallization endotherms in DSC upon heating.²³¹ Thus they likely exhibit an intermixed-amorphous phase and the glass transition of this amorphous phase can attribute to other optoelectronic features like temperature-dependent photoluminescence. To investigate this intermixed phase, we looked at the system in Flash DSC. Figure 2.37 shows the physical aging signatures of the 75 wt% P3HT blend. Even though there appears to be a good enthalpic overshoot signal at low aging temperatures, there is also a large endotherm in both the aged and reference samples at ~140 °C which is the melting peak of PVDF. Even though the samples are quenched at 4000 °C/s, the presence of the PVDF melting show that crystallization still occurs, and crystallization is generally accompanied by phase separation. Therefore the same intermixed-amorphous phase produced from solution processing has not been retained. As aging temperature reach the glass transition temperature of P3HT (~25 °C),²²³ two endotherms start to appear in the aged curve. These are assigned to PVDF crystal growth and P3HT crystallization at the low and high

temperatures, respectively. With crystallization of both components occurring, there is likely even more drastic phase separation.

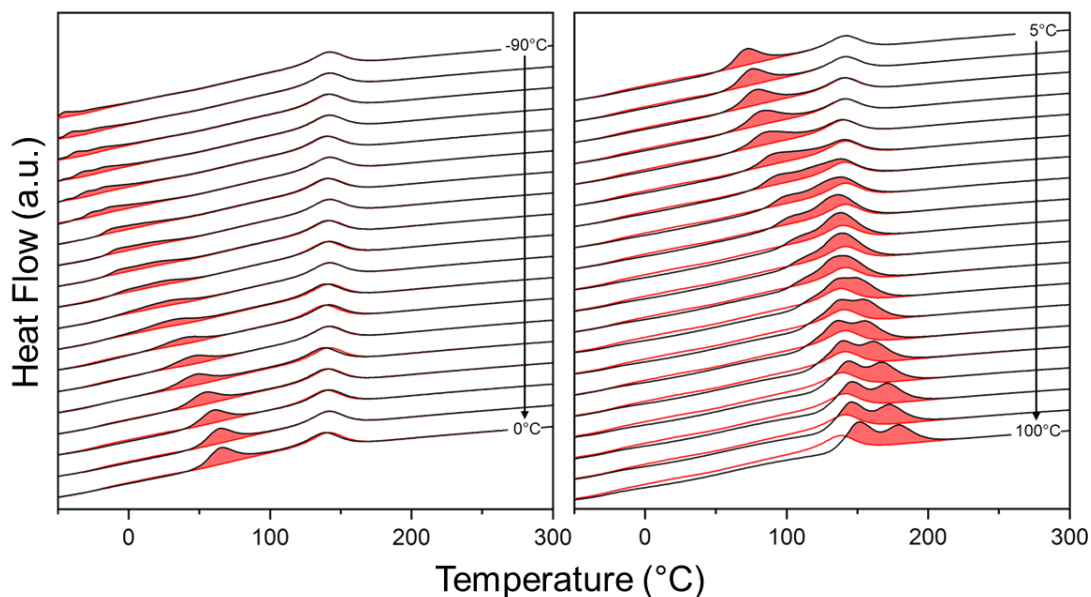


Figure 2.37 Physical Aging Signature of P3HT:PVDF 75:25 Blend (left) Low temperature aging range of blend exhibiting endotherm growth of characteristic of approaching the glass transition (right) Intermediate temperature aging range of blend showing a transition from physical aging to crystal growth

Further studies on the crystallization and vitrification kinetics of both P3HT and PVDF are required before analyzing the intermixed phase. Likely, the P3HT will crystallize slower than the PVDF as evidence by the absence of a P3HT melting peak until sufficiently high aging temperatures are reached. Fast cooling rates and long aging times of PVDF have shown to affect the different crystal phases of PVDF including the α - and β -phases.^{232,233} Experiments like those in Section 2.4 are suggested and generating temperature-time-transition curve for the PVDF will be required prior to physical aging measurements.

With the groundwork laid out to analyze crystallization kinetics using the Flash DSC, it can be expanded to conjugated polymers. This would complement the knowledge of the glass transition temperature, as that helps identify effective annealing temperatures, this

kinetics study can help identify annealing times required. In addition to process parameters, the crystallization kinetics of conjugated polymers can be expanded to modified Avrami equations that describe the directionality of the crystal growth.^{225–227} Finally, the crystallization kinetics of conjugated polymers under the influence of nucleated agents is of interest. Nucleating agents will affect the heterogeneous nucleation and can lead to an increased nucleation density and decreased crystal size and distribution.²³⁴ When combined with P3HT, nucleating agents improved the stability of the charge carrier mobility compared to neat P3HT and is attributed to the stabilized solid-state morphology.²³⁵ Nucleating agents for fullerene acceptors have also been shown to promote thermal stability in blended systems.²³⁶ Thus knowledge of the nucleation and crystallization rate of conjugated polymers and electron acceptors is advantageous in device processing.

The last aspect of phase kinetics that can be explored using the Flash DSC is melting kinetics. Similar to crystallization kinetics, this process analyzes the temperatures and times required to achieve full melting of polymer crystals. As polymers are heated, it is well known that their melting temperature will depend on the microstructure and heating rate. Chain-extending crystals will exhibit a superheated melting temperature, while chain-folded crystals can experience reorganization upon heating.²³⁷ The Flash DSC's large scanning rate time scales allow for in-depth analysis of the heating rate dependence of melting, which can then confirm heating rates at which no reorganization occurs.²³⁸ It is also possible to calculate the activation energy associated with detaching a crystalline stem which is dependent on the chain folding.²³⁹ Studies on chain-extending P3HT and chain-folded P3HT can provide further insight into the crystal microstructure.

Then the experiments could be extended to hairy-rod polymers to see if they behave like chain-extended crystals or something entirely different.

2.5.2 Future Work: Liquid Crystalline Hairy-rod Polymers

Several hairy-rod polymers were investigated for their glass transitions and side-chain ordering. However, like seen in PIDTBT, they also exhibit a high temperature liquid-crystalline-like melting. This liquid-crystalline is a main contributor to the increase performance of these polymers especially in OFETs. However, next-generation OPV materials include polymer like PM6 which have rigid backbones with some weak long-range ordering. These materials can be expected to exhibit liquid-crystallinity as well, and therefore knowledge of how to thermally induce the ordering would be advantageous for processing. With the ability to vitrify or order hairy-rod polymers in the Flash DSC, it can be combined with polarized microscopy and x-ray techniques to analyze the phase behavior and whether the backbone or side-chains participate in these liquid crystals.

2.5.3 Conclusions

The Flash DSC 1 has commercialized fast scanning calorimetry and as a result has opened the door to many experimental techniques and information on polymers. With this, phase information like the glass transition of conjugated polymers is now accessible. During the processing of conjugated polymers, annealing steps generally take place both to remove residual solvent and improve crystal structure. Now with knowledge of the glass transition temperature, more deliberate annealing temperatures and times can be utilized. Additionally, tracking the glass transitions of several conjugated polymers allows for empirical relationships between T_g and chemical structures to supplement other structure-property relationships.

In this thesis, we explored conjugated polymers for OPVs, OFETs, and OECTs, and the factors that affect thermal stability, mechanical ductility, and segmental motion. The glass transition temperature is a large contributor to each of these processes, but more importantly we looked at how the side-chains affect the T_g and these other processes. In OPVs, with the presence of UV-light, the side-chains have the ability to crosslink and therefore quench the PL intensity. Even if the glass transition temperature of the backbone is sufficiently high, the side-chains are still mobile and therefore affect device performance. In OFETs and hairy-rod polymers, the high rigidity of the backbone combined with long, linear side-chains can form local ordering of the side-chains known as side-chain crystals or side-chain ordering. These side-chain crystals will decrease the mechanical ductility of the overall material as it hinders segmental motion of the backbone even above the T_g . Additionally, the formation of the side-chain crystals is sensitive to several factors. Torsional rotation of the backbone and addition of fullerene derivatives that intercalate with the side-chains will disrupt the side-chain ordering. In OECTs, the side-chains are responsible for the solvent and electrolyte miscibility and therefore contribute to ionic mobility. In a series of ProDOTs, we found that the side-chain length is the primary contributor to backbone plasticization and that branching and polarity effects are negligible. With the wide range of T_g s accessible, we compared the electrochemical switching time with T_g and found no relation between the two. At least for ProDOT-based devices, the ionic mobility appears to not be limited by the segmental motion of the backbone. The switching kinetics of OECTs may be controlled by several factors including T_g , volumetric swelling, crystallinity, and more. Overall, the side-chains of conjugated polymers may not participate in the electronic processes of devices, however they heavily

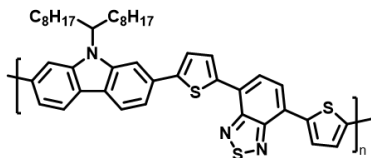
influence local ordering, thermal stability, and mechanical properties and careful design of the side-chains is critical in next-generation polymers.

In addition to measuring the glass transition temperatures and side-chain ordering of conjugated polymers, we also utilized the Flash DSC 1 to analyze crystallization kinetics. The fast cooling rates allow for a new method of measuring the crystallization kinetics of polymers instead of the half-time of crystallization measured in conventional DSC. The rapid cooling allows for vitrification to occur and then the characteristic crystallization times can be decoupled into homogeneous and heterogeneous nucleation. Rapid cooling rates also allows for more precise replication of thermal histories in 3D printed or melt-quenched polymers as they experience fast cooling rates as well. The extension of the crystallization times to a TTT diagrams also allows for easy prediction of the phases after a given thermal history.

In conclusion, fast scanning calorimetry has helped analyze the glass transitions and other low-resolution thermal transitions of conjugated polymers. This now accessible information will greatly supplement their structure-property relations and aid in the development of next generation conjugated polymers. Additionally, the fast heating and cooling rates allows for the formation of several different macroconformations of polymers and analysis of the kinetics of each phase. The field of polymer physics can greatly benefit from these new measurements and techniques.

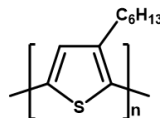
2.6 Appendix

2.6.1 Appendix A: Chemical Structures



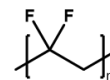
PCDTBT

poly[N-9'-heptadecanyl-2,7-carbazole-alt-5,5'-(4',7'-di-2-thienyl-2',1',3'-benzothiadiazole)]



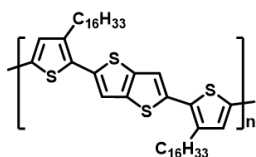
P3HT

poly(3-hexylthiophene-2,5-diyl)



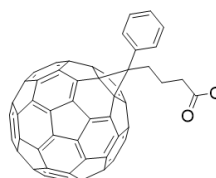
PVDF

poly(vinylidene fluoride)



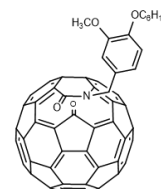
PBTTC-C16

poly[2,5-bis(3-hexadecylthiophen-2-yl)thieno[3,2-b]thiophene]



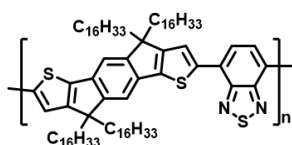
PCBM

[6,6]-Phenyl-C61-butyric acid methyl ester



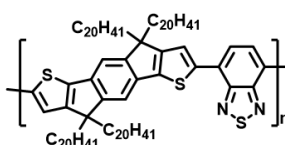
Keto

Ketolactam



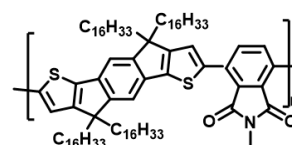
PIDTBT(-C16)

poly(indacenodithiophene-benzothiadiazole)



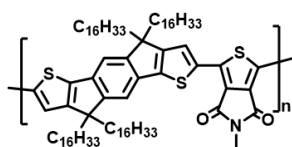
PIDTBT-C20

poly(indacenodithiophene-benzothiadiazole)



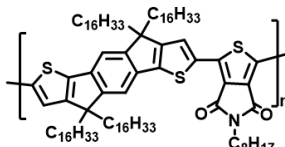
PIDTBPD

poly(indacenodithiophene-benzopyrrolodione)



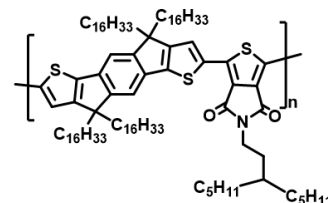
PIDTTPD-C1

poly(indacenodithiophene-thienopyrrolodione)



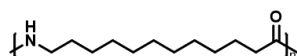
PIDTTPD-C8

poly(indacenodithiophene-thienopyrrolodione)



PIDTTPD-C13B

poly(indacenodithiophene-thienopyrrolodione)

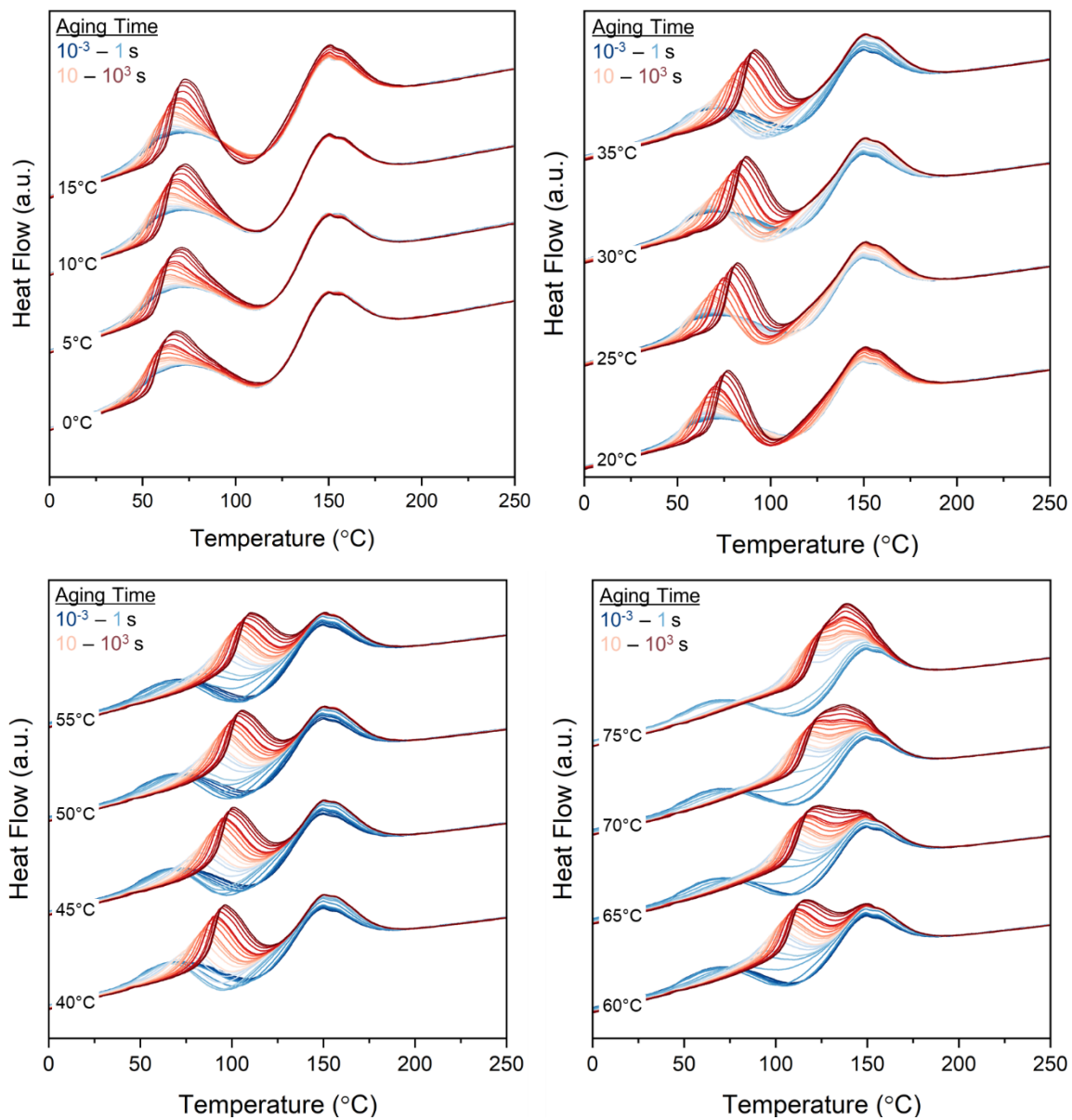


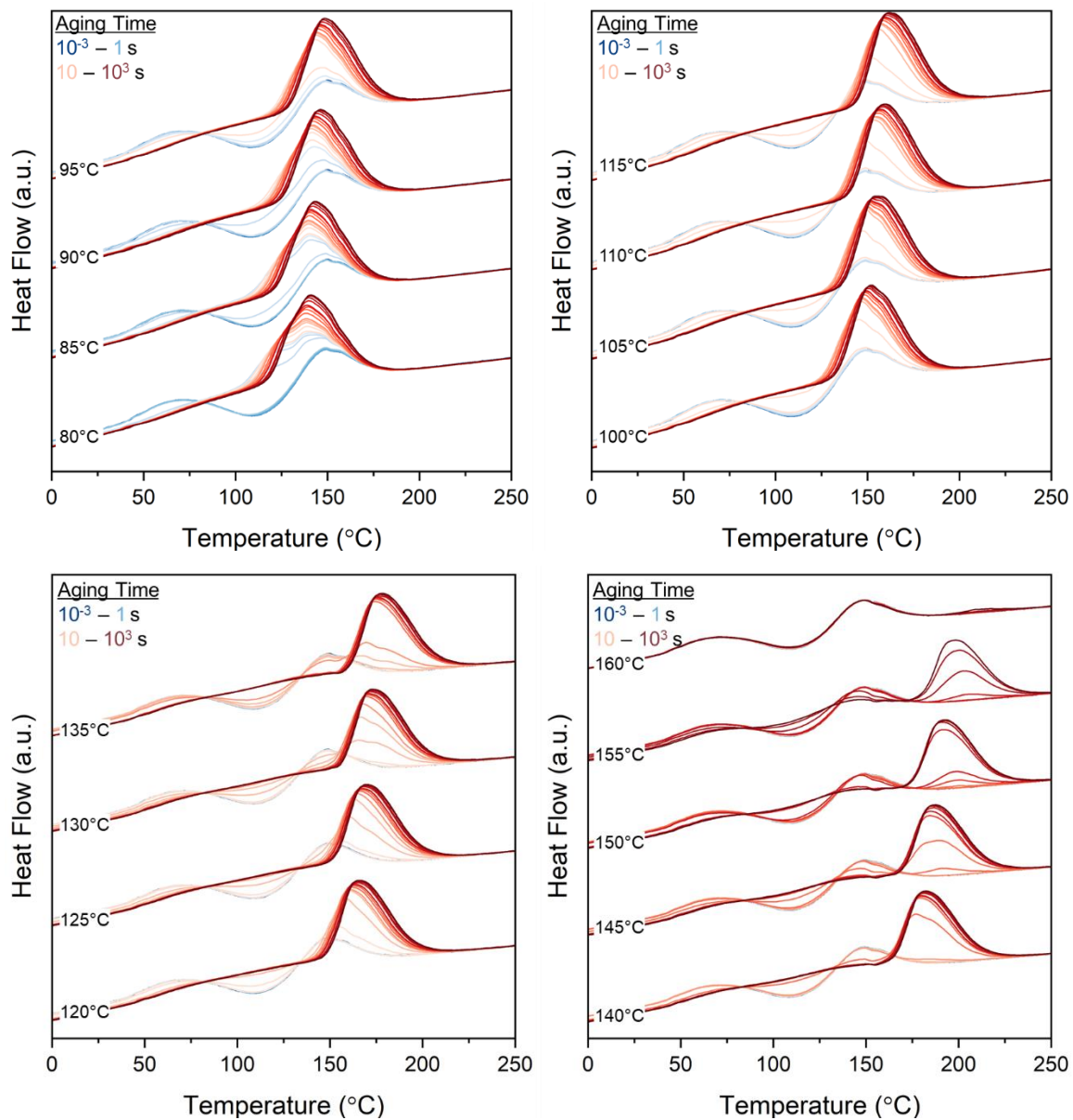
PA12, Nylon 12

Polyamide 12, poly(dodecano-12-lactam)

2.6.2 Appendix B: PA12 Supplemental Graphs

The following graphs are the full series of isotherms for the PA12 characteristic times of crystallization. The total area changes are plotted and extrapolated to zero like in Figure 2.35 to get the data points for Figure 2.36. Aging times are indicating from the transition from dark blue to dark red and annealing times are listed for each set of thermograms on the left side. Plotting all heating curves clearly shows the transitions from enthalpic relaxation, nucleation, and crystallization as low temperature endotherms, cold-crystallization endotherms, and high temperature endotherms, respectively.





3 References

- (1) Geyer, R.; Jambeck, J. R.; Law, K. L. Production, Use, and Fate of All Plastics Ever Made. *Science Advances* **2017**, 3 (7). <https://doi.org/10.1126/sciadv.1700782>.
- (2) Harmon, J. P. Polymers for Optical Fibers and Waveguides: An Overview. *ACS Symposium Series* **2001**, 795, 1–23. <https://doi.org/10.1021/bk-2001-0795.ch001>.
- (3) Ma, H.; Jen, A. K. Y.; Dalton, L. R. Polymer-Based Optical Waveguides: Materials, Processing, and Devices. *Advanced Materials* **2002**, 14 (19), 1339–1365. [https://doi.org/10.1002/1521-4095\(20021002\)14:19<1339::AID-ADMA1339>3.0.CO;2-O](https://doi.org/10.1002/1521-4095(20021002)14:19<1339::AID-ADMA1339>3.0.CO;2-O).
- (4) Liu, J. G.; Ueda, M. High Refractive Index Polymers: Fundamental Research and Practical Applications. *Journal of Materials Chemistry* **2009**, 19 (47), 8907–8919. <https://doi.org/10.1039/B909690F>.
- (5) Lorentz, H. A. Ueber Die Beziehung Zwischen Der Fortpflanzungsgeschwindigkeit Des Lichtes Und Der Körperdichte. *Ann Phys* **1880**, 245 (4), 641–665. <https://doi.org/10.1002/ANDP.18802450406>.
- (6) Lorenz, L. Ueber Die Refraktionsconstante. *Ann Phys* **1880**, 247 (9), 70–103. <https://doi.org/10.1002/ANDP.18802470905>.
- (7) Yang, C. J.; Jenekhe, S. A. Group Contribution to Molar Refraction and Refractive Index of Conjugated Polymers. *Chemistry of Materials* **2002**, 7 (7), 1276–1285. <https://doi.org/10.1021/CM00055A002>.
- (8) Olshavsky, M. A.; Allcock, H. R. Polyphosphazenes with High Refractive Indices: Synthesis, Characterization, and Optical Properties. *Macromolecules* **1995**, 28 (18), 6188–6197. <https://doi.org/10.1021/ma00122a028>.
- (9) Olshavsky, M.; Allcock, H. R. Polyphosphazenes with High Refractive Indices: Optical Dispersion and Molar Refractivity. *Macromolecules* **1997**, 30 (14), 4179–4183. <https://doi.org/10.1021/ma961628q>.
- (10) Fushimi, T.; Allcock, H. R. Cyclotriphosphazenes with Sulfur-Containing Side Groups: Refractive Index and Optical Dispersion. *Dalton Transactions* **2009**, No. 14, 2477–2481. <https://doi.org/10.1039/b819826h>.
- (11) Caseri, W. Inorganic Nanoparticles as Optically Effective Additives for Polymers. *Chemical Engineering Communications* **2009**, 196 (5), 549–572. <https://doi.org/10.1080/00986440802483954>.
- (12) Hanemann, T.; Szabó, D. V. *Polymer-Nanoparticle Composites: From Synthesis to Modern Applications*; 2010; Vol. 3. <https://doi.org/10.3390/ma3063468>.
- (13) Carter, B.; Norton, G. *Ceramic Materials Science and Engineering*; 2007. <https://doi.org/10.1007/978-0-387-46271-4>.

- (14) Russo, M.; Campoy-Quiles, M.; Lacharmoise, P.; Ferenczi, T. A. M.; Garriga, M.; Caseri, W. R.; Stingelin, N. One-Pot Synthesis of Polymer/Inorganic Hybrids: Toward Readily Accessible, Low-Loss, and Highly Tunable Refractive Index Materials and Patterns. *Journal of Polymer Science, Part B: Polymer Physics* **2012**, *50* (1), 65–74. <https://doi.org/10.1002/polb.22373>.
- (15) Caseri, W. Nanocomposites of Polymers and Metals or Semiconductors: Historical Background and Optical Properties. *Macromolecular Rapid Communications* **2000**, *21* (11), 705–722. [https://doi.org/10.1002/1521-3927\(20000701\)21:11<705::AID-MARC705>3.0.CO;2-3](https://doi.org/10.1002/1521-3927(20000701)21:11<705::AID-MARC705>3.0.CO;2-3).
- (16) Macleod, H. A. *Thin-Film Optical Filters, Fifth Edition*; CRC Press, 2018.
- (17) Hecht, E. *Optics*, 5th Ed.; 2016.
- (18) Rubin, M. Optical Properties of Soda Lime Silica Glasses. *Solar Energy Materials* **1985**, *12* (4), 275–288. [https://doi.org/10.1016/0165-1633\(85\)90052-8](https://doi.org/10.1016/0165-1633(85)90052-8).
- (19) Nussbaumer, R. J.; Caseri, W. R.; Smith, P.; Tervoort, T. Polymer-TiO₂ Nanocomposites: A Route towards Visually Transparent Broadband UV Filters and High Refractive Index Materials. *Macromolecular Materials and Engineering* **2003**, *288* (1), 44–49. <https://doi.org/10.1002/mame.200290032>.
- (20) Zimmermann, L.; Weibel, M.; Caseri, W.; Suter, U. W. High Refractive Index Films of Polymer Nanocomposites. *Journal of Materials Research* **1993**, *8* (7), 1742–1748. <https://doi.org/10.1557/JMR.1993.1742>.
- (21) Diebold, U. *The Surface Science of Titanium Dioxide*; 2003; Vol. 48. [https://doi.org/10.1016/S0167-5729\(02\)00100-0](https://doi.org/10.1016/S0167-5729(02)00100-0).
- (22) Zhang, M.; Lin, G.; Dong, C.; Wen, L. Amorphous TiO₂ films with High Refractive Index Deposited by Pulsed Bias Arc Ion Plating. *Surface and Coatings Technology* **2007**, *201* (16–17), 7252–7258. <https://doi.org/10.1016/j.surfcoat.2007.01.043>.
- (23) Zhang, H. Z.; Banfield, J. F. Thermodynamic Analysis of Phase Stability of Nanocrystalline Titania. *Journal of Materials Chemistry* **1998**, *8* (9), 2073–2076. <https://doi.org/10.1039/a802619j>.
- (24) Stride, J. A.; Tuong, N. T. Controlled Synthesis of Titanium Dioxide Nanostructures. *Solid State Phenomena* **2010**, *162*, 261–294. <https://doi.org/10.4028/www.scientific.net/SSP.162.261>.
- (25) Anpo, M. Applications of Titanium Oxide Photocatalysts and Unique Second-Generation TiO₂ Photocatalysts Able to Operate under Visible Light Irradiation for the Reduction of Environmental Toxins on a Global Scale. *Studies In Surface Science And Catalysis* **2000**, 157–166.
- (26) Weiser, H. B.; Milligan, W. O. X-Ray Studies on the Hydrous Oxides. *The Journal of Physical Chemistry* **1934**, *39* (1), 25–34. <https://doi.org/10.1021/j150361a003>.

- (27) Russo, M.; Rigby, S. E. J.; Caseri, W.; Stingelin, N. Pronounced Photochromism of Titanium Oxide Hydrates (Hydrous TiO₂). *Journal of Materials Chemistry* **2010**, 20 (7), 1348–1356. <https://doi.org/10.1039/b917152e>.
- (28) Bachevillier, S.; Yuan, H. K.; Strang, A.; Levitsky, A.; Frey, G. L.; Hafner, A.; Bradley, D. D. C.; Stavrinou, P. N.; Stingelin, N. Fully Solution-Processed Photonic Structures from Inorganic/Organic Molecular Hybrid Materials and Commodity Polymers. *Advanced Functional Materials* **2019**, 1808152, 1–7. <https://doi.org/10.1002/adfm.201808152>.
- (29) Meier, C.; Gondorf, A.; Lüttjohann, S.; Lorke, A.; Wiggers, H. Silicon Nanoparticles: Absorption, Emission, and the Nature of the Electronic Bandgap. *Journal of Applied Physics* **2007**, 101 (10), 103112. <https://doi.org/10.1063/1.2720095>.
- (30) Sultanova, N.; Kasarova, S.; Nikolov, I. Dispersion Properties of Optical Polymers. *Acta Physica Polonica A* **2009**, 116 (4), 585–587. <https://doi.org/10.12693/APhysPolA.116.585>.
- (31) Sultanova, N. G.; Kasarova, S. N.; Nikolov, I. D. Characterization of Optical Properties of Optical Polymers. *Optical and Quantum Electronics* **2013**, 45 (3), 221–232. <https://doi.org/10.1007/s11082-012-9616-6>.
- (32) Bruggeman, D. A. G. Berechnung Verschiedener Physikalischer Konstanten von Heterogenen Substanzen. I. Dielektrizitätskonstanten Und Leitfähigkeiten Der Mischkörper Aus Isotropen Substanzen. *Ann Phys* **1935**, 416 (7), 636–664. <https://doi.org/10.1002/ANDP.19354160705>.
- (33) Bachevillier, S. Solution-Processed Photonics for Light and Heat Management, Imperial College London, 2019.
- (34) Strang, A. Organic / Inorganic Hybrid Material for Solution-Processed Photonics Applications by Declaration of Authorship, Imperial College London, 2015.
- (35) Zewde, B.; Pitliya, P.; Raghavan, D. The Role of Surface Modified TiO₂ Nanoparticles on the Mechanical and Thermal Properties of CTBN Toughened Epoxy Nanocomposite. *Journal of Materials Science* **2016**, 51 (20), 9314–9329. <https://doi.org/10.1007/s10853-016-0179-y>.
- (36) Bandi, S.; Schiraldi, D. A. Glass Transition Behavior of Clay Aerogel/Poly(Vinyl Alcohol) Composites. *Macromolecules* **2006**, 39 (19), 6537–6545. <https://doi.org/10.1021/ma0611826>.
- (37) Loshaek, S.; Fox, T. G. Cross-Linked Polymers. I. Factors Influencing the Efficiency of Cross-Linking in Copolymers of Methyl Methacrylate and Glycol Dimethacrylates. *J Am Chem Soc* **1953**, 75 (14), 3544–3550. <https://doi.org/10.1021/ja01110a068>.
- (38) Fred-Ahmadu, O. H.; Bhagwat, G.; Oluyoye, I.; Benson, N. U.; Ayejuyo, O. O.; Palanisami, T. Interaction of Chemical Contaminants with Microplastics: Principles and Perspectives. *Science of the Total Environment* **2020**, 706, 135978. <https://doi.org/10.1016/j.scitotenv.2019.135978>.

- (39) Uhl, F. M.; Levchik, G. F.; Levchik, S. v.; Dick, C.; Liggat, J. J.; Snape, C. E.; Wilkie, C. A. Thermal Stability of Cross-Linked Polymers: Methyl Methacrylate with Divinylbenzene and Styrene with Dimethacrylates. *Polymer Degradation and Stability* **2001**, 71 (2), 317–325. [https://doi.org/10.1016/S0141-3910\(00\)00181-6](https://doi.org/10.1016/S0141-3910(00)00181-6).
- (40) Sonker, A. K.; Rathore, K.; Nagarale, R. K.; Verma, V. Crosslinking of Polyvinyl Alcohol (PVA) and Effect of Crosslinker Shape (Aliphatic and Aromatic) Thereof. *Journal of Polymers and the Environment* **2018**, 26 (5), 1782–1794. <https://doi.org/10.1007/s10924-017-1077-3>.
- (41) Ballistreri, A.; Foti, S.; Montaudo, G.; Scamporrino, E. Evolution of Aromatic Compounds in the Thermal Decomposition of Vinyl Polymers. *J Polym Sci A1* **1980**, 18 (4), 1147–1153. <https://doi.org/10.1002/pol.1980.170180401>.
- (42) Takahashi, T. Thermal Decomposition Products of Polymers. *Sen'i Gakkaishi* **1974**, 30 (1), 3151–3158. <https://doi.org/10.2115/fiber.30.P11>.
- (43) Holland, B. J.; Hay, J. N. The Thermal Degradation of Poly(Vinyl Alcohol). *Polymer (Guildf)* **2001**, 42 (16), 6775–6783. [https://doi.org/10.1016/S0032-3861\(01\)00166-5](https://doi.org/10.1016/S0032-3861(01)00166-5).
- (44) Akhter, S.; Allan, K.; Buchanan, D.; Cook, J. A.; Campion, A.; White, J. M. XPS and IR Study of X-Ray Induced Degradation of PVA Polymer Film. *Applied Surface Science* **1988**, 35 (2), 241–258. [https://doi.org/10.1016/0169-4332\(88\)90053-0](https://doi.org/10.1016/0169-4332(88)90053-0).
- (45) Ni, T.; Huang, G. S.; Zheng, J.; Gao, P.; Chen, M. M. Research on the Crosslinking Mechanism of Polyacrylamide/Resol Using Molecular Simulation and X-Ray Photoelectron Spectroscopy. *Polymer Journal* **2010**, 42 (5), 357–362. <https://doi.org/10.1038/pj.2010.10>.
- (46) Li, Y.; Ma, X.; Ju, J.; Sun, X.; Deng, N.; Li, Z.; Kang, W.; Cheng, B. Preparation and Characterization of Crosslinked Electrospun Pullulan Nanofiber Membrane as a Potential for Biomaterials. *Journal of the Textile Institute* **2018**, 109 (6), 750–756. <https://doi.org/10.1080/00405000.2017.1368107>.
- (47) Woo, J. H.; Kim, N. H.; Kim, S. il; Park, O. K.; Lee, J. H. Effects of the Addition of Boric Acid on the Physical Properties of MXene/Polyvinyl Alcohol (PVA) Nanocomposite. *Composites Part B: Engineering* **2020**, 199 (May), 108205. <https://doi.org/10.1016/j.compositesb.2020.108205>.
- (48) Delekar, S. D.; Dhodamani, A. G.; More, K. v.; Dongale, T. D.; Kamat, R. K.; Acquah, S. F. A.; Dalal, N. S.; Panda, D. K. Structural and Optical Properties of Nanocrystalline TiO₂ with Multiwalled Carbon Nanotubes and Its Photovoltaic Studies Using Ru(II) Sensitizers. *ACS Omega* **2018**, 3 (3), 2743–2756. <https://doi.org/10.1021/acsomega.7b01316>.
- (49) Cheng, A. T. Y.; Rodriguez, F. Mechanical Properties of Borate Crosslinked Poly(Vinyl Alcohol) Gels. *Journal of Applied Polymer Science* **1981**, 26 (11), 3895–3908. <https://doi.org/10.1002/app.1981.070261134>.

- (50) Kakihana, M.; Kobayashi, M.; Tomita, K.; Petrykin, V. Application of Water-Soluble Titanium Complexes as Precursors for Synthesis of Titanium-Containing Oxides via Aqueous Solution Processes. *Bull Chem Soc Jpn* **2010**, *83* (11), 1285–1308. <https://doi.org/10.1246/bcsj.20100103>.
- (51) Lee, J. H.; Koh, C. Y.; Singer, J. P.; Jeon, S. J.; Maldovan, M.; Stein, O.; Thomas, E. L. 25th Anniversary Article: Ordered Polymer Structures for the Engineering of Photons and Phonons. *Advanced Materials* **2014**, *26* (4), 532–569. <https://doi.org/10.1002/ADMA.201303456>.
- (52) Kazmierczak, T.; Song, H.; Hiltner, A.; Baer, E. Polymeric One-Dimensional Photonic Crystals by Continuous Coextrusion. *Macromolecular Rapid Communications* **2007**, *28* (23), 2210–2216. <https://doi.org/10.1002/marc.200700367>.
- (53) Gazzo, S.; Manfredi, G.; Pötzsch, R.; Wei, Q.; Alloisio, M.; Voit, B.; Comoretto, D. High Refractive Index Hyperbranched Polyvinylsulfides for Planar One-Dimensional All-Polymer Photonic Crystals. *Journal of Polymer Science, Part B: Polymer Physics* **2016**, *54* (1), 73–80. <https://doi.org/10.1002/polb.23932>.
- (54) Tavella, C.; Lova, P.; Marsotto, M.; Luciano, G.; Patrini, M.; Stagnaro, P.; Comoretto, D. High Refractive Index Inverse Vulcanized Polymers for Organic Photonic Crystals. *Crystals (Basel)* **2020**, *10* (3), 1–10. <https://doi.org/10.3390/cryst10030154>.
- (55) Bailey, J.; Sharp, J. S. Thin Film Polymer Photonics: Spin Cast Distributed Bragg Reflectors and Chirped Polymer Structures. *European Physical Journal E* **2010**, *33* (1), 41–49. <https://doi.org/10.1140/epje/i2010-10657-4>.
- (56) Álvarez, A. L.; Tito, J.; Vaello, M. B.; Velásquez, P.; Mallavia, R.; Sánchez-López, M. M.; Fernández de Ávila, S. Polymeric Multilayers for Integration into Photonic Devices. In *Thin Solid Films*; Elsevier, 2003; Vol. 433, pp 277–280. [https://doi.org/10.1016/S0040-6090\(03\)00348-1](https://doi.org/10.1016/S0040-6090(03)00348-1).
- (57) Tagaya, A.; Lou, L.; Ide, Y.; Koike, Y.; Okamoto, Y. Improvement of the Physical Properties of Poly(Methyl Methacrylate) by Copolymerization with N-Pentafluorophenyl Maleimide; Zero-Orientational and Photoelastic Birefringence Polymers with High Glass Transition Temperatures. *Science China Chemistry* **2012**, *55* (5), 850–853. <https://doi.org/10.1007/s11426-012-4498-9>.
- (58) Maurer, J. J.; Eustace, D. J.; Ratcliffe, C. T. Thermal Characterization of Poly (Acrylic Acid). *Macromolecules* **1987**, No. 20, 196–202.
- (59) Kamide, K.; Saito, M. Thermal Analysis of Cellulose Acetate Solids with Total Degrees of Substitution of 0.49, 1.75, 2.46, and 2.92. *Polymer Journal* **1985**, *17* (8), 919–928.
- (60) Fox, T. G.; Flory, P. J. Second-Order Transition Temperatures and Related Properties of Polystyrene. I. Influence of Molecular Weight. *Journal of Applied Physics* **1950**, *21* (6), 581–591. <https://doi.org/10.1063/1.1699711>.

- (61) al Lafi, A. G.; Hay, J. N. Stereo-Chemical Contributions to the Glass Transition and Liquid-Liquid Phase Separation in High Molecular Weight Poly(N-Vinyl Carbazole). *RSC Advances* **2016**, 6 (35), 29326–29333. <https://doi.org/10.1039/c6ra00097e>.
- (62) Zhao, H.; Ismail, K.; Weber, S. G. How Fluorous Is Poly(2,2-Bis(Trifluoromethyl)-4,5-Difluoro-1,3-Dioxide-Co- Tetrafluoroethylene) (Teflon AF)? *J Am Chem Soc* **2004**, 126 (41), 13184–13185. <https://doi.org/10.1021/ja047453e>.
- (63) Yablonovitch, E. *Inhibited Spontaneous Emission in Solid-State Physics and Electronics*; 1987; Vol. 58. <https://doi.org/10.1103/PhysRevLett.58.2059>.
- (64) John, S. *Strong Localization of Photons in Certain Disordered Dielectric Superlattices*; 1987; Vol. 58. <https://doi.org/10.1103/PhysRevLett.58.2486>.
- (65) Bates, F. Block Copolymer Thermodynamics: Theory And Experiment. *Annual Review of Physical Chemistry* **1990**, 41 (1), 525–557. <https://doi.org/10.1146/annurev.physchem.41.1.525>.
- (66) Parker, A. R. 515 Million Years of Structural Colour. *Journal of Optics A: Pure and Applied Optics* **2000**, 2 (6), R15–R28. <https://doi.org/10.1088/1464-4258/2/6/201>.
- (67) Parker, A. R.; Mckenzie, D. R.; J Large, M. C.; Large, M. C. J. Multilayer Reflectors in Animals Using Green and Gold Beetles as Contrasting Examples. *Journal of Experimental Biology* **1998**, 201 (9), 1307–1313.
- (68) Vignolini, S.; Rudall, P. J.; Rowland, A. v.; Reed, A.; Moyroud, E.; Faden, R. B.; Baumberg, J. J.; Glover, B. J.; Steiner, U. Pointillist Structural Color in Pollia Fruit. *Proc Natl Acad Sci U S A* **2012**, 109 (39), 15712–15715. <https://doi.org/10.1073/pnas.1210105109>.
- (69) Lova, P.; Manfredi, G.; Comoretto, D. Advances in Functional Solution Processed Planar 1D Photonic Crystals. *Advanced Optical Materials* **2018**, 6 (24), 1800730. <https://doi.org/10.1002/adom.201800730>.
- (70) Weber, M. F.; Stover, C. A.; Gilbert, L. R.; Nevitt, T. J.; Ouderkirk, A. J. *Giant Birefringent Optics in Multilayer Polymer Mirrors*; 2000; Vol. 287. <https://doi.org/10.1126/science.287.5462.2451>.
- (71) Komikado, T.; Inoue, A.; Masuda, K.; Ando, T.; Umegaki, S. Multi-Layered Mirrors Fabricated by Spin-Coating Organic Polymers. *Thin Solid Films* **2007**, 515 (7–8), 3887–3892. <https://doi.org/10.1016/J.TSF.2006.10.119>.
- (72) Bronnbauer, C.; Hornich, J.; Gasparini, N.; Guo, F.; Hartmeier, B.; Luechinger, N. A.; Pflaum, C.; Brabec, C. J.; Forberich, K. Printable Dielectric Mirrors with Easily Adjustable and Well-Defined Reflection Maxima for Semitransparent Organic Solar Cells. *Advanced Optical Materials* **2015**, 3 (10), 1424–1430. <https://doi.org/10.1002/ADOM.201500216>.
- (73) Dip Coating: Practical Guide to Theory and Troubleshooting <https://www.ossila.com/pages/dip-coating#overview>.

- (74) Scriven, L. E. Physics and Applications of DIP Coating and Spin Coating. *MRS Online Proceedings Library 1988 121:1* **2011**, 121 (1), 717–729. <https://doi.org/10.1557/PROC-121-717>.
- (75) Brudieu, B.; Bris, A. le; Teisseire, J.; Guillemot, F.; Dantelle, G.; Misra, S.; Cabarrocas, P. R. i.; Sorin, F.; Gacoin, T. Sol-Gel Route Toward Efficient and Robust Distributed Bragg Reflectors for Light Management Applications. *Advanced Optical Materials* **2014**, 2 (11), 1105–1112. <https://doi.org/10.1002/adom.201400292>.
- (76) Betancur, R.; Romero-Gomez, P.; Martinez-Otero, A.; Elias, X.; Maymó, M.; Martorell, J. Transparent Polymer Solar Cells Employing a Layered Light-Trapping Architecture. *Nature Photonics* **2013**, 7 (12), 995–1000. <https://doi.org/10.1038/nphoton.2013.276>.
- (77) Romero-Gómez, P.; Pastorelli, F.; Mantilla-Pérez, P.; Mariano, M.; Martínez-Otero, A.; Elias, X.; Betancur, R.; Martorell, J. Semi-Transparent Polymer Solar Cells. *Journal of Photonics for Energy* **2015**, 5 (1), 057212. <https://doi.org/10.1117/1.jpe.5.057212>.
- (78) Ramírez Quiroz, C. O.; Bronnbauer, C.; Levchuk, I.; Hou, Y.; Brabec, C. J.; Forberich, K. Coloring Semitransparent Perovskite Solar Cells via Dielectric Mirrors. *ACS Nano* **2016**, 10 (5), 5104–5112. <https://doi.org/10.1021/acsnano.6b00225>.
- (79) Zhang, W.; Anaya, M.; Lozano, G.; Calvo, M. E.; Johnston, M. B.; Míguez, H.; Snaith, H. J. Highly Efficient Perovskite Solar Cells with Tunable Structural Color. *Nano Letters* **2015**, 15 (3), 1698–1702. https://doi.org/10.1021/NL504349Z/SUPPL_FILE/NL504349Z_SI_001.PDF.
- (80) Allardyce, C. S.; Fankhauser, C.; Zakeeruddin, S. M.; Grätzel, M.; Dyson, P. J. The Influence of Greenhouse-Integrated Photovoltaics on Crop Production. *Solar Energy* **2017**, 155, 517–522. <https://doi.org/10.1016/J.SOLENER.2017.06.044>.
- (81) Ravishankar, E.; Charles, M.; Xiong, Y.; Henry, R.; Swift, J.; Rech, J.; Calero, J.; Cho, S.; Booth, R. E.; Kim, T.; Balzer, A. H.; Qin, Y.; Hoi Yi Ho, C.; So, F.; Stingelin, N.; Amassian, A.; Saravitz, C.; You, W.; Ade, H.; Sederoff, H.; O'Connor, B. T. Balancing Crop Production and Energy Harvesting in Organic Solar-Powered Greenhouses. *Cell Reports Physical Science* **2021**, 2 (3), 100381. <https://doi.org/10.1016/J.XCRP.2021.100381>.
- (82) Sun, X.; Silverman, T. J.; Zhou, Z.; Khan, M. R.; Bermel, P.; Alam, M. A. Optics-Based Approach to Thermal Management of Photovoltaics: Selective-Spectral and Radiative Cooling. *IEEE Journal of Photovoltaics* **2017**, 7 (2), 566–574. <https://doi.org/10.1109/JPHOTOV.2016.2646062>.
- (83) Slauch, I. M.; Deceglie, M. G.; Silverman, T. J.; Ferry, V. E. Spectrally Selective Mirrors with Combined Optical and Thermal Benefit for Photovoltaic Module Thermal Management. *ACS Photonics* **2018**, 5 (4), 1528–1538. <https://doi.org/10.1021/acsp Photonics.7b01586>.
- (84) Sargunanathan, S.; Elango, A.; Mohideen, S. T. Performance Enhancement of Solar Photovoltaic Cells Using Effective Cooling Methods: A Review. *Renewable and Sustainable Energy Reviews* **2016**, 64, 382–393. <https://doi.org/10.1016/j.rser.2016.06.024>.

- (85) Li, W.; Shi, Y.; Chen, K.; Zhu, L.; Fan, S. A Comprehensive Photonic Approach for Solar Cell Cooling. *ACS Photonics* **2017**, 4 (4), 774–782. <https://doi.org/10.1021/acsp Photonics.7b00089>.
- (86) EnergyPlus Version 8.6 Documentation. *US Department of Energy*. 2016, pp 1–847.
- (87) Holtz, J. H.; Asher, S. A. Polymerized Colloidal Crystal Hydrogel Films as Intelligent Chemical Sensing Materials. *Nature* **1997**, 389 (6653), 829–832. <https://doi.org/10.1038/39834>.
- (88) Lova, P. Selective Polymer Distributed Bragg Reflector Vapor Sensors. *Polymers (Basel)* **2018**, 10 (10). <https://doi.org/10.3390/polym10101161>.
- (89) Giusto, P.; Lova, P.; Manfredi, G.; Gazzo, S.; Srinivasan, P.; Radice, S.; Comoretto, D. Colorimetric Detection of Perfluorinated Compounds by All-Polymer Photonic Transducers. *ACS Omega* **2018**, 3 (7), 7517–7522. <https://doi.org/10.1021/acsomega.8b00554>.
- (90) Lova, P.; Manfredi, G.; Boarino, L.; Comite, A.; Laus, M.; Patrini, M.; Marabelli, F.; Soci, C.; Comoretto, D. Polymer Distributed Bragg Reflectors for Vapor Sensing. *ACS Photonics* **2015**, 2 (4), 537–543. <https://doi.org/10.1021/ph500461w>.
- (91) Barry, R. A.; Wiltzius, P. Humidity-Sensing Inverse Opal Hydrogels. *Langmuir* **2006**, 22 (3), 1369–1374. <https://doi.org/10.1021/la0519094>.
- (92) Gleason, K. K.; Karaman, M.; Kooi, S. E. Vapor Deposition of Hybrid Organic-Inorganic Dielectric Bragg Mirrors Having Rapid and Reversibly Tunable Optical Reflectance. *Chemistry of Materials* **2008**, 20 (6), 2262–2267. <https://doi.org/10.1021/cm703107d>.
- (93) Tian, E.; Wang, J.; Zheng, Y.; Song, Y.; Jiang, L.; Zhu, D. Colorful Humidity Sensitive Photonic Crystal Hydrogel. *Journal of Materials Chemistry* **2008**, 18 (10), 1116–1122. <https://doi.org/10.1039/b717368g>.
- (94) Jadun, P.; McMillan, C.; Stenberg, D.; Muratori, M.; Vimmerstedt, L.; Mai, T. Electrification Futures Study : End-Use Electric Technology Cost. *National Renewable Energy Lab*. Golden, CO: National Renewable Energy Laboratory 2017, p 109.
- (95) Zhao, D.; McCoy, A.; Du, J. An Empirical Study on the Energy Consumption in Residential Buildings after Adopting Green Building Standards. *Procedia Engineering* **2016**, 145, 766–773. <https://doi.org/10.1016/j.proeng.2016.04.100>.
- (96) Rissman, J.; Kennan, H. Low-Emissivity Windows. *Case Studies on the Government’s Role in Energy Technology Innovation* **2013**.
- (97) Casini, M. Smart Windows for Energy Efficiency of Buildings. *International Journal of Civil and Structural Engineering - IJCSE* **2015**, No. May.
- (98) Ellmers, C.; Leu, S.; Hofmann, M. R.; Karaiskaj, D.; Ruehle, W. W.; Stolz, W. Ultrafast Dynamic Response of Strain-Compensated (GaIn)As/Ga(PAs) Microcavity Lasers. *Vertical-Cavity Surface-Emitting Lasers III* **1999**, 3627, 70. <https://doi.org/10.1117/12.347088>.

- (99) Ferreira, J. A.; Grassi, M.; Gudiño, E.; de Oliveira, P. A New Look to Non-Fickian Diffusion. *Applied Mathematical Modelling* **2015**, *39* (1), 194–204. <https://doi.org/10.1016/J.APM.2014.05.030>.
- (100) Rehage, G.; Ernst, O.; Fuhrmann, J. Fickian and Non-Fickian Diffusion in High Polymer Systems. *Discuss Faraday Soc* **1970**, *49* (0), 208–221. <https://doi.org/10.1039/DF9704900208>.
- (101) Wood, J.; Gladden, L. F. Modelling Diffusion and Reaction Accompanied by Capillary Condensation Using Three-Dimensional Pore Networks. Part 1. Fickian Diffusion and Pseudo-First-Order Reaction Kinetics. *Chemical Engineering Science* **2002**, *57* (15), 3033–3045. [https://doi.org/10.1016/S0009-2509\(02\)00183-5](https://doi.org/10.1016/S0009-2509(02)00183-5).
- (102) Yeo, T. L.; Sun, T.; Grattan, K. T. V.; Parry, D.; Lade, R.; Powell, B. D. Characterisation of a Polymer-Coated Fibre Bragg Grating Sensor for Relative Humidity Sensing. *Sensors and Actuators B: Chemical* **2005**, *110* (1), 148–156. <https://doi.org/10.1016/J.SNB.2005.01.033>.
- (103) Flory, P. J. Statistical Mechanics of Swelling of Network Structures. *The Journal of Chemical Physics* **1950**, *18* (1), 108–111. <https://doi.org/10.1063/1.1747424>.
- (104) Keener, J. P.; Sircar, S.; Fogelson, A. L. Influence of the Standard Free Energy on Swelling Kinetics of Gels. *PHYSICAL REVIEW E* **2011**, *83*, 41802. <https://doi.org/10.1103/PhysRevE.83.041802>.
- (105) Liu, Y.; Daum, P. H. Relationship of Refractive Index to Mass Density and Self-Consistency of Mixing Rules for Multicomponent Mixtures like Ambient Aerosols. *Journal of Aerosol Science* **2008**, *39* (11), 974–986. <https://doi.org/10.1016/J.JAEROSCI.2008.06.006>.
- (106) Wunderlich, B.; Grebowicz, J. Thermotropic Mesophases and Mesophase Transitions of Linear, Flexible Macromolecules. **1984**, 1–59. https://doi.org/10.1007/3-540-12994-4_1.
- (107) Schick, C. Differential Scanning Calorimetry (DSC) of Semicrystalline Polymers. *Analytical and Bioanalytical Chemistry* **2009**, *395* (6), 1589–1611. <https://doi.org/10.1007/s00216-009-3169-y>.
- (108) Minakov, A. A.; Schick, C. Ultrafast Thermal Processing and Nanocalorimetry at Heating and Cooling Rates up to 1 MKs. *Review of Scientific Instruments* **2007**, *78* (7). <https://doi.org/10.1063/1.2751411>.
- (109) Rhoades, A. M.; Williams, J. L.; Androsch, R. Crystallization Kinetics of Polyamide 66 at Processing-Relevant Cooling Conditions and High Supercooling. *Thermochimica Acta* **2015**, *603*, 103–109. <https://doi.org/10.1016/J.TCA.2014.10.020>.
- (110) Qian, Z.; Galuska, L.; McNutt, W. W.; Ocheje, M. U.; He, Y.; Cao, Z.; Zhang, S.; Xu, J.; Hong, K.; Goodman, R. B.; Rondeau-Gagné, S.; Mei, J.; Gu, X. Challenge and Solution of Characterizing Glass Transition Temperature for Conjugated Polymers by Differential Scanning Calorimetry. *Journal of Polymer Science, Part B: Polymer Physics* **2019**, *57* (23), 1635–1644. <https://doi.org/10.1002/polb.24889>.

- (111) Adamovsky, S.; Schick, C. Ultra-Fast Isothermal Calorimetry Using Thin Film Sensors. *Thermochimica Acta* **2004**, *415* (1–2), 1–7. <https://doi.org/10.1016/j.tca.2003.07.015>.
- (112) Zhuravlev, E.; Madhavi, V.; Lustiger, A.; Androsch, R.; Schick, C. Crystallization of Polyethylene at Large Undercooling. *ACS Macro Letters* **2016**, *5* (3), 365–370. <https://doi.org/10.1021/acsmacrolett.5b00889>.
- (113) McKenna, G. B.; Simon, S. L. 50th Anniversary Perspective: Challenges in the Dynamics and Kinetics of Glass-Forming Polymers. *Macromolecules* **2017**, *50* (17), 6333–6361. <https://doi.org/10.1021/acs.macromol.7b01014>.
- (114) MOYNIHAN, C. T.; EASTEAL, A. J.; de BOLT, M. A. N. N.; TUCKER, J. Dependence of the Fictive Temperature of Glass on Cooling Rate. *Journal of the American Ceramic Society* **1976**, *59* (1–2), 12–16. <https://doi.org/https://doi.org/10.1111/j.1151-2916.1976.tb09376.x>.
- (115) Kauzmann, W. The Nature of the Glassy State and the Behavior of Liquids at Low Temperatures. *Chemical Reviews* **1948**, *43* (2), 219–256. <https://doi.org/10.1021/cr60135a002>.
- (116) Gibbs, J. H.; DiMarzio, E. A. Nature of the Glass Transition and the Glassy State. *The Journal of Chemical Physics* **2004**, *28* (3), 373. <https://doi.org/10.1063/1.1744141>.
- (117) Pyda, M.; Wunderlich, B. Analysis of the Residual Entropy of Amorphous Polyethylene at 0 K*. *Journal of Polymer Science Part B: Polymer Physics* **2002**, *40* (12), 1245–1253. <https://doi.org/10.1002/POLB.10160>.
- (118) Struik, L. C. E. Physical Aging in Plastics and Other Glassy Materials. *Polymer Engineering & Science* **1977**, *17* (3), 165–173. <https://doi.org/10.1002/pen.760170305>.
- (119) Roth, C. B. *Polymer Glasses*, 1st ed.; Roth, C. B., Ed.; CRC Press, 2016. <https://doi.org/10.4324/9781315305158>.
- (120) Schick, C.; Mathot, V. *Fast Scanning Calorimetry*; 2016. <https://doi.org/10.1007/978-3-319-31329-0>.
- (121) Yao, Z. F.; Wang, J. Y.; Pei, J. High-Performance Polymer Field-Effect Transistors: From the Perspective of Multi-Level Microstructures. *Chemical Science* **2021**, *12* (4), 1193–1205. <https://doi.org/10.1039/d0sc06497a>.
- (122) Mooney, M.; Nyayachavadi, A.; Rondeau-Gagné, S. Eco-Friendly Semiconducting Polymers: From Greener Synthesis to Greener Processability. *Journal of Materials Chemistry C* **2020**, *8* (42), 14645–14664. <https://doi.org/10.1039/d0tc04085a>.
- (123) Endrodi, B.; Mellár, J.; Gingl, Z.; Visy, C.; Janáky, C. Molecular and Supramolecular Parameters Dictating the Thermoelectric Performance of Conducting Polymers: A Case Study Using Poly(3-Alkylthiophene)s. *Journal of Physical Chemistry C* **2015**, *119* (16), 8472–8479. <https://doi.org/10.1021/acs.jpcc.5b00135>.

- (124) Vijayakumar, V.; Zaborova, E.; Biniek, L.; Zeng, H.; Herrmann, L.; Carvalho, A.; Boyron, O.; Leclerc, N.; Brinkmann, M. Effect of Alkyl Side Chain Length on Doping Kinetics, Thermopower, and Charge Transport Properties in Highly Oriented F4 TCNQ-Doped PBTFT Films. *ACS Applied Materials and Interfaces* **2019**, *11* (5), 4942–4953. <https://doi.org/10.1021/acsami.8b17594>.
- (125) Mooney, M.; Wang, Y.; Nyayachavadi, A.; Zhang, S.; Gu, X.; Rondeau-Gagné, S. Enhancing the Solubility of Semiconducting Polymers in Eco-Friendly Solvents with Carbohydrate-Containing Side Chains. *ACS Applied Materials and Interfaces* **2021**. <https://doi.org/10.1021/acsami.1c02860>.
- (126) Tran, H. N.; Park, S.; Wibowo, F. T. A.; Krishna, N. V.; Kang, J. H.; Seo, J. H.; Nguyen-Phu, H.; Jang, S. Y.; Cho, S. 17% Non-Fullerene Organic Solar Cells with Annealing-Free Aqueous MoO₃. *Advanced Science* **2020**, *7* (21), 1–11. <https://doi.org/10.1002/advs.202002395>.
- (127) Guo, Q.; Guo, Q.; Geng, Y.; Tang, A.; Zhang, M.; Du, M.; Sun, X.; Zhou, E. Recent Advances in PM6:Y6-Based Organic Solar Cells. *Materials Chemistry Frontiers* **2021**, *5* (8), 3257–3280. <https://doi.org/10.1039/d1qm00060h>.
- (128) Müller, C.; Ferenczi, T. A. M.; Campoy-Quiles, M.; Frost, J. M.; Bradley, D. D. C.; Smith, P.; Stingelin-Stutzmann, N.; Nelson, J. Binary Organic Photovoltaic Blends: A Simple Rationale for Optimum Compositions. *Advanced Materials* **2008**, *20* (18), 3510–3515. <https://doi.org/10.1002/adma.200800963>.
- (129) Chirvase, D.; Parisi, J.; Hummelen, J. C.; Dyakonov, V. Influence of Nanomorphology on the Photovoltaic Action of Polymer-Fullerene Composites. *Nanotechnology* **2004**, *15* (9), 1317–1323. <https://doi.org/10.1088/0957-4484/15/9/035>.
- (130) Buchaca-Domingo, E.; Ferguson, A. J.; Jamieson, F. C.; McCarthy-Ward, T.; Shoaee, S.; Tumbleston, J. R.; Reid, O. G.; Yu, L.; Madec, M. B.; Pfannmöller, M.; Hermerschmidt, F.; Schröder, R. R.; Watkins, S. E.; Kopidakis, N.; Portale, G.; Amassian, A.; Heeney, M.; Ade, H.; Rumbles, G.; Durrant, J. R.; Stingelin, N. Additive-Assisted Supramolecular Manipulation of Polymer:Fullerene Blend Phase Morphologies and Its Influence on Photophysical Processes. *Materials Horizons* **2014**, *1* (2), 270–279. <https://doi.org/10.1039/c3mh00125c>.
- (131) Tong, Y.; Xiao, Z.; Du, X.; Zuo, C.; Li, Y.; Lv, M.; Yuan, Y.; Yi, C.; Hao, F.; Hua, Y.; Lei, T.; Lin, Q.; Sun, K.; Zhao, D.; Duan, C.; Shao, X.; Li, W.; Yip, H. L.; Xiao, Z.; Zhang, B.; Bian, Q.; Cheng, Y.; Liu, S.; Cheng, M.; Jin, Z.; Yang, S.; Ding, L. Progress of the Key Materials for Organic Solar Cells. *Scientia Sinica Chimica* **2020**, *50* (4), 437–446. <https://doi.org/10.1360/SSC-2020-0018>.
- (132) Dalnoki-Veress, K.; Forrest, J. A.; Stevens, J. R.; Dutcher, J. R. Phase Separation Morphology of Spin-Coated Polymer Blend Thin Films. *Physica A: Statistical Mechanics and its Applications* **1997**, *239* (1–3), 87–94. [https://doi.org/10.1016/S0378-4371\(96\)00471-2](https://doi.org/10.1016/S0378-4371(96)00471-2).

- (133) Inoue, T.; Ougizawa, T.; Yasuda, O.; Miyasaka, K. Development of Modulated Structure during Solution Casting of Polymer Blends. *Macromolecules* **1985**, *18* (1), 57–63. <https://doi.org/10.1021/ma00143a009>.
- (134) Treat, N. D.; Brady, M. A.; Smith, G.; Toney, M. F.; Kramer, E. J.; Hawker, C. J.; Chabynyc, M. L. Interdiffusion of PCBM and P3HT Reveals Miscibility in a Photovoltaically Active Blend. *Advanced Energy Materials* **2011**, *1* (1), 82–89. <https://doi.org/10.1002/aenm.201000023>.
- (135) Yu, L.; Davidson, E.; Sharma, A.; Andersson, M. R.; Segalman, R.; Müller, C. Isothermal Crystallization Kinetics and Time-Temperature-Transformation of the Conjugated Polymer: Poly(3-(2'-Ethyl)Hexylthiophene). *Chemistry of Materials* **2017**, *29* (13), 5654–5662. <https://doi.org/10.1021/acs.chemmater.7b01393>.
- (136) Marina, S.; Kaufmann, N. P.; Karki, A.; Gutiérrez-Meza, E.; Gutiérrez-Fernández, E.; Vollbrecht, J.; Solano, E.; Walker, B.; Bannock, J. H.; de Mello, J.; Silva, C.; Nguyen, T. Q.; Cangialosi, D.; Stingelin, N.; Martín, J. The Importance of Quantifying the Composition of the Amorphous Intermixed Phase in Organic Solar Cells. *Advanced Materials* **2020**, *32* (47). <https://doi.org/10.1002/adma.202005241>.
- (137) Hoke, E. T.; Sachs-Quintana, I. T.; Lloyd, M. T.; Kauvar, I.; Mateker, W. R.; Nardes, A. M.; Peters, C. H.; Kopidakis, N.; McGehee, M. D. The Role of Electron Affinity in Determining Whether Fullerenes Catalyze or Inhibit Photooxidation of Polymers for Solar Cells. *Advanced Energy Materials* **2012**, *2* (11), 1351–1357. <https://doi.org/10.1002/aenm.201200169>.
- (138) Speller, E. M.; Clarke, A. J.; Aristidou, N.; Wyatt, M. F.; Francàs, L.; Fish, G.; Cha, H.; Lee, H. K. H.; Luke, J.; Wadsworth, A.; Evans, A. D.; McCulloch, I.; Kim, J. S.; Haque, S. A.; Durrant, J. R.; Dimitrov, S. D.; Tsoi, W. C.; Li, Z. Toward Improved Environmental Stability of Polymer: Fullerene and Polymer:Nonfullerene Organic Solar Cells: A Common Energetic Origin of Light- A Nd Oxygen-Induced Degradation. *ACS Energy Letters* **2019**, *4* (4), 846–852. <https://doi.org/10.1021/acsenergylett.9b00109>.
- (139) Uddin, A.; Upama, M. B.; Yi, H.; Duan, L. Encapsulation of Organic and Perovskite Solar Cells: A Review. *Coatings* **2019**, *9* (2), 1–17. <https://doi.org/10.3390/coatings9020065>.
- (140) Müller, C. On the Glass Transition of Polymer Semiconductors and Its Impact on Polymer Solar Cell Stability. *Chemistry of Materials* **2015**, *27* (8), 2740–2754. <https://doi.org/10.1021/acs.chemmater.5b00024>.
- (141) Sachs-Quintana, I. T.; Heumüller, T.; Mateker, W. R.; Orozco, D. E.; Cheacharoen, R.; Sweetnam, S.; Brabec, C. J.; McGehee, M. D. Electron Barrier Formation at the Organic-Back Contact Interface Is the First Step in Thermal Degradation of Polymer Solar Cells. *Advanced Functional Materials* **2014**, *24* (25), 3978–3985. <https://doi.org/10.1002/adfm.201304166>.
- (142) Bergqvist, J.; Lindqvist, C.; Bäcke, O.; Ma, Z.; Tang, Z.; Tress, W.; Gustafsson, S.; Wang, E.; Olsson, E.; Andersson, M. R.; Inganäs, O.; Müller, C. Sub-Glass Transition Annealing

- Enhances Polymer Solar Cell Performance. *Journal of Materials Chemistry A* **2014**, 2 (17), 6146–6152. <https://doi.org/10.1039/c3ta14165a>.
- (143) Viswanathan, N. K.; Balasubramanian, S.; Li, L.; Kumar, J.; Tripathy, S. K. Surface-Initiated Mechanism for the Formation of Relief Gratings on Azo-Polymer Films. *Journal of Physical Chemistry B* **1998**, 102 (31), 6064–6070. <https://doi.org/10.1021/jp981425z>.
- (144) Botiz, I.; Freyberg, P.; Leordean, C.; Gabudean, A. M.; Astilean, S.; Yang, A. C. M.; Stingelin, N. Enhancing the Photoluminescence Emission of Conjugated MEH-PPV by Light Processing. *ACS Applied Materials and Interfaces* **2014**, 6 (7), 4974–4979. <https://doi.org/10.1021/am4060244>.
- (145) Distler, A.; Sauermann, T.; Egelhaaf, H. J.; Rodman, S.; Waller, D.; Cheon, K. S.; Lee, M.; Guldi, D. M. The Effect of PCBM Dimerization on the Performance of Bulk Heterojunction Solar Cells. *Advanced Energy Materials* **2014**, 4 (1), 1–6. <https://doi.org/10.1002/aenm.201300693>.
- (146) Sun, Y.; Takacs, C. J.; Cowan, S. R.; Seo, J. H.; Gong, X.; Roy, A.; Heeger, A. J. Efficient, Air-Stable Bulk Heterojunction Polymer Solar Cells Using MoO_x as the Anode Interfacial Layer. *Advanced Materials* **2011**, 23 (19), 2226–2230. <https://doi.org/10.1002/adma.201100038>.
- (147) Cho, S.; Seo, J. H.; Park, S. H.; Beaupré, S.; Leclerc, M.; Heeger, A. J. A Thermally Stable Semiconducting Polymer. *Advanced Materials* **2010**, 22 (11), 1253–1257. <https://doi.org/10.1002/adma.200903420>.
- (148) Sharma, A.; Pan, X.; Campbell, J. A.; Andersson, M. R.; Lewis, D. A. Unravelling the Thermomechanical Properties of Bulk Heterojunction Blends in Polymer Solar Cells. *Macromolecules* **2017**, 50 (8), 3347–3354. <https://doi.org/10.1021/acs.macromol.7b00430>.
- (149) Yamilova, O. R.; Martynov, I. v.; Brandvold, A. S.; Klimovich, I. v.; Balzer, A. H.; Akkuratov, A. v.; Kusnetsov, I. E.; Stingelin, N.; Troshin, P. A. What Is Killing Organic Photovoltaics: Light-Induced Crosslinking as a General Degradation Pathway of Organic Conjugated Molecules. *Advanced Energy Materials* **2020**, 10 (7), 1–10. <https://doi.org/10.1002/aenm.201903163>.
- (150) Xie, R.; Aplan, M. P.; Caggiano, N. J.; Weisen, A. R.; Su, T.; Müller, C.; Segad, M.; Colby, R. H.; Gomez, E. D. Local Chain Alignment via Nematic Ordering Reduces Chain Entanglement in Conjugated Polymers. *Macromolecules* **2018**, 51 (24), 10271–10284. <https://doi.org/10.1021/acs.macromol.8b01840>.
- (151) Vyazovkin, S.; Sbirrazzuoli, N.; Dranca, I. Variation of the Effective Activation Energy throughout the Glass Transition. *Macromolecular Rapid Communications* **2004**, 25 (19), 1708–1713. <https://doi.org/10.1002/marc.200400268>.
- (152) Vyazovkin, S.; Sbirrazzuoli, N. Isoconversional Kinetic Analysis of Thermally Stimulated Processes in Polymers. *Macromolecular Rapid Communications* **2006**, 27 (18), 1515–1532. <https://doi.org/10.1002/marc.200600404>.

- (153) Baklar, M.; Barard, S.; Sparrowe, D.; Wilson, R. M.; McCulloch, I.; Heeney, M.; Kreouzis, T.; Stingelin, N. Bulk Charge Transport in Liquid-Crystalline Polymer Semiconductors Based on Poly(2,5-Bis(3-Alkylthiophen-2-Yl)Thieno[3,2-b]Thiophene). *Polymer Chemistry* **2010**, 1 (9), 1448–1452. <https://doi.org/10.1039/c0py00056f>.
- (154) Noriega, R.; Rivnay, J.; Vandewal, K.; Koch, F. P. V.; Stingelin, N.; Smith, P.; Toney, M. F.; Salleo, A. A General Relationship between Disorder, Aggregation and Charge Transport in Conjugated Polymers. *Nature Materials* **2013**, 12 (11), 1038–1044. <https://doi.org/10.1038/nmat3722>.
- (155) Himmelberger, S.; Salleo, A. Engineering Semiconducting Polymers for Efficient Charge Transport. *MRS Communications* **2015**, 5 (3), 383–395. <https://doi.org/10.1557/mrc.2015.44>.
- (156) McCulloch, I.; Heeney, M.; Bailey, C.; Genevicius, K.; MacDonald, I.; Shkunov, M.; Sparrowe, D.; Tierney, S.; Wagner, R.; Zhang, W.; Chabinyc, M. L.; Kline, R. J.; McGehee, M. D.; Toney, M. F. Liquid-Crystalline Semiconducting Polymers with High Charge-Carrier Mobility. *Nature Materials* **2006**, 5 (4), 328–333. <https://doi.org/10.1038/nmat1612>.
- (157) Xie, R.; Weisen, A. R.; Lee, Y.; Aplan, M. A.; Fenton, A. M.; Masucci, A. E.; Kempe, F.; Sommer, M.; Pester, C. W.; Colby, R. H.; Gomez, E. D. Glass Transition Temperature from the Chemical Structure of Conjugated Polymers. *Nature Communications* **2020**, 11 (1), 4–11. <https://doi.org/10.1038/s41467-020-14656-8>.
- (158) Kang, B.; Kim, R.; Lee, S. B.; Kwon, S. K.; Kim, Y. H.; Cho, K. Side-Chain-Induced Rigid Backbone Organization of Polymer Semiconductors through Semifluoroalkyl Side Chains. *J Am Chem Soc* **2016**, 138 (11), 3679–3686. <https://doi.org/10.1021/jacs.5b10445>.
- (159) Carpenter, J. H.; Ghasemi, M.; Gann, E.; Angunawela, I.; Stuard, S. J.; Rech, J. J.; Ritchie, E.; O'Connor, B. T.; Atkin, J.; You, W.; DeLongchamp, D. M.; Ade, H. Competition between Exceptionally Long-Range Alkyl Sidechain Ordering and Backbone Ordering in Semiconducting Polymers and Its Impact on Electronic and Optoelectronic Properties. *Advanced Functional Materials* **2019**, 29 (5), 1–13. <https://doi.org/10.1002/adfm.201806977>.
- (160) Ito, T.; Shimomura, T.; Miura, T. Simulation Study of the Effect of the Side-Chain Structure on the Initial Nucleation Process of Polythiophene Derivatives. *Journal of Physical Chemistry B* **2017**, 121 (5), 1108–1117. <https://doi.org/10.1021/acs.jpcc.6b10848>.
- (161) Jamieson, F. C.; Domingo, E. B.; McCarthy-Ward, T.; Heeney, M.; Stingelin, N.; Durrant, J. R. Fullerene Crystallisation as a Key Driver of Charge Separation in Polymer/Fullerene Bulk Heterojunction Solar Cells. *Chemical Science* **2012**, 3 (2), 485–492. <https://doi.org/10.1039/c1sc00674f>.
- (162) Buchaca-Domingo, E.; Vandewal, K.; Fei, Z.; Watkins, S. E.; Scholes, F. H.; Bannock, J. H.; de Mello, J. C.; Richter, L. J.; DeLongchamp, D. M.; Amassian, A.; Heeney, M.; Salleo, A.; Stingelin, N. Direct Correlation of Charge Transfer Absorption with Molecular

- Donor:Acceptor Interfacial Area via Photothermal Deflection Spectroscopy. *J Am Chem Soc* **2015**, *137* (16), 5256–5259. <https://doi.org/10.1021/ja512410f>.
- (163) Miller, N. C.; Cho, E.; Gysel, R.; Risko, C.; Coropceanu, V.; Miller, C. E.; Sweetnam, S.; Sellinger, A.; Heeney, M.; McCulloch, I.; Brédas, J. L.; Toney, M. F.; McGehee, M. D. Factors Governing Intercalation of Fullerenes and Other Small Molecules between the Side Chains of Semiconducting Polymers Used in Solar Cells. *Advanced Energy Materials* **2012**, *2* (10), 1208–1217. <https://doi.org/10.1002/aenm.201200392>.
- (164) Matrone, G. M.; Gutiérrez-Meza, E.; Balzer, A. H.; Khirbat, A.; Levitsky, A.; Sieval, A. B.; Frey, G. L.; Richter, L. J.; Silva, C.; Stingelin, N. The Hole in the Bucky: Structure-Property Mapping of Closed- Vs. Open-Cage Fullerene Solar-Cell Blends via Temperature/Composition Phase Diagrams. *Journal of Materials Chemistry C* **2021**, *9* (45), 16304–16312. <https://doi.org/10.1039/d1tc03082e>.
- (165) Zhang, W.; Smith, J.; Watkins, S. E.; Gysel, R.; McGehee, M.; Salleo, A.; Kirkpatrick, J.; Ashraf, S.; Anthopoulos, T.; Heeney, M.; McCulloch, I. Indacenodithiophene Semiconducting Polymers for High-Performance, Air-Stable Transistors. *J Am Chem Soc* **2010**, *132* (33), 11437–11439. <https://doi.org/10.1021/ja1049324>.
- (166) Bronstein, H.; Chen, Z.; Ashraf, R. S.; Zhang, W.; Du, J.; Durrant, J. R.; Shakya Tuladhar, P.; Song, K.; Watkins, S. E.; Geerts, Y.; Wienk, M. M.; Janssen, R. A. J.; Anthopoulos, T.; Sirringhaus, H.; Heeney, M.; McCulloch, I. Thieno[3,2- b]Thiophene-Diketopyrrolopyrrole-Containing Polymers for High-Performance Organic Field-Effect Transistors and Organic Photovoltaic Devices. *J Am Chem Soc* **2011**, *133* (10), 3272–3275. <https://doi.org/10.1021/ja110619k>.
- (167) Mei, J.; Kim, D. H.; Ayzner, A. L.; Toney, M. F.; Bao, Z. Siloxane-Terminated Solubilizing Side Chains: Bringing Conjugated Polymer Backbones Closer and Boosting Hole Mobilities in Thin-Film Transistors. *J Am Chem Soc* **2011**, *133* (50), 20130–20133. <https://doi.org/10.1021/ja209328m>.
- (168) Tsao, H. N.; Cho, D. M.; Park, I.; Hansen, M. R.; Mavrinskiy, A.; Yoon, D. Y.; Graf, R.; Pisula, W.; Spiess, H. W.; Müllen, K. Ultrahigh Mobility in Polymer Field-Effect Transistors by Design. *J Am Chem Soc* **2011**, *133* (8), 2605–2612. <https://doi.org/10.1021/ja108861q>.
- (169) Zhang, X.; Bronstein, H.; Kronemeijer, A. J.; Smith, J.; Kim, Y.; Kline, R. J.; Richter, L. J.; Anthopoulos, T. D.; Sirringhaus, H.; Song, K.; Heeney, M.; Zhang, W.; McCulloch, I.; Delongchamp, D. M. Molecular Origin of High Field-Effect Mobility in an Indacenodithiophene- Benzothiadiazole Copolymer. *Nature Communications* **2013**, *4*. <https://doi.org/10.1038/ncomms3238>.
- (170) Coropceanu, V.; Cornil, J.; da Silva Filho, D. A.; Olivier, Y.; Silbey, R.; Brédas, J. L. Charge Transport in Organic Semiconductors. *Chemical Reviews* **2007**, *107* (4), 926–952. <https://doi.org/10.1021/CR050140X/ASSET/IMAGES/MEDIUM/CR050140XE00056.GIF>.

- (171) Sirringhaus, H. Device Physics of Solution-Processed Organic Field-Effect Transistors. *Advanced Materials* **2005**, *17* (20), 2411–2425. <https://doi.org/10.1002/adma.200501152>.
- (172) Root, S. E.; Savagatrup, S.; Printz, A. D.; Rodriguez, D.; Lipomi, D. J. Mechanical Properties of Organic Semiconductors for Stretchable, Highly Flexible, and Mechanically Robust Electronics. *Chemical Reviews* **2017**, *117* (9), 6467–6499. <https://doi.org/10.1021/acs.chemrev.7b00003>.
- (173) Balar, N.; O'Connor, B. T. Correlating Crack Onset Strain and Cohesive Fracture Energy in Polymer Semiconductor Films. *Macromolecules* **2017**, *50* (21), 8611–8618. <https://doi.org/10.1021/acs.macromol.7b01282>.
- (174) Zheng, Y.; Wang, G. J. N.; Kang, J.; Nikolka, M.; Wu, H. C.; Tran, H.; Zhang, S.; Yan, H.; Chen, H.; Yuen, P. Y.; Mun, J.; Dauskardt, R. H.; McCulloch, I.; Tok, J. B. H.; Gu, X.; Bao, Z. An Intrinsically Stretchable High-Performance Polymer Semiconductor with Low Crystallinity. *Advanced Functional Materials* **2019**, *29* (46), 1–12. <https://doi.org/10.1002/adfm.201905340>.
- (175) Li, Y.; Tatum, W. K.; Onorato, J. W.; Zhang, Y.; Luscombe, C. K. Low Elastic Modulus and High Charge Mobility of Low-Crystallinity Indacenodithiophene-Based Semiconducting Polymers for Potential Applications in Stretchable Electronics. *Macromolecules* **2018**, *51* (16), 6352–6358. <https://doi.org/10.1021/acs.macromol.8b00898>.
- (176) Sommerville, P. J. W.; Li, Y.; Dong, B. X.; Zhang, Y.; Onorato, J. W.; Tatum, W. K.; Balzer, A. H.; Stingelin, N.; Patel, S. N.; Nealey, P. F.; Luscombe, C. K. Elucidating the Influence of Side-Chain Circular Distribution on the Crack Onset Strain and Hole Mobility of Near-Amorphous Indacenodithiophene Copolymers. *Macromolecules* **2020**, *53* (17), 7511–7518. <https://doi.org/10.1021/acs.macromol.0c00512>.
- (177) Balar, N.; Siddika, S.; Kashani, S.; Peng, Z.; Rech, J. J.; Ye, L.; You, W.; Ade, H.; O'Connor, B. T. Role of Secondary Thermal Relaxations in Conjugated Polymer Film Toughness. *Chemistry of Materials* **2020**, *32* (15), 6540–6549. <https://doi.org/10.1021/acs.chemmater.0c01910>.
- (178) Sharma, A.; Pan, X.; Bjuggren, J. M.; Gedefaw, D.; Xu, X.; Kroon, R.; Wang, E.; Campbell, J. A.; Lewis, D. A.; Andersson, M. R. Probing the Relationship between Molecular Structures, Thermal Transitions, and Morphology in Polymer Semiconductors Using a Woven Glass-Mesh-Based DMTA Technique. *Chemistry of Materials* **2019**, *31* (17), 6740–6749. https://doi.org/10.1021/ACS.CHEMMATER.9B01213/ASSET/IMAGES/LARGE/CM-2019-012133_0007.JPEG.
- (179) Cao, Z.; Galuska, L.; Qian, Z.; Zhang, S.; Huang, L.; Prine, N.; Li, T.; He, Y.; Hong, K.; Gu, X. The Effect of Side-Chain Branch Position on the Thermal Properties of Poly(3-Alkylthiophenes). *Polymer Chemistry* **2020**, *11* (2), 517–526. <https://doi.org/10.1039/c9py01026b>.

- (180) Koch, F. P. V.; Rivnay, J.; Foster, S.; Müller, C.; Downing, J. M.; Buchaca-Domingo, E.; Westacott, P.; Yu, L.; Yuan, M.; Baklar, M.; Fei, Z.; Luscombe, C.; McLachlan, M. A.; Heeney, M.; Rumbles, G.; Silva, C.; Salleo, A.; Nelson, J.; Smith, P.; Stingelin, N. The Impact of Molecular Weight on Microstructure and Charge Transport in Semicrystalline Polymer Semiconductors-Poly(3-Hexylthiophene), a Model Study. *Progress in Polymer Science* **2013**, 38 (12), 1978–1989. <https://doi.org/10.1016/j.progpolymsci.2013.07.009>.
- (181) Ungar, G.; Stejny, J.; Keller, A.; Bidd, I.; Whiting, M. C. The Crystallization of Ultralong Normal Paraffins: The Onset of Chain Folding. *Science* (1979) **1985**, 229 (4711), 386–389. <https://doi.org/10.1126/science.229.4711.386>.
- (182) Flory, P. J. On the Morphology of the Crystalline State in Polymers. *J Am Chem Soc* **1962**, 84 (15), 2857–2867. <https://doi.org/10.1021/ja00874a004>.
- (183) Paulsen, B. D.; Tybrandt, K.; Stavrinidou, E.; Rivnay, J. Organic Mixed Ionic–Electronic Conductors. *Nature Materials* **2020**, 19 (1), 13–26. <https://doi.org/10.1038/s41563-019-0435-z>.
- (184) Khodagholy, D.; Doublet, T.; Quilichini, P.; Gurfinkel, M.; Leleux, P.; Ghestem, A.; Ismailova, E.; Hervé, T.; Sanaur, S.; Bernard, C.; Malliaras, G. G. In Vivo Recordings of Brain Activity Using Organic Transistors. *Nature Communications* **2013**, 4. <https://doi.org/10.1038/ncomms2573>.
- (185) Rivnay, J.; Leleux, P.; Ferro, M.; Sessolo, M.; Williamson, A.; Koutsouras, D. A.; Khodagholy, D.; Ramuz, M.; Strakosas, X.; Owens, R. M.; Benar, C.; Badier, J. M.; Bernard, C.; Malliaras, G. G. High-Performance Transistors for Bioelectronics through Tuning of Channel Thickness. *Science Advances* **2015**, 1 (4), 1–6. <https://doi.org/10.1126/sciadv.1400251>.
- (186) Neo, W. T.; Ye, Q.; Chua, S. J.; Xu, J. Conjugated Polymer-Based Electrochromics: Materials, Device Fabrication and Application Prospects. *Journal of Materials Chemistry C* **2016**, 4 (31), 7364–7376. <https://doi.org/10.1039/c6tc01150k>.
- (187) Collier, G. S.; Pelse, I.; Reynolds, J. R. Aqueous Electrolyte Compatible Electrochromic Polymers Processed from an Environmentally Sustainable Solvent. *ACS Macro Letters* **2018**, 7 (10), 1208–1214. <https://doi.org/10.1021/acsmacrolett.8b00551>.
- (188) Meng, Q.; Cai, K.; Chen, Y.; Chen, L. Research Progress on Conducting Polymer Based Supercapacitor Electrode Materials. *Nano Energy* **2017**, 36 (April), 268–285. <https://doi.org/10.1016/j.nanoen.2017.04.040>.
- (189) Facchetti, A. π -Conjugated Polymers for Organic Electronics and Photovoltaic Cell Applications. *Chemistry of Materials* **2011**, 23 (3), 733–758. <https://doi.org/10.1021/cm102419z>.
- (190) Onorato, J. W.; Wang, Z.; Sun, Y.; Nowak, C.; Flagg, L. Q.; Li, R.; Dong, B. X.; Richter, L. J.; Escobedo, F. A.; Nealey, P. F.; Patel, S. N.; Luscombe, C. K. Side Chain Engineering Control of Mixed Conduction in Oligoethylene Glycol-Substituted Polythiophenes. *Journal of Materials Chemistry A* **2021**, 9 (37), 21410–21423. <https://doi.org/10.1039/d1ta05379e>.

- (191) Cao, Y.; Yu, G.; Heeger, A. J.; Yang, C. Y. Efficient, Fast Response Light-Emitting Electrochemical Cells: Electroluminescent and Solid Electrolyte Polymers with Interpenetrating Network Morphology. *Applied Physics Letters* **1996**, *68* (23), 3218–3220. <https://doi.org/10.1063/1.116442>.
- (192) van Reenen, S.; Akatsuka, T.; Tordera, D.; Kemerink, M.; Bolink, H. J. Universal Transients in Polymer and Ionic Transition Metal Complex Light-Emitting Electrochemical Cells. *J Am Chem Soc* **2013**, *135* (2), 886–891. <https://doi.org/10.1021/ja3107803>.
- (193) Inal, S.; Malliaras, G. G.; Rivnay, J. Benchmarking Organic Mixed Conductors for Transistors. *Nature Communications* **2017**, *8* (1), 1–6. <https://doi.org/10.1038/s41467-017-01812-w>.
- (194) Stavrinidou, E.; Leleux, P.; Rajaona, H.; Khodagholy, D.; Rivnay, J.; Lindau, M.; Sanaur, S.; Malliaras, G. G. Direct Measurement of Ion Mobility in a Conducting Polymer. *Advanced Materials* **2013**, *25* (32), 4488–4493. <https://doi.org/10.1002/adma.201301240>.
- (195) Hallinan, D. T.; Balsara, N. P. Polymer Electrolytes. *Annual Review of Materials Research* **2013**, *43*, 503–525. <https://doi.org/10.1146/annurev-matsci-071312-121705>.
- (196) Patel, S. N.; Javier, A. E.; Stone, G. M.; Mullin, S. A.; Balsara, N. P. Simultaneous Conduction of Electronic Charge and Lithium Ions in Block Copolymers. *ACS Nano* **2012**, *6* (2), 1589–1600. <https://doi.org/10.1021/nn2045664>.
- (197) Merkle, R.; Gutbrod, P.; Reinold, P.; Katzmaier, M.; Tkachov, R.; Maier, J.; Ludwigs, S. Mixed Conductivity of Polythiophene-Based Ionic Polymers under Controlled Conditions. *Polymer (Guildf)* **2017**, *132*, 216–226. <https://doi.org/10.1016/j.polymer.2017.10.064>.
- (198) Groenendaal, L.; Zotti, G.; Aubert, P. H.; Waybright, S. M.; Reynolds, J. R. Electrochemistry of Poly(3,4-Alkylenedioxythiophene) Derivatives. *Advanced Materials* **2003**, *15* (11), 855–879. <https://doi.org/10.1002/adma.200300376>.
- (199) Savagian, L. R.; Österholm, A. M.; Ponder, J. F.; Barth, K. J.; Rivnay, J.; Reynolds, J. R. Balancing Charge Storage and Mobility in an Oligo(Ether) Functionalized Dioxothiophene Copolymer for Organic- and Aqueous- Based Electrochemical Devices and Transistors. *Advanced Materials* **2018**, *30* (50), 1–6. <https://doi.org/10.1002/adma.201804647>.
- (200) Bargigia, I.; Savagian, L. R.; Österholm, A. M.; Reynolds, J. R.; Silva, C. Charge-Transfer Intermediates in the Electrochemical Doping Mechanism of Conjugated Polymers. *J Am Chem Soc* **2021**, *143* (1), 294–308. <https://doi.org/10.1021/jacs.0c10692>.
- (201) Das, P.; Zayat, B.; Wei, Q.; Salamat, C. Z.; Magdău, I. B.; Elizalde-Segovia, R.; Rawlings, D.; Lee, D.; Pace, G.; Irshad, A.; Ye, L.; Schmitt, A.; Segalman, R. A.; Miller, T. F.; Tolbert, S. H.; Dunn, B. S.; Narayan, S. R.; Thompson, B. C. Dihexyl-Substituted Poly(3,4-Propylenedioxythiophene) as a Dual Ionic and Electronic Conductive Cathode Binder for Lithium-Ion Batteries. *Chemistry of Materials* **2020**, *32* (21), 9176–9189. <https://doi.org/10.1021/acs.chemmater.0c02601>.

- (202) Pittelli, S. L.; de Keersmaecker, M.; Ponder, J. F.; Österholm, A. M.; Ochieng, M. A.; Reynolds, J. R. Structural Effects on the Charge Transport Properties of Chemically and Electrochemically Doped Dioxythiophene Polymers. *Journal of Materials Chemistry C* **2020**, 8 (2), 683–693. <https://doi.org/10.1039/c9tc05697a>.
- (203) Ponder, J. F.; Gregory, S. A.; Atassi, A.; Menon, A. K.; Lang, A. W.; Savagian, L. R.; Reynolds, J. R.; Yee, S. K. Significant Enhancement of the Electrical Conductivity of Conjugated Polymers by Post-Processing Side Chain Removal. *J Am Chem Soc* **2022**, 144 (3), 1351–1360. <https://doi.org/10.1021/jacs.1c11558>.
- (204) Flagg, L. Q.; Bischak, C. G.; Onorato, J. W.; Rashid, R. B.; Luscombe, C. K.; Ginger, D. S. Polymer Crystallinity Controls Water Uptake in Glycol Side-Chain Polymer Organic Electrochemical Transistors. *J Am Chem Soc* **2019**, 141 (10), 4345–4354. <https://doi.org/10.1021/jacs.8b12640>.
- (205) White, R. P.; Lipson, J. E. G. Polymer Free Volume and Its Connection to the Glass Transition. *Macromolecules* **2016**, 49 (11), 3987–4007. <https://doi.org/10.1021/acs.macromol.6b00215>.
- (206) Zhan, P.; Zhang, W.; Jacobs, I. E.; Nisson, D. M.; Xie, R.; Weissen, A. R.; Colby, R. H.; Moulé, A. J.; Milner, S. T.; Maranas, J. K.; Gomez, E. D. Side Chain Length Affects Backbone Dynamics in Poly(3-Alkylthiophene)s. *Journal of Polymer Science, Part B: Polymer Physics* **2018**, 56 (17), 1193–1202. <https://doi.org/10.1002/polb.24637>.
- (207) Moynihan, C. T.; Easteal, A. J.; Wilder, J.; Tucker, J. Dependence of the Glass Transition Temperature on Heating and Cooling Rate. *Journal of Physical Chemistry* **1974**, 78 (26), 2673–2677. https://doi.org/10.1021/J100619A008/ASSET/J100619A008.FP.PNG_V03.
- (208) Clark, J.; Silva, C.; Friend, R. H.; Spano, F. C. Role of Intermolecular Coupling in the Photophysics of Disordered Organic Semiconductors: Aggregate Emission in Regioregular Polythiophene. *Physical Review Letters* **2007**, 98 (20), 1–4. <https://doi.org/10.1103/PhysRevLett.98.206406>.
- (209) Spano, F. C.; Silva, C. H- and J-Aggregate Behavior in Polymeric Semiconductors. *Annual Review of Physical Chemistry* **2014**, 65, 477–500. <https://doi.org/10.1146/annurev-physchem-040513-103639>.
- (210) Hassab, S.; Shen, D. E.; Österholm, A. M.; da Rocha, M.; Song, G.; Alesanco, Y.; Viñuales, A.; Rougier, A.; Reynolds, J. R.; Padilla, J. A New Standard Method to Calculate Electrochromic Switching Time. *Solar Energy Materials and Solar Cells* **2018**, 185, 54–60. <https://doi.org/10.1016/J.SOLMAT.2018.04.031>.
- (211) Lim, H.; Hoag, S. W. Plasticizer Effects on Physical-Mechanical Properties of Solvent Cast Soluplus® Films. *AAPS PharmSciTech* **2013**, 14 (3), 903–910. <https://doi.org/10.1208/S12249-013-9971-Z/FIGURES/12>.
- (212) Bocharova, V.; Sokolov, A. P. Perspectives for Polymer Electrolytes: A View from Fundamentals of Ionic Conductivity. *Macromolecules* **2020**, 53 (11), 4141–4157.

- https://doi.org/10.1021/ACS.MACROMOL.9B02742/ASSET/IMAGES/LARGE/MA9B02742_0002.JPEG.
- (213) Wang, X.; Chen, K.; de Vasconcelos, L. S.; He, J.; Shin, Y. C.; Mei, J.; Zhao, K. Mechanical Breathing in Organic Electrochromics. *Nature Communications* **2020**, *11* (1), 1–10. <https://doi.org/10.1038/s41467-019-14047-8>.
 - (214) Reimschuessel, H. K. On the Glass Transition Temperature of Comblike Polymers: Effects of Side Chain Length and Backbone Chain Structure. *J Polym Sci Polym Chem Ed* **1979**, *17* (8), 2447–2457. <https://doi.org/10.1002/pol.1979.170170817>.
 - (215) Cowie, J. M. G.; Ho, C. Y. GLASS TRANSITIONS AND RELAXATIONS IN COMB-BRANCH POLY(DI-*p*-ALKOXYPHENYL ITACONATE)S. *British Polymer Journal* **1987**, *19* (3–4), 347–352. <https://doi.org/10.1002/pi.4980190318>.
 - (216) Overberger, C. G.; Frazier, C.; Mandelman, J.; Smith, H. F. The Preparation and Polymerization of *p*-Alkylstyrenes. Effect of Structure on the Transition Temperatures of the Polymers. *J Am Chem Soc* **1953**, *75* (14), 3326–3330. <https://doi.org/10.1021/ja01110a010>.
 - (217) Cowie, J. M. G.; Haq, Z.; McEwen, I. J.; Veličković, J. Poly(Alkyl Itaconates): 8. Observations of Dual Glass Transitions and Crystallinity in the Dialkyl Ester Series Diheptyl to Di-Eicosyl. *Polymer (Guildf)* **1981**, *22* (3), 327–332. [https://doi.org/10.1016/0032-3861\(81\)90043-4](https://doi.org/10.1016/0032-3861(81)90043-4).
 - (218) Genix, A. C.; Lauprêtre, F. Investigation of Local Chain Dynamics in Poly(Di-*n*-Alkylitaconate)s. *Journal of Non-Crystalline Solids* **2006**, *352* (42-49 SPEC. ISS.), 5035–5041. <https://doi.org/10.1016/j.jnoncrysol.2006.01.134>.
 - (219) Jordan, E. F. Side-Chain Crystallinity. III. Influence of Side-Chain Crystallinity on the Glass Transition Temperatures of Selected Copolymers Incorporating *n*-Octadecyl Acrylate or Vinyl Stearate. *Journal of Polymer Science Part A-1: Polymer Chemistry* **1971**, *9* (11), 3367–3378. <https://doi.org/10.1002/pol.1971.150091122>.
 - (220) Rogers, S.; Mandelkern, L. Glass Transitions of the Poly-(*n*-Alkyl Methacrylates). *The Journal of Physical Chemistry* **1957**, *61* (7), 985–991. <https://doi.org/10.1021/j150553a033>.
 - (221) Suzuki, H.; Grebowicz, J.; Wunderlich, B. Glass Transition of Poly(Oxymethylene). *British Polymer Journal* **1985**, *17* (1), 1–3. <https://doi.org/10.1002/PI.4980170101>.
 - (222) Monnier, X.; Cavallo, D.; Righetti, M. C.; di Lorenzo, M. L.; Marina, S.; Martin, J.; Cangialosi, D. Physical Aging and Glass Transition of the Rigid Amorphous Fraction in Poly(*l*-Lactic Acid). *Macromolecules* **2020**, *53* (20), 8741–8750. <https://doi.org/10.1021/acs.macromol.0c01182>.
 - (223) Martín, J.; Stingelin, N.; Cangialosi, D. Direct Calorimetric Observation of the Rigid Amorphous Fraction in a Semiconducting Polymer. *Journal of Physical Chemistry Letters* **2018**, *9* (5), 990–995. <https://doi.org/10.1021/acs.jpcllett.7b03110>.

- (224) Simha Martynková, G.; Slíva, A.; Kratošová, G.; Čech Barabaszová, K.; Študentová, S.; Klusák, J.; Brožová, S.; Dokoupil, T.; Holešová, S. Polyamide 12 Materials Study of Morpho-Structural Changes during Laser Sintering of 3D Printing. *Polymers (Basel)* **2021**, *13* (5). <https://doi.org/10.3390/polym13050810>.
- (225) Avrami, M. Kinetics of Phase Change. I: General Theory. *The Journal of Chemical Physics* **1939**, *7* (12), 1103–1112. <https://doi.org/10.1063/1.1750380>.
- (226) Avrami, M. Kinetics of Phase Change. II Transformation-Time Relations for Random Distribution of Nuclei. *The Journal of Chemical Physics* **1940**, *8* (2), 212–224. <https://doi.org/10.1063/1.1750631>.
- (227) Avrami, M. Granulation, Phase Change, and Microstructure Kinetics of Phase Change. III. *The Journal of Chemical Physics* **1941**, *9* (2), 177–184. <https://doi.org/10.1063/1.1750872>.
- (228) Jariyavidyanont, K.; Zhuravlev, E.; Schick, C.; Androsch, R. Kinetics of Homogeneous Crystal Nucleation of Polyamide 11 near the Glass Transition Temperature. *Polymer Crystallization* **2021**, *4* (1), e10149. <https://doi.org/10.1002/PCR2.10149>.
- (229) Toda, A.; Androsch, R.; Schick, C. Insights into Polymer Crystallization and Melting from Fast Scanning Chip Calorimetry. *Polymer*. Elsevier Ltd May 17, 2016, pp 239–263. <https://doi.org/10.1016/j.polymer.2016.03.038>.
- (230) Zhuravlev, E.; Schmelzer, J. W. P.; Wunderlich, B.; Schick, C. Kinetics of Nucleation and Crystallization in Poly(ϵ -Caprolactone) (PCL). *Polymer (Guildf)* **2011**, *52* (9), 1983–1997. <https://doi.org/10.1016/j.polymer.2011.03.013>.
- (231) Khirbat, A. Influence of Local Polar Environment on the Optoelectronic Landscape of Polymeric Semiconductors, Georgia Institute of Technology, 2021.
- (232) Chen, Y.; Shen, Q. D.; Hu, W. Primary and Secondary Crystallization of Fast-Cooled Poly(Vinylidene Fluoride) Studied by Flash DSC, Wide-Angle X-Ray Diffraction and Fourier Transform Infrared Spectroscopy. *Polymer International* **2016**, *65* (4), 387–392. <https://doi.org/10.1002/pi.5066>.
- (233) Chen, Y.; Chen, X.; Zhou, D.; Shen, Q. D.; Hu, W. Low-Temperature Crystallization of P(VDF-TrFE-CFE) Studied by Flash DSC. *Polymer (Guildf)* **2016**, *84*, 319–327. <https://doi.org/10.1016/j.polymer.2016.01.003>.
- (234) Wang, B.; Utzeri, R.; Castellano, M.; Stagnaro, P.; Müller, A. J.; Cavallo, D. Heterogeneous Nucleation and Self-Nucleation of Isotactic Polypropylene Microdroplets in Immiscible Blends: From Nucleation to Growth-Dominated Crystallization. *Macromolecules* **2020**, *53* (14), 5980–5991. <https://doi.org/10.1021/acs.macromol.0c01167>.
- (235) Wenzel, F. A.; Welz, H.; Zwan, K. P. van der; Stäter, S.; Kreger, K.; Hildner, R.; Senker, J.; Schmidt, H.-W. Highly Efficient Supramolecular Nucleating Agents for Poly(3-Hexylthiophene). *Macromolecules* **2022**, *55* (7), 2861–2871. <https://doi.org/10.1021/ACS.MACROMOL.1C02283>.

- (236) Lindqvist, C.; Bergqvist, J.; Feng, C. C.; Gustafsson, S.; Bäcke, O.; Treat, N. D.; Bounioux, C.; Henriksson, P.; Kroon, R.; Wang, E.; Sanz-Velasco, A.; Kristiansen, P. M.; Stingelin, N.; Olsson, E.; Inganäs, O.; Andersson, M. R.; Müller, C. Fullerene Nucleating Agents: A Route towards Thermally Stable Photovoltaic Blends. *Advanced Energy Materials* **2014**, *4* (9), 1–10. <https://doi.org/10.1002/aenm.201301437>.
- (237) Wunderlich, B. Structural Data on Crystalline Polymers by Thermal Analysis. *Journal of Polymer Science: Polymer Symposia* **1973**, *43* (1), 29–42. <https://doi.org/10.1002/POLC.5070430106>.
- (238) Schick, C.; Toda, A.; Androsch, R. The Narrow Thickness Distribution of Lamellae of Poly(Butylene Succinate) Formed at Low Melt Supercooling. *Macromolecules* **2021**, *54* (7), 3366–3376. <https://doi.org/10.1021/acs.macromol.1c00388>.
- (239) Toda, A.; Androsch, R.; Schick, C. Melting Kinetics of Superheated Polymer Crystals Examined by Isothermal and Nonisothermal Fast Scanning Calorimetry. *Macromolecules* **2021**, *54* (18), 8770–8779. <https://doi.org/10.1021/acs.macromol.1c01628>.